5-2023

Exploring Ferroelectric Phenomena in BaTiO3, LiNbO3, and LiZnSb: From Extended Oxygen Vacancies to Tri-Stable Polarization and Giant Hyperferroelectricity

Shaohui Qiu
University of Arkansas, Fayetteville

Exploring Ferroelectric Phenomena in $BaTiO_3$, $LiNbO_3$, and LiZnSb: From Extended Oxygen Vacancies to Tri-Stable Polarization and Giant Hyperferroelectricity

A dissertation submitted in partial fulfillment
of the requirements for the degree of
Doctor of Philosophy in Physics

by

Shaohui Qiu
Wenzhou University, Oujiang Independent College
Bachelor of Law, 2012
University of Central Arkansas
Bachelor of Science in Physics, 2015

May 2023
University of Arkansas

This dissertation is approved for recommendation to the Graduate Council.

_____
Huaxiang Fu, Ph.D.
Dissertation Director

_____
Laurent Bellaiche, Ph.D.
Committee Member

_____
Hameed Naseem, Ph.D.
Committee Member

Abstract

This dissertation presents three projects that investigate the complex phenomena of ferroelectricity under different conditions in $BaTiO_3$, $LiNbO_3$, and LiZnSb using first-principles density functional calculations. Extended defects in ferroelectric solids play a crucial role in reducing the lifetime and performance of ferroelectric devices by causing fatigue, domain pinning, and aging. Thus, understanding their impact is of critical importance for the development of reliable and high-performance ferroelectric devices. In addition, hyperferroelectricity is an intriguing phenomenon that has attracted much attention in recent years. Despite the existence of depolarization field, spontaneous polarization persists under an open-circuit boundary condition (OCBC), making hyperferroelectric materials promising candidates for various electronic applications.

In the first project, we investigate the energetic, structural, and electric properties caused by extended planar oxygen vacancies in ferroelectric $BaTiO_3$. Oxygen vacancies of different charge states, namely V_O^{2+}, V_O^{1+}, and V_O^0, are studied. We find that, while planar V_O^q vacancies of all three charge states may take place under the oxygen-*poor* condition, planar V_O^{2+} vacancies can still occur even under the oxygen-*rich* condition. Furthermore, our calculations show that $BaTiO_3$ with planar V_O^0 or V_O^{1+} vacancies is metallic, while $BaTiO_3$ with planar V_O^{2+} vacancies is an insulator. This finding reveals an important conclusion that, for $BaTiO_3$ with planar V_O^{2+} vacancies, no mobile charges are available to screen the polarization, electric polarization is thus well defined and can be rigorously computed. Moreover, we discover that *extended* planar V_O^{2+} vacancies produce a devastating effect on ferroelectricity by drastically reducing the electric polarization, which is markedly different from *isolated* V_O^{2+} vacancies (which are benign to ferroelectricity). The polarization dead layer caused by planar oxygen vacancies is shown to be around 72Å.

In the second project, we investigate the hyperferroelectric properties of $LiNbO_3$. We find that (i) the longitudinal-optic $A_{2u}(LO_1)$ phonon is soft with imaginary frequency $96i$ cm^{-1} when centrosymmetric $LiNbO_3$ is under OCBC. (ii) The $A_{2u}(LO_1)$ phonon can yield, under OCBC, a free-energy minimum with well depth of -9 meV at a nonzero polarization of 0.023 C/m^2, thereby capable of producing hyperferroelectricity. (iii) The origin that $A_{2u}(LO_1)$ can induce HyFE stems from the extraordinarily small mode effective charge of this phonon. (iv) Despite that $A_{2u}(LO_1)$ can induce HyFE, we find the ground state of $LiNbO_3$ under OCBC is not polar, revealing that the existence of a soft LO phonon does not guarantee HyFE. (v) We further show that $LiNbO_3$ under OCBC may exhibit unusual tri-stable polarization states, with two potential wells of depth -23 meV and -1.9 meV.

However, small polarization and shallow well depth are found so far in most hyperferroelectric materials, including $LiNbO_3$, which severely limits their applications. In the third project, we report the discovery of a giant hyperferroelectricity in LiZbSb. The HyFE polarization is shown to be remarkably large with P=0.282 C/m^2 under OCBC, which is one order of magnitude greater than the HyFE polarization in $LiNbO_3$. Furthermore, HyFE in LiZnSb is found to be exceptionally stable with a well depth of electric free energy ΔF=-332 meV, which makes LiZnSb a possible hyperferroelectric solid at room temperature. The origin of the giant hyperferroelectricity in LiZnSb is attributed to the large mode effective charge of the soft longitudinal-optic phonon and the large high-frequency dielectric constant. The HyFE strain dependence in LiZnSb is also examined.

Acknowledgements

I am extremely grateful to my advisor, Prof. Huaxiang Fu, for his unwavering support and guidance throughout my doctoral journey. Prof. Fu's expertise, patience, and encouragement have been invaluable to me, and I have learned so much from him in the process. I could not have completed this dissertation without his mentorship, and I am truly grateful for his contributions to my academic and personal growth.

I would also like to express my gratitude to my committee members, Prof. Laurent Bellaiche and Prof. Hameed Naseem, for their valuable insights and feedback during my doctoral studies. Their expertise and critical perspectives have been instrumental in shaping my research and helping me to develop as a scholar.

In addition, I would like to thank the faculty and staff of the Department of Physics at University of Arkansas, as well as my colleagues for their support and encouragement. I am grateful for the opportunities I have had to collaborate, learn, and grow with them.

Finally, I would like to thank my family and friends for their support and encouragement throughout my doctoral studies. Their love, patience, and understanding have been essential to my success and well-being.

Thank you all for your contributions to this accomplishment.

Dedication

This dissertation is dedicated to my wife Songyan, who has been a constant source of love and support throughout my journey, and to my amazing daughters Shiloh and Sarah. Your encouragement and belief in me have been instrumental in reaching this point, and I am forever grateful for your presence in my life. Thank you for being my inspiration and motivation, and for sharing this journey with me.

Table of Contents

List of Figures

Chapter 1:

Chapter 2:

Chapter 3:

List of Tables

Chapter 2:

Chapter 3:

List of Published Papers

Manuscript in preparation:

[1] S. Qiu and H. Fu, Extended planar defects of oxygen vacancies in ferroelectric BaTiO3: Vacancy formation energy, condition of existence, insulating/conducting nature, and impact on ferroelectricity, (Chapter 1).

Published:

[2] S. Qiu, L. Ma, S. Liu, and H. Fu, Possible existence of tristable polarization states in $LiNbO_3$ under an open-circuit boundary condition, Phys. Rev. B **104**, 064112 (2021), **(**Chapter 2).

[3] S. Qiu, S. Rhodes, and H. Fu, Giant hyperferroelectricity in LiZnSb and its origin, Phys. Rev. B 107, 094108 (2023), (Chapter 3).

Introduction

Ferroelectricity (FE) is a phenomenon that occurs in certain materials where a spontaneous polarization arises due to the distortion of the crystal structure. This spontaneous polarization can be reversed by the application of an external electric field, causing a hysteresis loop in the polarization-electric field curve. In addition, the presence of a spontaneous electric polarization gives rise to many unique and interesting properties, such as piezoelectricity, pyroelectricity, and non-linear optical effects. These interesting features make ferroelectric materials highly attractive for technological applications such as capacitors, sensors, actuators, and memory devices.

Extended vacancies in ferroelectrics have significant implications both from a fundamental and technological perspective. Fundamentally, extended vacancies can cause substantial changes in atom-atom interactions over an extensive spatial region, leading to significant alterations in ferroelectricity, polarization, and other properties. Moreover, extended vacancies can influence the ferroelectric instability and give rise to novel phenomena not observed in perfect bulks or bulks with isolated defects. Despite their importance, extended defects are less understood than isolated defects, which have been the focus of most previous studies of defect physics in FEs[1-8].

From a technological standpoint, extended vacancies play a crucial role in understanding persistent issues such as polarization fatigue and aging. The presence of extended defects can impair the performance of these devices, as defects have been linked to polarization fatigue and aging in polarization switching, and can also pin domain walls leading to the imprinting of electric polarization[9-14]. Meanwhile they can also be beneficial by producing properties that do not exist in perfect FEs [15-18]. Understanding how to eliminate or intentionally generate vacancies in FEs is crucial for maximizing their benefits and minimizing their detrimental effects.

Hyperferroelectricity (HyFE) is a fascinating phenomenon that has attracted significant attention in recent years. Proper ferroelectrics are materials that exhibit ferroelectricity due to a soft phonon at the zone center, while improper ferroelectrics exhibit ferroelectricity due to rotational soft modes at the zone boundary. In proper ferroelectrics under open-circuit boundary conditions (OCBC), the strong depolarization field tends to eliminate the polarization [19, 20]. However, HyFE materials can overcome this limitation and maintain polar instability even under OCBC, making them of significant interest for both fundamental research and technological applications [21-23].

It has been proposed that the possible HyFE origin can be attributed to the small Born effective charge of ions and small longitudinal-optic/transverse-optic splitting [21]; deep internal-energy well and small spontaneous polarization [22]; the significance of short-range interaction [23, 24], or the existence of metascreening [25].

Despite the progress made in understanding the mechanism of HyFE, many fundamental challenges remain. For example, one critical challenge is to develop reliable methods to accurately determine whether a solid is HyFE. One common approach is to use the existence of soft longitudinal-optic (LO) phonons with imaginary frequencies as the hallmark of HyFE [3-5]. However, it is not yet clear whether this criterion is fully justified and whether a solid with soft LO phonons will always exhibit HyFE. Another fundamental challenge is to understand why the strong depolarization field does not eliminate the polarization in HyFE. This requires identifying the physical origin responsible for the persistence of the polarization in HyFE. Additionally, it is crucial to identify pivotal physical quantities that guide the search for new HyFEs. Currently, the search for new HyFEs often relies on a trial-and-error approach, which can be time-consuming and less efficient.

In addition to these challenges, HyFE faces two other fundamental challenges. (i) The spontaneous polarization under OCBC found in many HyFE materials is often very small and not practically useful. For example, the HyFE polarization in LiBeSb is merely 0.02 C/m^2 under OCBC, which is more than twenty times smaller than the value of 0.59 C/m^2 of the same solid under a short-circuit boundary condition (SCBC) [21]. This presents an outstanding obstacle to the technological use of hyperferroelectricity. (ii) The well depth of HyFE is often very small, which means that the HyFE phase is stable only at very low temperatures. Thermal fluctuations can easily eliminate the hyperferroelectricity, making it challenging to develop HyFE materials that are stable at room temperature. To overcome these challenges, it is essential to develop new approaches and techniques to explore and understand HyFE.

In this dissertation, we present three projects that investigate the complex phenomena of ferroelectricity and hyperferroelectricity in $BaTiO_3$, $LiNbO_3$, and LiZnSb using first-principles density functional calculations. In the first project (Chapter 1), we investigate the extended planar oxygen vacancies in ferroelectric $BaTiO_3$, a commonly used material in FE devices. We find that planar oxygen vacancies are not as difficult to form as previously thought and can drastically reduce ferroelectricity in $BaTiO_3$, potentially causing polarization fatigue and imprinting. We also also provide insights into the optimal conditions to eliminate or generate planar oxygen vacancies, with implications for growing high-quality $BaTiO_3$.

In the second project (Chapter 2), we study the hyperferroelectric material $LiNbO_3$ which has a soft LO mode under OCBC. We discover that the ground state of $LiNbO_3$ under OCBC is nonpolar, revealing that possessing a soft LO mode does not guarantee that a solid is HyFE. Additionally, we uncover an unusual, triple potential well phenomenon in $LiNbO_3$ under OCBC, which exhibits three stable and/or metastable states with different polarizations. This study

provides important insights into the mechanism of HyFE and reveals critical physical quantities for designing and searching for new HyFE materials.

In the third project (Chapter 3), we find that LiZnSb exhibits a giant hyperferroelectricity polarization of 0.282 C/m^2 under a -2% compressive inplane strain under OCBC, which is comparable to the polarization in prototypical ferroelectric $BaTiO_3$ under SCBC. The well depth of the electric free-energy is also unusually stable, being -332 meV, which suggests that the HyFE phase in LiZnSb is stable even under room temperature. The physical origin responsible for the giant hyperferroelectricity is found to stem from the large mode effective charge of the soft LO phonon and the large high-frequency dielectric constant of LiZnSb.

References

[1] S. Pöykkö and D. J. Chadi, Phys. Rev. Lett. **83**, 1231-1234 (1999).

[2] A. Kimmel, P. Weaver, M. Cain and P. Sushko, Phys. Rev. Lett. **109**, 117601 (2012).

[3] A. Chandrasekaran, D. Damjanovic, N. Setter and N. Marzari, Phys. Rev. B **88**, 214116 (2013).

[4] C. Paillard, G. Geneste, L. Bellaiche and B. Dkhil, J. Phys.: Condens. Matter **29**, 485707 (2017).

[5] Z. Alahmed and H. Fu, Phys. Rev. B **76**, 224101 (2007).

[6] Y. Yao and H. Fu, Phys. Rev. B **84**, 064112 (2011).

[7] M. Choi, F. Oba and I. Tanaka, Appl. Phys. Lett. **98**, 172901 (2011).

[8] P. Erhart and K. Albe, J. Appl. Phys. **102**, 084111 (2007).

[9] H. M. Duiker, P. D. Beale, J. F. Scott, C. Paz de Araujo, B. M. Melnick, J. D. Cuchiaro and L. D. McMillan, J. Appl. Phys. **68**, 5783 (1990).

[10] X. Du and I. Chen, J. Appl. Phys. **83**, 7789 (1998).

[11] M. Dawber and J. Scott, Appl. Phys. Lett. **76**, 1060 (2000).

[12] A. Tagantsev, I. Stolichnov, E. Colla and N. Setter, J. Appl. Phys. **90**, 1387 (2001).

[13] Z. Fan, C. Zhou, X. Ren and X. Tan, Appl. Phys. Lett. **111**, 252902 (2017).

[14] L. V. D. He, Phys. Rev. B **68**, 134103 (2003).

[15] O.N. Tufte and P.W. Chapman, Phys. Rev. **155**, 796 (1967).

[16] E. Cockayne and B. P. Burton, Phys. Rev. B **69**, 144116 (2004).

[17] L. Bellaiche, J. Iniguez, E. Cockayne, and B.P. Burton, Phys. Rev. B **75**, 014111 (2007).

[18] X. Ren, Nat. Mater. **3**, 91 (2004).

[19] M. Dawber, K. M. Rabe, and J. F. Scott, Rev. Mod. Phys. **77**, 1083 (2005).

[20] J. Junquera and P. Ghosez, Nature (London) **422**, 506 (2003).

[21] K. F. Garrity, K. M. Rabe, and D. Vanderbilt, Phys. Rev. Lett. **112**, 127601 (2014).

[22] H. Fu, J. Appl. Phys. **116**, 164104 (2014).

[23] P. Li, X. Ren, G.-C. Guo, and L. He, Sci. Rep. **6**, 34085 (2016).

[24] M. Khedidji, D. Amoroso, and H. Djani, Phys. Rev. B **103**, 014116 (2021).

[25] H. J. Zhao, A. Filippetti, C. Escorihuela-Sayalero, P. Delugas, E. Canadell, L. Bellaiche, V. Fiorentini, and J. Iniguez, Phys. Rev. B **97**, 054107 (2018).

.

Chapter 1: Extended planar defects of oxygen vacancies in ferroelectric $BaTiO_3$: Vacancy formation energy, condition of existence, insulating/conducting nature, and impact on ferroelectricity.

I. Introduction

Extended vacancies in ferroelectrics (FE) are of substantial importance both fundamentally and technologically. Fundamentally, extended vacancies alter the atom-atom interaction over an extensive space region [1], and break the delicate balance between the long-range and short-range interactions [2, 3], which may profoundly affect the ferroelectricity, polarization, and other materials properties. Extended vacancies may also alter the rotational instability in FEs [4, 5]. Furthermore, different from isolated defects, extended defects allow the defects to interact strongly with each other, which may possibly generate new and interesting phenomena that do not exist in perfect bulks or in bulks with isolated defects. While a majority of previous studies of defect physics in FEs focus on isolated defects [6-13], extended defects are less understood.

Technologically, extended vacancies are vitally important in understanding the long-standing problems such as polarization fatigue and aging, as well as in improving the performances of FE devices [14-16]. FE materials are widely used in non-volatile random access memories [17], actuators [18], and charge capacitors, thanks to the large and reversible spontaneous polarization, anomalous Born effective charges [19, 20], ultrahigh electromechanical response [21-23], interesting morphotropic phase boundary [24-26], large dielectric response [27, 28], and unusual phase transitions [29-31]. However, these FE applications could be considerably impaired by the existence of extended defects. For instance, defects are linked to polarization fatigue (which deteriorates the performance of FE devices) and aging (which reduces the lifetime of devices) in

polarization switching [32-36]. Oxygen vacancies were also reported to pin the domain wall [37], which may cause the imprinting of electric polarization.

Interestingly, although vacancies often hamper the performance of FE devices, they can nevertheless be technologically useful since they may produce properties that do not otherwise exist in perfect FEs. For example, oxygen vacancies in $SrTiO_3$ can generate at low temperature a strong electrical conductivity with carrier mobility as high as 10^4 $cm^2V^{-1}s^{-1}$ [38]. Furthermore, a Pb-O vacancy pair in $PbTiO_3$ was shown to enhance the local polarization by nearly 100% [39]. Meanwhile, Pb vacancies in $Pb(Sc_{0.5}Nb_{0.5})O_3$ can broaden the peak of dielectric response [40]. Moreover, vacancies were reported to be able to enhance significantly the electromechanical response in aged $BaTiO_3$ [41]. Since vacancies can be either detrimental or beneficial, it is thus technologically important to find out how to eliminate, or how to (intentionally) generate, vacancies in FEs, depending on whether we want to diminish the detrimental effects or to enhance the beneficial effects.

Despite the importance, extended vacancies in FEs are poorly understood. Many questions of fundamental relevance remain to be answered. These include: i) Whether are the extended vacancies thermodynamically stable from the fundamental point of view of energy? How much is the formation energy for extended vacancies? ii) Under what conditions can the extended vacancies be generated or annihilated, by which scientists can enhance the beneficial properties or eliminate the harmful effects? iii) How are ferroelectricity and polarization affected by the extended vacancies? Will ferroelectricity persist despite the existence of extended vacancies? iv) Extended vacancies may appear with different charge states. How does the impact of extended vacancies depend on the charge states?

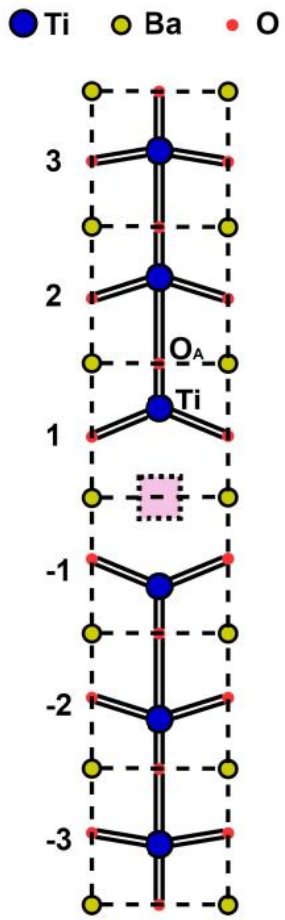

FIG. 1. 1: Schematic illustration (side view) of the planar vacancies in an $1 \times 1 \times 6$ supercell, where an oxygen vacancy is indicated by a dotted square at the center of the supercell. Individual bulk cells along the c-axis are marked as -3, -2, -1, 1, 2, and 3, depending on their distances from the vacancy. In perfect $BaTiO_3$, the Ti atom in cell 1 is bonded to two oxygen atoms (O_A and O_B) along the *c*-axis. In $BaTiO_3$ with planar oxygen vacancies, the oxygen atom O_B in cell 1 is removed, and the Ti atom is pulled toward the oxygen atom O_A due to the broken Ti-O_B bond.

In this project we investigate by first-principles density functional theory the extended planar oxygen vacancies in ferroelectric $BaTiO_3$, where oxygen vacancies are formed on an atomic plane. $BaTiO_3$ is a prototypical ferroelectric solid and is one of commonly used materials in FE devices. Meanwhile, oxygen vacancies are an important type of native defects in FEs. $BaTiO_3$ with planar oxygen vacancies to be investigated here is illustrated schematically in Fig.1.1, where an oxygen vacancy is created at the center of a $1 \times 1 \times 6$ supercell by removing one oxygen atom. Due to the

periodicity along the lateral *ab*-plane directions, the oxygen vacancies thus created are extended on an atomic plane and will interact strongly with each other. Obviously our study differs from the previous work [6-13] where isolated defects were reported. Extended planar vacancies are potentially more interesting.

The purpose of this study is to determine how much energy is needed to form the planar oxygen vacancies in ferroelectric $BaTiO_3$, and to understand how the planar vacancies affect ferroelectricity. We obtain the following main results: (i) The formation energy ΔH of planar V_O^{2+} vacancies can be interestingly small (on the order of merely 0.54 eV) even under the oxygen-rich condition, showing that planar oxygen vacancies are not as difficult to form as commonly thought. (ii) We further systematically determine the optimal condition to eliminate (or generate) the planar V_O^q vacancies of all three charge states, which is technologically relevant in terms of growing high-quality $BaTiO_3$. (iii) Planar V_O^{2+} vacancies drastically reduce the ferroelectricity in $BaTiO_3$, which provides a pivotal (theoretical) evidence that the planar oxygen vacancies could be the origin of causing polarization fatigue and imprinting. (iv) The length of polarization dead layer caused by planar V_O^{2+} vacancies in $BaTiO_3$ is determined to be large and around 72Å. showing that extended oxygen vacancies are very harmful to electric polarization. Moreover, we provide microscopic insight aimed to obtain a deep understanding on the physical behaviors of planar oxygen vacancies.

II. Theoretical methods

A. Determination of vacancy formation energy

Oxygen vacancies in $BaTiO_3$ can exist in three different charge states — V_O^0, V_O^{1+}, and V_O^{2+}. These vacancies will be denoted in general as V_O^q, where q is the charge state of the vacancy. The formation energy of an oxygen vacancy, ΔH, is defined as the energy that is needed to move an oxygen atom from a perfect $BaTiO_3$ solid to the *atomic* reservoir of oxygen. If the vacancy carries

q charge, ΔH also includes the energy that is needed to move q electrons from the $BaTiO_3$ solid to the *electron* reservoir [42, 43].

Quantitatively, the vacancy formation energy is the energy difference between the initial state ($E_{initial}$) and the final state (E_{final}), i.e., $\Delta H = E_{final} - E_{initial}$. Here the initial state is the perfect $BaTiO_3$, of which the total energy per supercell is denoted as $E[BTO]$. The final state includes three parts [42, 43]: (i) The defective $BaTiO_3$ solid containing vacancies V_O^q, of which the total energy per supercell is denoted as $E[V_O^q]$; (ii) Vacated O atoms that are placed in the atomic reservoir of oxygen, where the relative chemical potential of the atomic reservoir is μ_O with respect to the reference energy E_O (Here E_O is chosen to be the energy of one oxygen atom in an O_2 molecule [10, 11]; (iii) q electrons in the electron reservoir, where the relative chemical potential of the electron reservoir is μ_e with respect to the Kohn-Sham orbital energy ε'_{VBM} of the valence band maximum (VBM) of defective $BaTiO_3$ with vacancies. Denote the orbital energy of the VBM of perfect $BaTiO_3$ as ε_{VBM}. ε'_{VBM} and ε_{VBM} are related by $\varepsilon'_{VBM} = \varepsilon_{VBM} + \Delta\bar{V}$, where $\Delta\bar{V}$ is the difference in potential far away from the defect. $\Delta\bar{V}$ is computed by using the semi-core state of Ti $3s$ orbital [10, 11], since Ti $3s$ state is highly localized with very little energy dispersion---and the difference in the orbital energy of this state in different systems thus reflects $\Delta\bar{V}$. By combining the different parts in the above, the formation energy ΔH per V_O^q vacancy is then given by the equation [42, 43]

$$\Delta H = E\left[V_O^q\right] + (E_O + \mu_O) + q(\varepsilon_{VBM} + \Delta\bar{V} + \mu_e) - E[BTO]. \quad (1)$$

Large ΔH implies that vacancy V_O^q is difficult to form by requiring more energy. Charge correction is included. Details on how to calculate each term in Eq.(1) were given in Ref. [10, 11].

Vacancy formation energy depends on the chemical potential μ_O of the oxygen atomic reservoir and the chemical potential μ_e of the electron reservoir, as shown in Eq.(1). The allowable

range of μ_O need be determined using the thermodynamical constraints that no secondary phases are formed during the growth of $BaTiO_3$ [10, 11, 42]. Using the thermodynamical constraints, we determine that μ_O can vary from -5.7 eV to 0 eV, where the lower limit μ_O = -5.7 eV corresponds to the oxygen-poor condition for growing $BaTiO_3$ while the upper limit μ_O = 0 eV corresponds to the oxygen-rich condition. The chemical potential μ_e of the electron reservoir can vary from the valence band maximum to the conduction band minimum (CBM) of the $BaTiO_3$ solid, as required by the thermodynamical equilibrium between the $BaTiO_3$ solid and the electron reservoir [42, 43].

Technically we use the first-principles density functional theory within the local density approximation (LDA) [44], as implemented in Quantum Espresso [45], to perform the structural optimization and total energy calculations. Norm-conserving pseudopotentials of Troullier and Martins type are used [46]. The semi-core orbits of Ti $3s$ and $3p$ are treated as valence states to ensure better accuracy; details of pseudopotential generation were given in Ref. [47]. The energy cutoff for the plane-wave expansion of single-pproject Kohn-Sham states is 90 Ry, which is sufficient. We consider tetragonal $BaTiO_3$ with P4mm symmetry. For tetragonal bulk $BaTiO_3$, we obtain the inplane lattice constant a = 3.929Å and the tetragonality c/a = 1.007, which agree well with the values a = 3.945Å and c/a = 1.009 in other calculation [48].

In tetragonal $BaTiO_3$ with P4mm symmetry, there are two inequivalent oxygen Wyckoff sites according to the group theory [49]: one is located on the base plane of an oxygen octahedron, and the other is located at the apex of the octahedron. It was previously shown in the study of isolated defects that the vacancy formation energies at two different sites are very close [10, 11], since the c/a ratio of tetragonal $BaTiO_3$ is close to 1.0, and the chemical bonds at two oxygen sites are similar. Furthermore, the oxygen vacancies at the base plane do not affect strongly the ferroelectricity and are of less interest. We thus choose to consider the oxygen vacancies at the

apical site. We use the $1 \times 1 \times 6$ supercell as shown in Fig.1.1. Different charge states (V_O^0, V_O^{1+}, and V_O^{2+}) of oxygen vacancies are considered in our calculations. For each charge state, the atomic positions and cell parameters are relaxed. A Monkhorst-Pack k-mesh of $6 \times 6 \times 2$ is used in all supercell calculations [50].

B. Determination of electric polarization

Both ions and electrons contribute to electric polarization. Contribution from ions can be calculated straightforwardly using point charges as $\mathbf{P}_{ion} = \frac{1}{\Omega}\sum_i q_i \boldsymbol{r}_i$, where q_i is the charge of ion i and $\boldsymbol{r}_i$ is the position. Contribution from electrons is nontrivial since electrons in solids cannot be treated as point charges, and this contribution need be calculated using the Berry geometric-phase approach, as formulated in the modern theory of polarization (MTP) [51, 52],

$$\mathbf{P}_{\text{el}} = \frac{2e}{(2\pi)^3}\int d\mathbf{k}_\perp \,\text{Im ln}\prod_j \det\,(< u_{m,\mathbf{k}_\parallel^j}|u_{n,\mathbf{k}_\parallel^{j+1}} >), \qquad (2)$$

where $u_{n,\mathbf{k}_\parallel}$s are the cell-periodic Bloch part of wave functions for occupied valence states; $\mathbf{k}_\perp$ and $\mathbf{k}_\parallel$ are the components of the electron wave vector perpendicular and parallel to the polarization direction, respectively. Electronic contribution $\mathbf{P}_{\text{el}}$ can be further analyzed using the theory of polarization structure [53]. Here one may argue whether MTP is valid for charged systems since the polarization of charged systems is not translation invariant. Recently, Raeliarijaona and Fu showed rigorously that, even for charged systems, the *change* of polarization is still translation invariant and is physically meaningful, and hence the modern theory of polarization remains valid in computing the change of polarization [54].

We use the following scheme to determine the electric polarization for defected $BaTiO_3$ with vacancies. We first perform structural optimization for $BaTiO_3$ with V_O^q vacancies of charge state q. Denote the optimized atomic configuration as $\{\mathbf{r}_i^{\text{opt}}\}$. We then generate a centrosymmetric

atomic configuration, $\{\mathbf{r}_i^c\}$, of which the magnitude of polarization is zero by symmetry. Next we adiabatically move atomic positions from $\{\mathbf{r}_i^c\}$ to $\{\mathbf{r}_i^{\mathrm{opt}}\}$ by constructing a series of intermediate configurations according to $\mathbf{r}_i = \mathbf{r}_i^c + \lambda(\mathbf{r}_i^{\mathrm{opt}} - \mathbf{r}_i^c)$, where $0 < \lambda < 1$. For each intermediate configuration we compute the electric polarization in order to determine the polarization branch and to ensure the continuity of the computed polarization value along the path. The polarization value at $\lambda = 1$ is the needed polarization that corresponds to the optimized configuration of vacancies V_O^q. This procedure of using intermediate configurations is critical for determining the electric polarization in large *supercells*, since polarization can easily jump discontinuously to other branches of different polarization quanta [54].

III. Results and discussions

A. Vacancy formation energies and charge states

Whether or not planar V_O^q vacancies of a given q charge state can occur in $BaTiO_3$ depends on the formation energy ΔH. A lower formation energy indicates that vacancies V_O^q are more likely to occur by requiring a less energy. Here it helps to be (slightly) more quantitative. Using the oxygen-vacancies concentrations which were often observed in experiments, it was quantitatively estimated that, when ΔH is below 1.5 eV, vacancies are very likely to occur [54]. When ΔH is between 1.5 eV and 4.0 eV, vacancies are still possible to occur, but with less probability. On the other hand, if ΔH is near or above 4.0 eV, vacancies will be difficult to form.

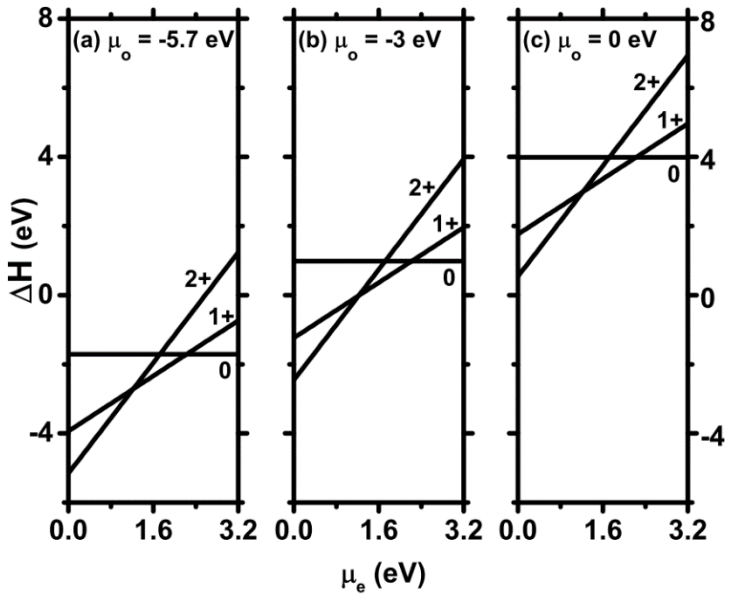

FIG. 1. 2: Vacancy formation energy ΔH as a function of the chemical potential μ_e of the electron reservoir, at the following chemical potential μ_O of the oxygen reservoir: (a) $\mu_O = -5.7$ eV (oxygen poor), (b) $\mu_O = -3.0$ eV, and (c) $\mu_O = 0$ eV (oxygen rich). Charge state q of vacancy is labelled near the corresponding line.

The calculated formation energies of planar oxygen vacancies are shown in Fig.1.2(a)-(c) as a function of the chemical potential μ_e of the electron reservoir, for three different chemical potentials μ_O of the oxygen reservoir. We use the experimental band gap of 3.2 eV as the varying range of μ_e. Note that ΔH depends on both μ_e and μ_O, as described in Eq.(1). Fig.1.2 contains a rich variety of knowledge about the energetics and stabilities of planar oxygen vacancies, from which several key observations can be made as follows.

First, we see from Fig.1.2(a) that, under the oxygen-poor condition, the vacancy formation energies of the three charge states (V_O^{2+}, V_O^{1+}, and V_O^0) are largely negative, which indicates that the formation of vacancies requires no energy. The planar oxygen vacancies of all three charge states will thus spontaneously occur and vacancies will be abundant under the oxygen-poor

condition. This is consistent with our intuition since, under the oxygen-poor condition, there are insufficient oxygen atoms in $BaTiO_3$, and oxygen vacancies will thus be amply present.

Next let us turn attention to the oxygen-rich condition in Fig.1.2(c). Interestingly, we discover that planar V_O^{2+} vacancies may occur even under the oxygen-rich condition. More specifically, Fig.1.2(c) reveals that, when μ_e is close to 0, ΔH of planar V_O^{2+} vacancies is merely 0.54 eV, and formation of this charge-state vacancies thus requires only a small amount of energy, indicating that extended V_O^{2+} vacancies may easily form under the oxygen-rich condition. This is rather surprising since, according to the common wisdom, oxygen vacancies should be difficult to occur while oxygen is rich and sufficient. Our result suggests that one need be cautious in applying the common wisdom to the extended oxygen vacancies in FEs. One possible reason for the low formation energy of planar V_O^{2+} vacancies in FEs, despite oxygen is rich, is explained later in Sec.III,(E).

Furthermore, we can determine from Fig.1.2(c) which charge state of vacancy is most stable at a given chemical potential μ_e. Specifically, when $\mu_e < 1.22$ eV, V_O^{2+} is most stable since its formation energy is lower than both V_O^{1+} and V_O^0 in Fig.1.2(c). When μ_e is increased to $1.22 < \mu_e < 2.22$ eV, V_O^{1+} becomes most stable. When μ_e is further increased to $\mu_e > 2.22$ eV, neutral V_O^0 is most stable. We thus see that, by varying μ_e, each of the three charge states (namely V_O^{2+}, V_O^{1+}, and V_O^0) can be made most stable for the extended planar oxygen vacancies. This knowledge (regarding which charge state is most stable in a given μ_e region) is useful, for it can be utilized to grow the planar oxygen vacancies of a desired charge state. Note also that this knowledge does not depend on the choice of the chemical potential μ_O of the oxygen reservoir, since it is the same in Fig.1.2(a) and Fig.1.2(b).

Our theoretical results that planar oxygen vacancies can be formed in $BaTiO_3$ with reasonably small formation energies call for experiments to verify. Nowadays, the layer-by-layer epitaxial growth of perovskite oxides, enabled by pulsed laser deposition (PLD) [55] or molecular beam epitaxy (MBE) [56], shall (in principle) make it possible to fabricate oxide materials with extended defects. Although no planar oxygen vacancies have been experimentally grown per se, evidence for the existence of extended clusters of oxygen vacancies was reported in perovskite oxides [57, 58], which is to some extent consistent with our theory.

B. Condition to generate (or eliminate) planar oxygen vacancies

One intriguing question about planar oxygen vacancies is to find the condition (to be termed as "Condition G") under which these vacancies can be easily *generated* for all three charge states, for the purpose of enhancing the beneficial effects of oxygen vacancies. This question is important for two reasons: (i) FEs with extended oxygen vacancies may have technologically-relevant properties that are not available in perfect bulk, and (ii) the knowledge of this condition may be useful in experiments to deliberately grow $BaTiO_3$ with extended V_O^q vacancies.

In Fig.1.2(b), at $\mu_O = -3.0$ eV (i.e., as μ_O is located near the middle point between the oxygen-rich and oxygen-poor conditions), the vacancy formation energies of all three charge states are small and around 0.6 eV, when μ_e is in the range from 1.6 to 2.4 eV. As a result, planar oxygen vacancies of each of the three charge states may easily occur at the considered μ_O and μ_e. Therefore, the Condition G under which all three charge states of vacancies can be easily generated is $\mu_O \approx -3.0$ eV and $1.6 < \mu_e < 2.4$ eV. Furthermore, as shown in Fig.1.2(b), when $1.6 < \mu_e < 2.4$ eV, one may change the most-stable charge state by slightly altering μ_e. Note that changing the charge state of defects is often technologically useful since it can drastically tune the transport properties.

Another question regarding planar oxygen vacancies is to figure out the condition (to be termed "Condition E") under which all three charge states of planar oxygen vacancies can be easily *eliminated* (i.e., these vacancies are difficult to form), for the purpose of minimizing the detrimental effects of oxygen vacancies. Our study also yields the Condition E. From Fig.1.2(c), we see that, when $\mu_O = 0$ eV and when μ_e is between 2.4 eV and 3.2 eV, the formation energies of all three charge states are nearly 4.0 eV or above, suggesting that planar oxygen vacancies are unlikely to occur. Therefore, the optimal condition to eliminate the extended oxygen vacancies (i.e., Condition E) is to grow $BaTiO_3$ under the oxygen-rich condition and at the same time adjust μ_e to be near the conduction band minimum. Considering that the extended oxygen vacancies are one key class of defects that may cause the fatigue and aging in polarization switching [15], the Condition E obtained here to eliminate the planar oxygen vacancies could be useful in terms of growing $BaTiO_3$ solids that will improve the performance of FE devices.

We also estimate how our calculation results may be affected if the LDA band gap is corrected. Ideally one would prefer the hybrid (such as HSE) density functional calculations to correct the band gap [59]. However, the computation of HSE hybrid-functional calculations is time consuming, particularly for large-supercell vacancy calculations. We thus decide to perform LDA+U calculations which largely improve the band gap but with manageable computation. We choose a U=6eV value for Ti in our calculations, since this U value produces a direct band gap of 3.15 eV at zone-center Γ for perfect bulk $BaTiO_3$, which is comparable to the experimental band gap of 3.20 eV. In contrast, the direct band gap of LDA is only 2.40eV at the Γ point. Using the LDA+U method, we find that the formation energies are modified, but by a rather small change of 0.30eV, 0.35eV, and 0.55eV for planar V_O^0, V_O^{1+}, and V_O^{2+} vacancies, respectively. As discussed quantitatively in Ref. [54], in order for oxygen V_O^q vacancies to change their probability from

"being likely to occur" to "being unlikely to occur", the formation energy needs to change from 1.5eV to 4.0eV, i.e., by about 2.5eV. The modifications (on the order of 0.35eV) of the formation energies due to LDA+U calculations are considerably smaller than 2.5eV. Therefore, the LDA+U calculations and the band-gap corrections do not qualitatively alter the main conclusions in our study. Furthermore, from the LDA+U calculations, the *relative* change in the formation energies, for instance the formation energy of planar V_O^{1+} vacancies with respect to that of planar V_O^{2+} vacancies, is even smaller (only 0.05eV), which reveals that the transition chemical potentials (μ_e) between different charge states are nearly unchanged.

C. Insulating or conducting

Defects can cause an insulating solid to become conducting since these defects may introduce extra mobile charges of electrons or holes. It is thus relevant to determine whether the defected system is insulating or metallic. For defects in ferroelectric solids, this question is even more critical since mobile electrons or holes in FEs may effectively screen (and thus alter) the electric polarization, if ferroelectricity is to persist.

The densities of states (DOS) of $BaTiO_3$ with planar V_O^q vacancies are shown in Fig.1.3, along with the DOS of perfect $BaTiO_3$. In Fig.1.3, the energy levels of different systems are aligned by using the Kohn-Sham orbital energy of Ti semi-core $3s$ state. After alignment, it is physically meaningful to compare the relative orbital energies in different systems if needed, although this comparison is not critical in the present study.

Several conclusions can be made from Fig.1.3: (i) For both V_O^0 and V_O^{1+} planar vacancies, the Fermi level is located within the conduction bands [Fig.1.3(b) and Fig.1.3(c)], and these two systems thus have mobile electrons and are conducting. (ii) In contrast, for V_O^{2+} vacancies in Fig.1.3(d), the Fermi level is located at the top of valence band, by which a sizable band gap is

formed between the occupied and unoccupied states. $BaTiO_3$ with planar V_O^{2+} vacancies is thus an insulator. (iii) Comparing V_O^0 in Fig.1.3(b) with V_O^{1+} in Fig.1.3(c), we see that neutral V_O^0 has a larger DOS at the Fermi level, and the charge state q=0 may thus enhance the conductivity and/or superconductivity than q=1+. (iv) When q increases from Fig.1.3(b) to Fig.1.3(d), the Fermi level decreases.

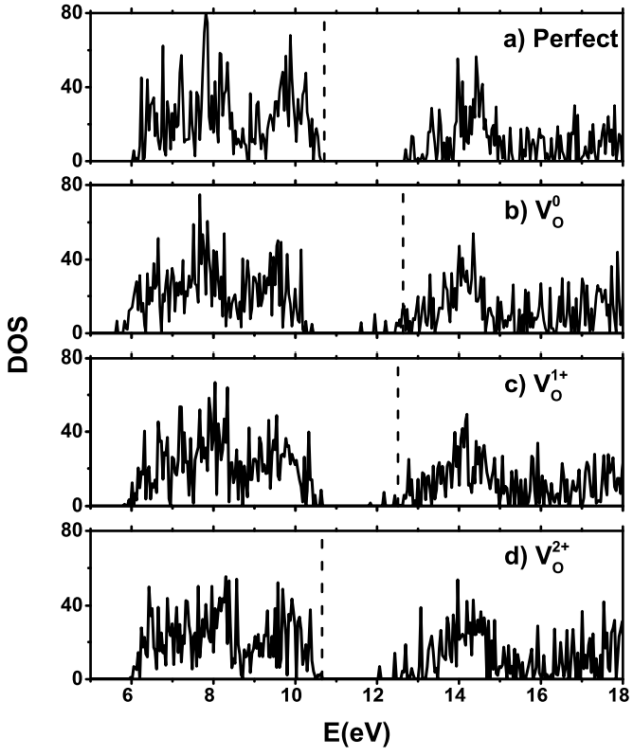

FIG. 1. 3: Density of states (DOS) of the following systems: (a) Perfect $BaTiO_3$; (b)-(d): $BaTiO_3$ with planar V_O^0 vacancies (b), planar V_O^{1+} vacancies (c), planar V_O^{2+} vacancies (d). Dashed line indicates the Fermi level in each system.

The finding of the insulating nature of planar V_O^{2+} vacancies is nontrivial. It reveals that no mobile electrons and holes are available to screen the polarization in $BaTiO_3$ with V_O^{2+}. In contrast, the conducting nature of planar V_O^0 or V_O^{1+} vacancies indicates that polarization will be screened (or at least partially screened) by the mobile electrons.

The theoretical result that $BaTiO_3$ with planar V_O^{2+} vacancies is an insulator can be intuitively understood as follows. In $BaTiO_3$ solid, outside each O atom, there are two additional electrons which are transferred from Ti or Ba cations. These two additional electrons are strongly bonded to the O atom, due to the strong electronegativity of oxygen atoms. When an O atom (named "atom X") is removed from $BaTiO_3$ to create a vacancy, the two additional electrons outside atom X prefer to stay with this atom (rather than staying inside the $BaTiO_3$ solid) in order to lower the energy of the total system. In other words, we need to remove both atom X and two additional electrons, which leads to that each V_O vacancy carries a 2+ charge. Furthermore, because the two additional electrons outside atom X are removed, these electrons will not be donated to the $BaTiO_3$ solid, and there will be no mobile electrons inside $BaTiO_3$, which makes it an insulator.

While both perfect $BaTiO_3$ [Fig.1.3(a)] and defected $BaTiO_3$ with V_O^{2+} [Fig.1.3(d)] are insulating, their band gaps nevertheless differ. The LDA band gap (~1.3 eV) of defected $BaTiO_3$ with V_O^{2+} vacancies is smaller than the LDA gap (~2.0 eV) of perfect $BaTiO_3$. In FEs, a reduction in band gap could be technologically useful in, for instance, improving the power conversion efficiency in photovoltaic applications [60, 61].

D. Impact on ferroelectricity

One critical subject about extended oxygen vacancies in FEs centers on how they may affect ferroelectricity [1, 14]. Here we attempt to shed light on this important topic. Note that the *ab-initio* determination on how charged defects affect ferroelectricity is a standing challenge despite its importance [52], since the polarization itself in *charged* systems is not translation invariant. The determination becomes possible after it was recently proved that the *change* of polarization in charged systems is translation invariant and thus physically meaningful [54].

From the densities of states in Fig.1.3, we have determined that $BaTiO_3$ with planar V_O^{2+} vacancies is an insulator, and therefore ferroelectricity can, in principle, exist for this charge state since there are no mobile charges to screen the polarization. The challenge is to find how large the polarization will be quantitatively in $BaTiO_3$ with planar V_O^{2+} vacancies. Will the polarization be similar to (or drastically different from) the value in perfect $BaTiO_3$? On the other hand, for planar oxygen vacancies of two other charge states (i.e., V_O^0 and V_O^{1+}), the systems are metallic, and electric polarization is ill-defined for metallic systems.

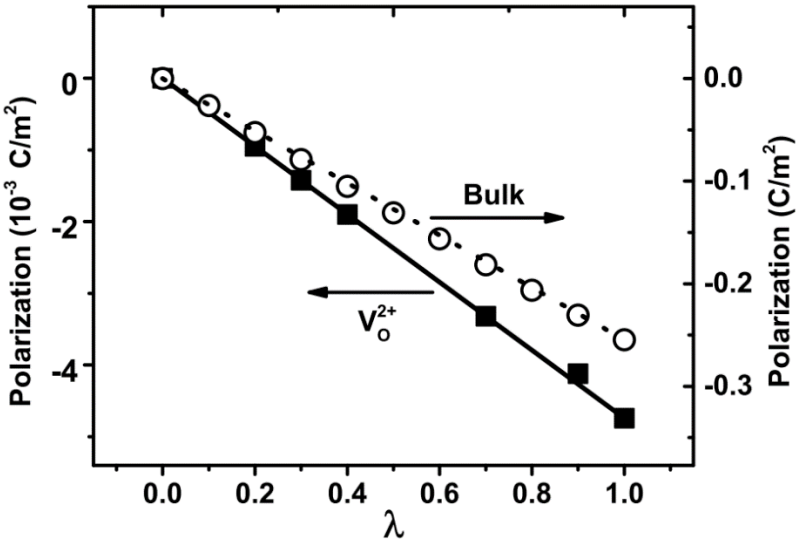

FIG. 1. 4: Polarization as a function of the λ parameter, for defective $BaTiO_3$ with planar V_O^{2+} vacancies (solid squares and solid line, using the left vertical axis), and for perfect $BaTiO_3$ (empty circles and dotted line, using the right vertical axis). λ=0 corresponds to the centro-symmetric structure, and λ=1 corresponds to the LDA-optimized structure for each system. Note that the left vertical axis is in units of 10^{-3} C/m^2. The polarization value at the final configuration λ=1 is determined to be $P = -4.7 \times 10^{-3}$ C/m^2 for $BaTiO_3$ with V_O^{2+} vacancies, and $P = -0.25$ C/m^2 for perfect $BaTiO_3$ without vacancies.

We go one step further and perform the Berry-phase calculations to determine the electric polarizations in defective $BaTiO_3$ with planar V_O^{2+} vacancies as well as in perfect bulk, using the modern theory of polarization [51, 52] and the intermediate configurations as described in

Sec.II,(B). Fig.1.4 depicts the polarization as a function of the λ parameter which controls the intermediate configurations.

For $BaTiO_3$ with planar V_O^{2+} vacancies (see the solid-square symbols and solid line in Fig.1.4), we observe the following. (i) The polarization value at λ=0 is zero, showing that this configuration is indeed centro-symmetric and can thus serve as the zero-reference point for determining the change in polarization, as it should be. (ii) The polarization at λ=1 is found to be $P = -4.7 \times 10^{-3}\ C/m^2$, which is the polarization value for the optimized structure of $BaTiO_3$ with planar V_O^{2+} vacancies.

Meanwhile, for perfect bulk $BaTiO_3$ (see the empty circles and dotted line in Fig.1.4), we find that the polarization is $P = -0.25\ C/m^2$ at λ=1. This theoretical value of polarization agrees well with the experimental measurement results [62, 63] of $|P| = 0.26\ C/m^2$, indicating that our polarization calculations are rather reliable.

The results in Fig.1.4 reveal an important conclusion, that is, the electric polarization in $BaTiO_3$ with planar V_O^{2+} vacancies is more than 50 times smaller than the value in perfect bulk. In other words, we find that planar V_O^{2+} vacancies almost entirely eliminate the ferroelectric polarization, showing that the extended planar oxygen vacancies in $BaTiO_3$ generate a devastating effect on ferroelectricity.

The calculation results also reveal a drastic difference between *extended* oxygen vacancies and *isolated* oxygen vacancies. A previous study has reported that strong ferroelectricity with a polarization of 0.24 C/m^2 persists in $BaTiO_3$ with *isolated* V_O^{2+} vacancies [54], which is close to the bulk value of 0.25 C/m^2. In sharp contrast, for *extended* planar V_O^{2+} vacancies, we find in Fig.1.4 that the polarization nearly vanishes. Therefore, the two types of oxygen vacancies produce very different effects on macroscopic polarization.

Moreover, our studies have significant implication on polarization fatigue in FEs. First, our current results confirm that planar oxygen vacancies indeed can give rise to polarization fatigue in FEs by diminishing the polarization, which supports the phenomenological model proposed in Ref. [15]. Second, our results suggest that polarization fatigue in switching is likely caused by extended vacancies (namely, not isolated vacancies), since it is the former (not the latter) that drastically reduces the polarization.

E. Origin of the vanished polarization and microscopic insight

The drastic reduction of polarization caused by planar V_O^{2+} vacancies is interesting and may explain the important phenomenon such as polarization fatigue. We next attempt to provide microscopic insight in order to understand the origin of the declining polarization. For this purpose, we investigate the Ti-O relative displacement ΔZ along the tetragonal *c*-axis direction, for each TiO_2 layer in the LDA-optimized structures of defected $BaTiO_3$ with V_O^q vacancies. ΔZ is defined as $\Delta Z = Z_{Ti} - Z_O$, where Z_{Ti} and Z_O are the *z*-component atomic positions of Ti and O, respectively. ΔZ is an indicator of local polarization. Since each supercell of vacancy calculations consists of six bulk cells and we need to address the Ti-O displacement in each bulk cell, we thus label, as schematically illustrated in Fig.1.1, the six individual bulk cells as -3, -2, -1, 1, 2, 3 based on their distances from the vacancy (which is located at the center of the supercell). Cells ±1 are close to the vacancy, while cells ±3 are farther away from the vacancy. The obtained Ti-O relative displacements are shown in Fig.1.5(a)-(c) for V_O^{2+}, V_O^{1+}, and V_O^0, respectively. Let us first focus on V_O^{2+} in Fig.1.5(a).

Several important findings can be obtained in Fig.1.5(a): (i) ΔZ in cell 1 is found remarkably large, with a magnitude $\Delta Z = 0.36$Å. To appreciate the size of this ΔZ, we compare it with the Ti-O displacement in *perfect* bulk $BaTiO_3$ with P4mm symmetry, which is 0.10Å according to our

calculation. ΔZ in cell 1 for planar V_O^{2+} vacancies is thus ~360% times of the counterpart in perfect $BaTiO_3$. This reveals that the local dipole moment is strongly enhanced in cell 1 near the planar vacancies, supporting the result of Ref. [39]. (ii) ΔZ decreases drastically from cell 1 to cell 3, being quantitatively $\Delta Z = 0.17$Å in cell 2 and $\Delta Z = 0.05$Å in cell 3. It shows that the impact of planar vacancies declines when cells move away from the vacancies, as a result of the strong dielectric screening in FEs [64-66]. (iii) Interestingly, ΔZ of cell 1 and ΔZ of cell -1 in Fig.1.5(a) have an equal magnitude, but opposite signs, showing that the strong local dipole moments induced by planar vacancies in cells 1 and -1 are cancelled. This explains why the total polarization, obtained in Fig.1.4 from the Berry-phase calculations, nearly vanishes for V_O^{2+}.

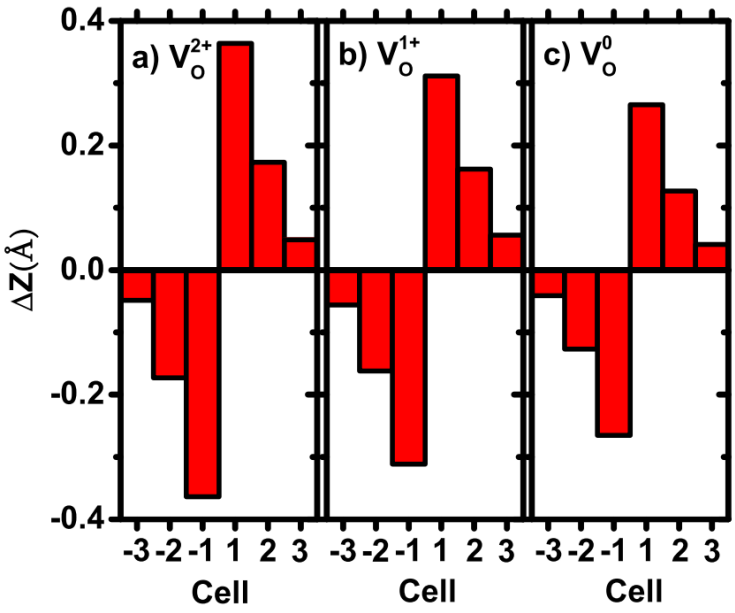

FIG. 1. 5: Ti-O relative displacements ΔZ in individual bulk cells (as labelled by the horizontal axis), for the optimized atomic configurations of the following planar vacancies: (a) V_O^{2+}, (b) V_O^{1+}, and (c) V_O^0.

Furthermore, additional microscopic insight can be gained by contrasting the ΔZ displacements of different charge states in Fig.1.5. Two key outcomes can be drawn here. First, we recognize that, when charge state q decreases from Fig.1.5(a) to Fig.1.5(c), ΔZ in cell 1

decreases notably. Quantitatively, we find that ΔZ in cell 1 is 0.36Å , 0.31Å , and 0.27Å for $q = 2+, 1+, \text{and } 0$, respectively. Second, ΔZ in cell 1 for neutral V_O^0 [Fig.1.5(c)] nevertheless remains to be much larger than the ΔZ value (0.10Å) in perfect bulk $BaTiO_3$. Moreover, for all three charge states which include *q*=1+ in Fig.1.5(b) and *q*=0 in Fig.1.5(c), ΔZ in cell 1 and ΔZ in cell -1 exhibit a mirror symmetry by having opposite signs.

One may wonder what causes ΔZ in cell 1 to decline from Fig.1.5(a) to Fig.1.5(c) as charge state *q* decreases. We find that it may be answered by considering the Coulomb interaction. More specifically, for *positively* charged vacancies such as V_O^{2+} or V_O^{1+}, the vacancies will repel Ti cations and attract O anions due to the Coulomb interaction. As a result, Ti^{4+} ions will move away from the vacancy plane, while O^{2-} ions will move toward the vacancy plane, leading to that ΔZ in cell 1 is enhanced in V_O^{2+} or V_O^{1+} than in neutral V_O^0.

Another question concerns why, for *neutral* V_O^0, ΔZ of cell 1 in Fig.1.5(c) remains to be much larger than the value in perfect bulk $BaTiO_3$. Considering that neutral V_O^0 vacancies do not generate strong Coulomb forces, it is rather interesting that ΔZ in cell 1 of V_O^0 (namely $\Delta Z = 0.27$Å) is still remarkably larger than the value $\Delta Z = 0.1$Å) in perfect bulk. This large ΔZ in cell 1 for V_O^0 can be explained by the broken Ti-O bond when vacancies are created. In perfect $BaTiO_3$, one Ti atom is bonded along the *c*-axis to two apical O atoms, one above and one below Ti. Let us denote these two O atoms as O_A and O_B. When an oxygen vacancy is created by removing, e.g., atom O_B, the Ti-O_B bond in the O-Ti-O chain along the *c*-axis is then broken as schematically shown in Fig.1.1 for the Ti atom in cell 1, and the considered Ti atom will be attracted strongly toward the remaining O_A atom in order to lower the total energy. This gives rise to a large position change of the Ti atom with respect to the O atoms in the same TiO_2 layer (and thus a large ΔZ in cell 1) for the neutral V_O^0 vacancies.

The above microscopic insight on ΔZ may also explain why planar V_O^{2+} vacancies can occur with a low formation energy even under the oxygen-rich condition [as seen in Fig.1.2(c) when μ_e is near 0]. For V_O^{2+}, notice that the ΔZ in cell 1 is contributed by both the Coulomb repulsion mechanism (since V_O^{2+} is positively charged) and the broken Ti-O bond mechanism (since V_O^{2+} breaks the Ti-O_B bond), and the combination of these two mechanisms leads to a gigantic $\Delta Z = 0.36$Å in cell 1. This large ΔZ considerably shortens the distance between Ti and O_A atoms and allows these two atoms to interact strongly, which stabilizes the planar V_O^{2+} vacancies and lowers the formation energy.

F. Polarization dead layer of planar oxygen vacancies

Denote the spacing distance between two adjacent oxygen-vacancy planes as *S*. Our calculations so far are obtained for $1 \times 1 \times 6$ supercell, which corresponds to the experimental situation where *S* is around 24Å (Here, to be consistent, the experimental lattice constant of 4Å is used). One interesting question then arises: what will happen if the spacing *S* is increased? At what spacing, will ferroelectricity appear? Another important topic of technological relevance centers on how much is the length of the polarization dead layer, to be caused by the planar oxygen vacancies. To address these important questions, we focus on the planar V_O^{2+} vacancies (since, only for V_O^{2+} charge state, electric polarization is well defined), and we perform additional calculations using $1 \times 1 \times 12$, $1 \times 1 \times 18$, and $1 \times 1 \times 24$ supercells, which correspond to the experimental situations with spacing *S* being around 48Å , 72Å , and 96Å , respectively.

The obtained Ti-O relative displacements ΔZ are given in Fig.1.6(a) and Fig.1.6(b) for the $1 \times 1 \times 18$ and $1 \times 1 \times 24$ supercells, respectively. Fig.1.6(a) reveals that, when *S* is increased to 72Å , ΔZ continues to be symmetric, being positive at one side of oxygen-vacancy plane and negative at the other side. Polarization remains to be vanishing. Furthermore, the magnitude of ΔZ

in cell 1 (0.38Å) in Fig.1.6(a) is nearly the same as in Fig.1.5(a), showing that the *local* structure near the vacancy plane is very similar and does not depend on the spacing distance *S*.

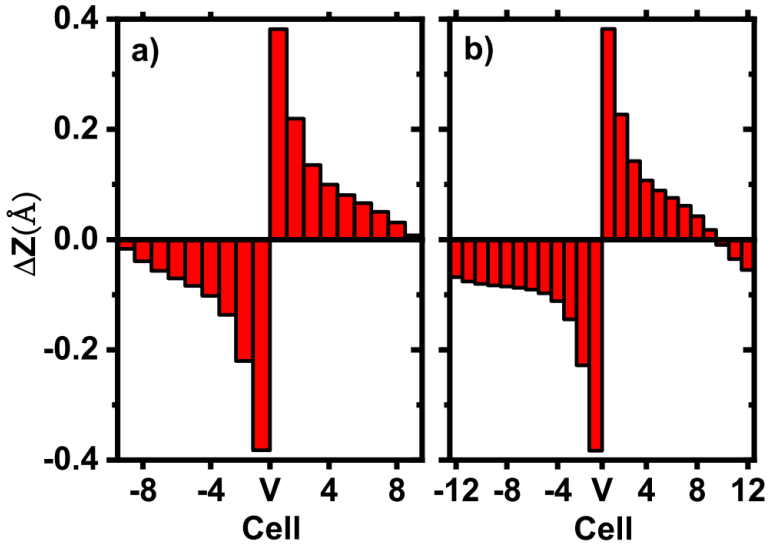

FIG. 1. 6: Ti-O relative displacements ΔZ in individual bulk cells (as labelled by the horizontal axis) in $BaTiO_3$ with planar V_O^{2+} vacancies for the following supercells: (a) $1 \times 1 \times 18$; (b) $1 \times 1 \times 24$ supercells. V on the horizontal axis indicates the location of the oxygen-vacancy plane.

However, and interestingly, when spacing *S* is increased to 96Å , ΔZ in Fig.1.6(b) becomes notably different. More specifically, we see in Fig.1.6(b) that (i) while ΔZ in the left side of vacancy plane is all negative in different bulk cells, ΔZ in the right side of vacancy plane is no longer all positive, and instead it changes from positive in cell 1 to negative in cell 12. As a result, ΔZ ceases to be centro symmetric, which is an indication that ferroelectricity emerges in Fig.1.6(b). (ii) Notice that both ΔZ in the left boundary (cell -12) and ΔZ in the right boundary (cell 12) in Fig.1.6(b) are negative and point at the same direction. Therefore, the local polarizations at two sides of the oxygen-vacancy plane do not cancel. (iii) The magnitude of ΔZ in cell -12 of Fig.1.6(b) is considerably large (0.068Å), and is in fact comparable to ΔZ (0.10Å) in perfect $BaTiO_3$.

Furthermore, we calculate the electric polarization for the $1 \times 1 \times 24$ supercell, and the value is found to be -0.038 C/m^2, which is nonzero. This confirms that ferroelectricity indeed emerges

when the spacing *S* is 96Å . Not surprisingly, the above polarization value is small as compared to the value (-0.25 C/m^2) in perfect $BaTiO_3$, since the *local* polarizations in a large number of bulk cells cancel in Fig.1.6(b), except those bulk cells far away from the vacancy plane.

Our calculations also answer another important question, namely the length of the polarization dead layer to be caused by the oxygen-vacancy plane. We see from Fig.1.6(a) [with assistance from Fig.1.6(b)] that the length of dead layer is approximately 9 cells (or 36Å) on each side of the oxygen-vacancy plane. The (total) length of polarization dead layer is thus 72Å and is rather large, indicating that planar oxygen vacancies are indeed very harmful to electric polarization.

IV. Conclusions

Various physical properties of planar oxygen vacancies in ferroelectric $BaTiO_3$ are investigated by density functional theory and modern theory of polarization. The considered properties include the energetics of vacancy formation, conditions to grow (or eliminate) the planar V_O^q vacancies, insulating or conducting nature of different vacancy-charge states, the magnitude of electric polarization when vacancies are presented, as well as the microscopic structure insight. The main findings of our studies are summarized in the following.

(i) Under the oxygen-poor condition, planar V_O^q vacancies can spontaneously form and thus abundantly exist in $BaTiO_3$ [Fig.1.2(a)]. Interestingly, we also find that, even under the oxygen-rich condition, the formation energy of planar V_O^{2+} vacancies is small and merely 0.54 eV when μ_e is near VBM [Fig.1.2(c)], and planar V_O^{2+} vacancies are thus also very likely to occur.

Furthermore, by varying the chemical potential μ_e of electron reservoir, each of the three charge states of oxygen vacancies can be made most stable. Quantitatively, according to our calculations in Fig.1.2(c), V_O^{2+}, V_O^{1+}, and V_O^0 are most stable in the regions $\mu_e < 1.22$ eV, $1.22 < \mu_e < 2.22$ eV, and $\mu_e > 2.22$ eV, respectively.

(ii) We determine the optimal condition to grow (or eliminate) the planar oxygen vacancies of all three charge states in $BaTiO_3$. If planar oxygen vacancies are beneficial and need be generated on purpose, the optimal condition (i.e., Condition G) is to choose μ_O around $\mu_O = -3.0$ eV while adjusting μ_e to be in the range from 1.6 to 2.4 eV [Fig.1.2(b)], since the formation energies of all three charge states are rather small and ~0.6 eV under the Condition G. Another advantage of choosing the Condition G is that, by altering μ_e, one can change the most-stable charge state of planar V_O^q vacancies, hence tuning the transport properties.

On the other hand, if planar oxygen vacancies are detrimental and need be eliminated, our calculations show that the optimal condition (i.e., Condition E) to eliminate them is to grow $BaTiO_3$ under the oxygen-rich condition ($\mu_O = 0$ eV) while adjusting μ_e to be near CBM [Fig.1.2(c)].

(iii) $BaTiO_3$ with planar V_O^{2+} vacancies is an insulator, and therefore no mobile charges are available to screen the polarization if ferroelectricity is to persist. The band gap of $BaTiO_3$ with V_O^{2+} vacancies is reduced as compared to perfect $BaTiO_3$. In contrast, $BaTiO_3$ with planar oxygen vacancies of two other charge states (i.e., V_O^{1+} or V_O^0) are found to be metallic, and ferroelectricity will be screened or at least partially screened by mobile charges.

(iv) Pursuing one step further, we quantitatively calculate the electric polarization of defected $BaTiO_3$ with planar V_O^{2+} vacancies, and we find that planar V_O^{2+} vacancies almost completely eliminate the polarization when the spacing *S* between two adjacent V_O^{2+} planes is 24Å , showing that planar oxygen vacancies have a devastating effect on ferroelectricity. Our calculations also provide a rather strong evidence that polarization fatigue is likely caused by extended defects rather than isolated defects.

(v) By examining the relative displacement ΔZ of Ti and O atoms, we find that, for planar V_O^q vacancies of all three charge states, ΔZ in cell 1 (i.e., in the bulk cell near the vacancy) is much enhanced by ~300% than in perfect $BaTiO_3$ [Fig.1.5]. The ΔZ enhancement in cell 1 mainly originates from the broken Ti-O bond when vacancies are created. Furthermore, ΔZ in cell 1 declines when charge state q changes from +2 to 0, which can be explained by the decreasing Coulomb interaction. Moreover, when the spacing S is 24Å , ΔZ is found to exhibit a mirror symmetry for all three charge states, namely ΔZs in cells ±1 are equal and have opposite sign, leading to the fact that polarization is largely eliminated by the planar vacancies.

(vi) When the spacing S is increased to 96Å , we find that ferroelectricity emerges, as demonstrated by the local Ti-O displacements in the region far away from the vacancy plane [Fig.1.6(b)]. The total length of polarization dead layer caused by planar V_O^{2+} vacancies is shown to be around 72Å .

Considering that extended vacancies profoundly alter the ferroelectric properties and may have important (technological) implications on polarization fatigue and imprinting, we thus hope this study will stimulate more theoretical and experimental interest in the extended vacancies in ferroelectrics.

V. Acknowledgments

This work was supported by the Office of Naval Research. The computing facility was provided by the High-Performance Computing Center at the University of Arkansas.

References

[1] M. E. Lines and A. M. Glass, *Principles and applications of ferroelectrics and related materials* (Clarendon Press, Oxford, 1977).

[2] R. E. Cohen, Nature **358**, 136–138, 1992.

[3] R. E. Cohen and H. Krakauer, Phys. Rev. B **42**, 6416-6423 (1990).

[4] M. Fornari and D. J. Singh, Phys. Rev. B **63**, 092101 (2001).

[5] J. López-Pérez and J. Íñiguez, Phys. Rev. B 84, 075121 (2011).

[6] S. Pöykkö and D. J. Chadi, Phys. Rev. Lett. **83**, 1231-1234 (1999).

[7] A. Kimmel, P. Weaver, M. Cain and P. Sushko, Phys. Rev. Lett. **109**, 117601 (2012).

[8] A. Chandrasekaran, D. Damjanovic, N. Setter and N. Marzari, Phys. Rev. B **88**, 214116 (2013).

[9] C. Paillard, G. Geneste, L. Bellaiche and B. Dkhil, J. Phys.: Condens. Matter **29**, 485707 (2017).

[10] Z. Alahmed and H. Fu, Phys. Rev. B **76**, 224101 (2007).

[11] Y. Yao and H. Fu, Phys. Rev. B **84**, 064112 (2011).

[12] M. Choi, F. Oba and I. Tanaka, Appl. Phys. Lett. **98**, 172901 (2011).

[13] P. Erhart and K. Albe, J. Appl. Phys. **102**, 084111 (2007).

[14] M. Dawber, K. M. Rabe and J. F. Scott, Rev. Mod. Phys. **77**, 1083-1130 (2005).

[15] J. F. Scott and M. Dawber, Appl. Phys. Lett. **76**, 3801 (2000).

[16] J. F. Scott, Science **315**, 954-959 (2007).

[17] J. F. Scott, *Ferroelectric memories* (Springer, Berlin, 2000).

[18] K. Uchino, *Piezoelectric actuators and ultrasonic motors* (Kluwer Academic, Boston, 1996).

[19] W. Zhong, R. D. King-Smith and D. Vanderbilt, Phys. Rev. Lett. **72**, 3618-3621 (1994).

[20] M.-H. Du and D. J. Singh, Phys. Rev. B **81**, 144114 (2010).

[21] S.-E. Park and T. Shrout, J. Appl. Phys. **82**, 1804 (1997).

[22] A. Garcia and D. Vanderbilt, Appl. Phys. Lett. **72**, 2981 (1998).

[23] H. Fu and R. Cohen, Nature **403**, 281-283 (2000).

[24] B. Noheda, D. Cox, G. Shirane, J. Gonzalo, L. Cross and S.-E. Park, Appl. Phys. Lett. **74**, 2059 (1999).

[25] B. Noheda, D. E. Cox, G. Shirane, S.-E. Park, L. E. Cross and Z. Zhong, Phys. Rev. Lett. **86**, 3891-3894 (2001).

[26] X. Fu, I. Naumov and H. Fu, Nano. Lett. **13**, 491-496 (2012).

[27] J. Íñiguez and L. Bellaiche, Phys. Rev. Lett. **87**, 095503 (2001).

[28] A. George, J. Iniguez and L. Bellaiche, Nature **413**, 54–57 (2001).

[29] I. I. Naumov, L. Bellaiche and H. Fu, Nature **432**, 737-740 (2004).

[30] I. Naumov and H. Fu, Phys. Rev. Lett. **98**, 077603 (2007).

[31] M. Pereira Goncalves, C. Escorihuela-Sayalero, P. Garca-Fernandez, J. Junquera and J. Iniguez, Sci. Adv. **5**, eaau7023 (2019).

[32] H. M. Duiker, P. D. Beale, J. F. Scott, C. Paz de Araujo, B. M. Melnick, J. D. Cuchiaro and L. D. McMillan, J. Appl. Phys. **68**, 5783 (1990).

[33] X. Du and I. Chen, J. Appl. Phys. **83**, 7789 (1998).

[34] M. Dawber and J. Scott, Appl. Phys. Lett. **76**, 1060 (2000).

[35] A. Tagantsev, I. Stolichnov, E. Colla and N. Setter, J. Appl. Phys. **90**, 1387 (2001).

[36] Z. Fan, C. Zhou, X. Ren and X. Tan, Appl. Phys. Lett. **111**, 252902 (2017).

[37] L. V. D. He, Phys. Rev. B **68**, 134103 (2003).

[38] O.N. Tufte and P.W. Chapman, Phys. Rev. **155**, 796 (1967).

[39] E. Cockayne and B. P. Burton, Phys. Rev. B **69**, 144116 (2004).

[40] L. Bellaiche, J. Iniguez, E. Cockayne, and B.P. Burton, Phys. Rev. B **75**, 014111 (2007).

[41] X. Ren, Nat. Mater. **3**, 91 (2004).

[42] S.-H. Wei and S. B. Zhang, Phys. Rev. B **66**, 155211 (2002).

[43] C. Freysoldt, B. Grabowski, T. Hickel, J. Neugebauer, G. Kresse, A. Janotti, and C.G. Van de Walle, Rev. Mod. Phys. **86**, 253 (2014), and references therein.

[44] P. Hohenberg and W. Kohn, Phys. Rev. 136, **B864** (1964); W. Kohn and L.J. Sham, Phys. Rev. **140**, A1133 (1965).

[45] P. Giannozzi, S. B. N. Baroni and *et al*., J. Phys. C **21**, 395502 (2009)

[46] N. Troullier and J. L. Martins, Phys. Rev. B **43**, 1993-2006 (1991).

[47] H. Fu and O. Gulseren, Phys. Rev. B **66**, 214114 (2002).

[48] R. Wahl, D. Vogtenhuber, and G. Kresse, Phys. Rev. B **78**, 104116 (2008).

[49] M. El-Batanouny and F. Wooten, *Symmetry and Condensed Matter Physics* (Cambridge University Press, Cambridge, 2008).

[50] H.J. Monkhorst and J.D. Pack, Phys. Rev. B **13**, 5188 (1976).

[51] R. D. King-Smith and D. Vanderbilt, Phys. Rev. B **47**, 1651 (1993).

[52] R. Resta, Rev. Mod. Phys. **66**, 889 (1994).

[53] Y. Yao and H. Fu, Phys. Rev. B **79**, 014103 (2009).

[54] A. Raeliarijaona and H. Fu, Sci. Rep. **7**, 41301 (2017); Phys. Rev. B **96**, 144431 (2017).

[55] D. Lowndes, D. Geohegan, A. Puretzky, D. Norton and C. Rouleau, Science **273**, 898-903 (1996).

[56] D. Schlom and *et al.*, Mater. Sci. Eng. B **87**, 282-291 (2001).

[57] D. Muller, N. Nakagawa, A. Ohtomo, J. Grazul and H. Hwang, Nature **430**, 657–661, (2004).

[58] R. Klie, Y. Ito, S. Stemmer and N. Browning, Ultramicroscopy **86**, 289-302 (2001).

[59] J. Heyd, G.E. Scuseria, and M. Ernzerhof, J. Chem. Phys. **118**, 8207 (2003).

[60] W.J. Yin, J.H. Yang, J. Kang, Y. Yan, and S.-H. Wei, J. Mater. Chem. A **3**, 8926 (2015).

[61] S. Chen, A. Walsh, X.G. Gong, S.-H. Wei, Adv. Mater. **25**, 1522 (2013).

[62] W. Merz, Phys. Rev. **91**, 513-517 (1953).

[63] B. Jaffe, W.R. Cook, and H. Jaffe, *Piezoelectric Ceramic* (Academic Press, London, 2012).

[64] C. Mitra, C. Lin, J. Robertson, and A.A. Demkov, Phys. Rev. B **86**, 155105 (2012).

[65] M. Veithen and Ph. Ghosez, Phys. Rev. B **65**, 214302 (2002).

[66] H. Fu and L. Bellaiche, Phys. Rev. Lett. **91**, 057601 (2003).

Chapter 2: Possible existence of unusual tri-stable polarization states in $LiNbO_3$ under an open-circuit boundary condition

I. Introduction

Hyperferroelectricity (HyFE), in which an out-of-plane polarization persists in proper ferroelectrics (FE) under an open-circuit boundary condition (OCBC) [1-3], is an intriguing phenomenon of fundamental and technological importance. Unlike improper hybrid FEs in which the structural instability is caused by the rotational soft modes at the zone boundary [4-6], the dominating structural instability in proper FEs is caused by the soft phonon at the zone center. When ferroelectricity is present in proper FEs under OCBC, the out-of-plane polarization often generates a strong depolarization field, which tends to eliminate entirely the polarization [7, 8]. Ferroelectricity is thus not anticipated to persist in proper FEs under OCBC, which explains why HyFE is interesting and fundamentally important [9]. Furthermore, certain HyFE materials may also exhibit other favorable properties such as negative longitudinal piezoelectric coefficients [10]. HyFE was previously reported to exist in hexagonal ABC-type semiconducting FEs (such as LiBeSe and LiZnAs) [1] and in compounds $LiBO_3$ (where B can be V, Nb, Ta, and Os) [3].

Technologically, lack of ferroelectricity under OCBC limits the miniaturization of FE devices and impairs the applications of FE materials [11]. On the other hand, provided that HyFE exists under OCBC, the storage density of FE memories can be increased [12, 13], and the efficiency of switching polarization may be improved due to the reduction in coercive field. Furthermore, by heterostructuring HyFEs with other functional solids such as semiconductors and/or superconductors, the properties of the combined systems may be effectively tuned by utilizing the polarization in HyFEs.

While the mechanism of HyFE remains unsettled, one possible origin is attributed to the small Born effective charge of ions and small longitudinal-optic/transverse-optic splitting [1]. However, Li *et al.* pointed out that this may not be necessary; for instance, HyFE was reported to exist in $LiBO_3$-type materials in which the Born effective charges of ions are large [3]. Other possible explanations include deep internal-energy well and small spontaneous polarization [2], the significance of short-range interaction [3, 14], or the existence of metascreening [15].

Despite the importance of HyFE, many issues of fundamental relevance nevertheless remain not fully understood. (i) First, it is profoundly important to seek reliable methods that can accurately determine whether a solid is HyFE. Currently, one key approach is to use the existence of soft longitudinal-optic (LO) phonon with imaginary frequency as the standard criterion [1-3]. This approach is widely used, and the existence of a soft LO phonon is commonly thought as the hallmark of HyFE. Recently this approach was employed to predict that $LiBO_3$ is HyFE [3]. Nevertheless, one critical question remains unanswered: is this hallmark of HyFE fully justified? Is it possible that a solid possessing soft LO phonon may turn out to be *not* a HyFE? (ii) It remains fundamentally interesting and meanwhile elusive to understand why the strong depolarization field does not eliminate the polarization in HyFE and what physical origin leads to its nonzero polarization under OCBC. Discovery of this origin may vastly expand our understanding of HyFE. (iii) In the search for new HyFEs, we often rely on the trial-and-error approach, which is time-consuming and less efficient. In light of this, one may wonder whether there exists any pivotal physical quantity that is of unique importance in terms of providing the much-needed guide in the designing and searching for new HyFEs. (iv) Are there any interesting and previously-unknown phenomena, which wait to be discovered in HyFEs?

The purpose of this project is to address the above subjects of fundamental relevance. Instead of using the existence of soft LO phonon as the criterion of determining HyFE [3], we here use a different (and more rigorous) approach by determining the electric free energy under OCBC. The approach of electric free energy is powerful and generally applicable because, provided that a solid is HyFE, it should by definition exhibit a nonzero polarization at the minimum of free energy when the solid is under OCBC. We choose to consider $LiNbO_3$ since this material is technologically important by possessing strong ferroelectricity and piezoelectricity, high electro-optic coefficient, and photoelastic effect [16]. In fact, $LiNbO_3$ has been widely used in optical parametric oscillators, beam deflectors, memory elements, electro-optic and nonlinear optical devices [16]. The $LiNbO_3$ solid belongs to the R3c space group in FE phase and the $R\bar{3}c$ space group in PE phase. The PE-to-FE phase transition occurs at 1480 K.

Driven by the technological interest, various properties of $LiNbO_3$ have been studied previously. For example, neutron scattering shows evidence that the phase transition in $LiNbO_3$ is largely order-disorder type [17]. The fundamental band gap of $LiNbO_3$ was calculated using GW approach and Bethe-Salpeter equation, along with the phonon frequencies in FE and PE $LiNbO_3$ [18]. In particular, the frequencies of the soft A_{2u} and A_{2g} modes were found to be 183*i* and 92*i* cm^{-1}, respectively [18]. Raman scattering efficiency were calculated and assigned to the measured Raman peaks [19], and the theory confirms the experimental results [20]. By using the vibration free energy, the FE-to-PE Curie temperature was theoretically determined [21]. Furthermore, localized vibration modes were found to exist both at the positive and negative surfaces of $LiNbO_3$ [22].

Besides addressing the key issues on HyFE as described above, we will further answer some critical questions regarding $LiNbO_3$. These questions include (1) whether $LiNbO_3$ is HyFE under

OCBC? (2) How deep is the HyFE potential well, if HyFE exists in $LiNbO_3$? (3) How large is the hyperferroelectric polarization when $LiNbO_3$ is under OCBC? These questions cannot be (and have not been) rigorously addressed in previous study, which uses the approach of predicting HyFE according to the existence of soft LO phonon [3].

We find that (i) the longitudinal $A_{2u}(LO_1)$ soft mode at imaginary frequency $96i$ cm^{-1} in $LiNbO_3$ yields, under OCBC, a nonzero polarization of magnitude $P = 0.023$ C/m^2. The physical origin responsible for the existence of this nonzero polarization, despite that the system is under OCBC, is found to stem from the remarkably small depolarization energy caused by the $A_{2u}(LO_1)$ phonon, which is about *three orders of magnitude* smaller than the depolarization energy caused by the corresponding transverse-optic (TO) phonon. (ii) However, and interestingly, we discover that the *ground state* of $LiNbO_3$ under OCBC is nevertheless *not* hyperferroelectric, which differs from previous study where $LiNbO_3$ was concluded to be HyFE [3]. Instead we find that the ground state of $LiNbO_3$ under OCBC is nonpolar. This important finding reveals that possessing a soft LO mode does not guarantee that the solid is HyFE. Therefore, one must be cautious when using the hallmark criterion of determining HyFE according to the soft LO mode. (iii) The reason that the ground state of $LiNbO_3$ is not HyFE can be attributed to the fact that there is a strong nonpolar mode, being soft at frequency $120i$ cm^{-1} under OCBC, and this mode drives the system to be nonpolar. (iv) Moreover, we reveal another intriguing phenomenon, namely that $LiNbO_3$ under OCBC may possess an unusual, triple potential well. In other words, $LiNbO_3$ under OCBC exhibits three stable and/or metastable states with different polarizations.

II. Theoretical Methods

A combination of three different methods is used to investigate the hyperferroelectric properties in $LiNbO_3$. (i) We use the first-principles linear response theory [23-26] to determine

the phonon eigenvalues and eigenvectors, paying particular attention to the TO and LO phonons. The appearance of soft TO phonon gives rise to structural instability under the short-circuit boundary condition (SCBC). Meanwhile, the existence of soft LO phonon indicates the possibility of structural instability under OCBC, since an LO phonon is obtained after the corresponding (one or multiple) TO phonons interact with the macroscopic electric field induced by lattice vibration [27-29]. (ii) To determine the magnitude of electric polarization in the system, we use the modern theory of polarization via the geometric Berry-phase approach [30, 31]. (iii) We determine whether a solid is HyFE by optimizing the electric free energy under OCBC [32]. When a solid under OCBC exhibits a nonzero polarization at the free-energy minimum, HyFE occurs. These methods are described in the following.

A. Linear-response phonon calculations

Phonon calculations are performed using the density functional perturbation theory (DFPT) [23–26]. Change in bare-ions potential ΔV due to atomic vibration is treated as perturbation, and the response of electron state $|\Delta\psi_n\rangle$ is obtained by solving the Sternheimer equation [23],

$$(H_{scf} - \varepsilon_n)|\Delta\psi_n\rangle = -(\Delta V_{scf} - \Delta\varepsilon_n)|\psi_n\rangle, \quad (1)$$

where H_{scf} is the single-pproject Kohn-Sham Hamiltonian, ε_n is the eigenvalue of H_{scf}, $\Delta V_{scf}(\boldsymbol{r}) = \Delta V(\boldsymbol{r}) + e\int \frac{\Delta\rho(\boldsymbol{r}')}{|\boldsymbol{r}-\boldsymbol{r}'|} d\boldsymbol{r}' + \frac{dv_{xc}(\rho)}{d\rho}\Big|_{\rho=\rho(\boldsymbol{r})} \Delta\rho(\boldsymbol{r})$ is the first-order correction to the self-consistent Vsc f (r) potential, and $\Delta\varepsilon_n = \langle\psi_n|\Delta V_{scf}(\boldsymbol{r})|\psi_n\rangle$ is the first-order correction to eigenvalue ε_n. Born effective-charge tensor (Z) and high-frequency dielectric tensor (ϵ_∞) are also determined within the DFPT calculations.

Phonon frequencies and eigenvectors are obtained by solving the secular equation $det\left|\frac{1}{\sqrt{M_i M_j}} C_{i\alpha,j\beta}(\vec{q}) - \omega^2(\vec{q})\right| = 0$, where $C(\vec{q})$ is the force-constant matrix, ω is frequency, i and

j are atomic indices, and α and β are the Cartesiandirection indices [33]. $C(\vec{q})$ includes both analytic C^a and nonanalytic C^{na} contributions [25]. The analytic part C^a is the force-constant matrix computed directly from DFPT under zero macroscopic electric field. The nonanalytic part C^{na} is caused by the fact that, in the long-wavelength limit $q \to 0$, an LO phonon leads to a macroscopic electric field, which is to interact with the lattice vibration. The nonanalytic term is given as where $C^{na}_{i\alpha,j\beta}(\vec{q}) = \frac{4\pi}{\Omega} e^2 \frac{(\vec{q}\cdot Z_i)_\alpha (\vec{q}\cdot Z_j)_\beta}{\vec{q}\cdot\epsilon_\infty\vec{q}}$, where Z_i is the Born effective-charge tensor of atom i and ϵ_∞ is the high-frequency dielectric tensor due to the electron response [25].

It should be pointed out that, when C^{na} is not included in the dynamic matrix, there is no macroscopic electric field in the solid (which corresponds to the electrical boundary condition of SCBC), and the existence of soft modes (if any) thus indicates the structure instability under SCBC [26]. On the other hand, when C^{na} is included in the dynamic matrix, the macroscopic electric field is nonzero (which corresponds to the electrical boundary condition of OCBC), and the existence of soft modes indicates the structure instability under OCBC.

B. Polarization calculations

Electric polarization consists of ionic and electronic contributions. Ionic contribution can be calculated directly using point charges as $\mathbf{P}_{ion} = \frac{1}{\Omega}\sum_i q_i \boldsymbol{r}_i$, where q_i is the charge of ion i and $\boldsymbol{r}_i$ is the ion position. Electronic contribution is calculated using the modern theory of polarization via the Berry-phase approach [30, 31],

$$\mathbf{P}_{\text{el}} = \frac{2e}{(2\pi)^3}\int d\mathbf{k}_\perp \,\text{Im ln}\prod_j \det\,(< u_{m,\mathbf{k}_\parallel^j} | u_{n,\mathbf{k}_\parallel^{j+1}} >), \qquad (2)$$

where $u_{n,\mathbf{k}}$ is the cell-periodic Bloch part of occupied wave functions, $\mathbf{k}_\perp$ and $\mathbf{k}_\parallel$ are, respectively, the components of the electron wave vector perpendicular and parallel to the polarization direction.

Microscopic understanding of $\mathbf{P}_{\mathrm{el}}$ from individual $\mathbf{k}_{\perp}$ string can be further analyzed using the theory of polarization structure [34].

C. Electric free energy under OCBC

When a FE solid is under OCBC (i.e., with a vanishing electric displacement D = 0), a macroscopic electric field E is to appear, which will interact with polarization and polarize the electron wave functions. To make our theory generally applicable, we consider an arbitrary atomic configuration $\{\mathbf{r}_i(\lambda)\}$ parametrized by λ. Here, $\{\mathbf{r}_i(\lambda)\}$ can be an intermediate configuration between the centrosymmetric configuration $\{\mathbf{r}_i^{\mathrm{c}}\}$ of the paraelectric (PE) phase and the ferroelectric configuration $\{\mathbf{r}_i^{\mathrm{f}}\}$ of the FE phase, according to $\mathbf{r}_i = \mathbf{r}_i^{\mathrm{c}} + \lambda(\mathbf{r}_i^{\mathrm{f}} - \mathbf{r}_i^{\mathrm{c}})$, where i is the atomic index and λ is the control parameter by which we vary the atomic configuration. Alternatively, the configuration $\{\mathbf{r}_i(\lambda)\}$ can be obtained by shifting the atoms in the PE phase according to the eigendisplacement $|\vec{u}_i\rangle$ of a given phonon mode as

$$\mathbf{r}_i(\lambda) = \mathbf{r}_i^{\mathrm{c}} + \lambda a_0 \vec{u}_i, \tag{3}$$

where a_0 is the lattice constant. For configuration λ, the electric free energy under OCBC is [35]

$$F(\lambda) = U(\lambda) - \Omega(\lambda)\left[P(\lambda)\cdot E + \frac{1}{2}\epsilon_0 \chi_\infty(\lambda) E^2\right], \tag{4}$$

which $U(\lambda)$, $\Omega(\lambda)$, and $P(\lambda)$ are, respectively, the internal energy, unit-cell volume, electric polarization, and the χ_∞^{33} component of high-frequency dielectric permittivity at configuration λ; all these quantities are computed from the DFT calculations at zero macroscopic electric field because Eq.(4) is essentially a second-order Taylor expansion of the free energy around the zero field [32]. Since we are interested in the circumstances where the electric field is along the direction of polarization, the vector notations are thus dropped in Eq.(4). For a given E field, the

total electric polarization is obtained from Eq.(4) as $P_{tot} = -\frac{1}{\Omega}\frac{\partial F}{\partial E} = P(\lambda) + \epsilon_0\chi_\infty(\lambda)E$. Under OCBC where D vanishes, the macroscopic E field is thus

$$E = -\frac{P(\lambda)}{\epsilon_0[1+\chi_\infty(\lambda)]}. \quad (5)$$

Combining Eq.(4) and Eq.(5), the free energy of arbitrary configuration λ under OCBC is [32]

$$F(\lambda) = U(\lambda) - \Omega(\lambda)\frac{1+\frac{1}{2}\chi_\infty(\lambda)}{\epsilon_0[1+\chi_\infty(\lambda)]^2}P^2(\lambda), \quad (6)$$

where all quantities on the right-hand side can be computed by DFT. The second term in Eq.(6) is clearly the energy cost introduced by the depolarization field under OCBC, and will be denoted as

$$U_{dp} = \Omega(\lambda)\frac{1+\frac{1}{2}\chi_\infty(\lambda)}{\epsilon_0[1+\chi_\infty(\lambda)]^2}P^2(\lambda). \quad (7)$$

If the free energy under OCBC exhibits a global minimum at a configuration with nonzero polarization, the solid is then a HyFE.

D. Computational details

Technically we use the density functional theory (DFT) within the local density approximation (LDA) to calculate the total (internal) energy and atomic forces, and to optimize the structure. Computations are performed using QUANTUM ESPRESSO [36, 37]. Troullier-Martins type of norm-conserving pseudopotentials is generated to replace the effects of core electrons [38]. The rhombohedral unit cell of $LiNbO_3$ with ten atoms is used. The cutoff energy for planewave expansion of the single-pproject wavefunctions is 110 Ry, which is sufficient.

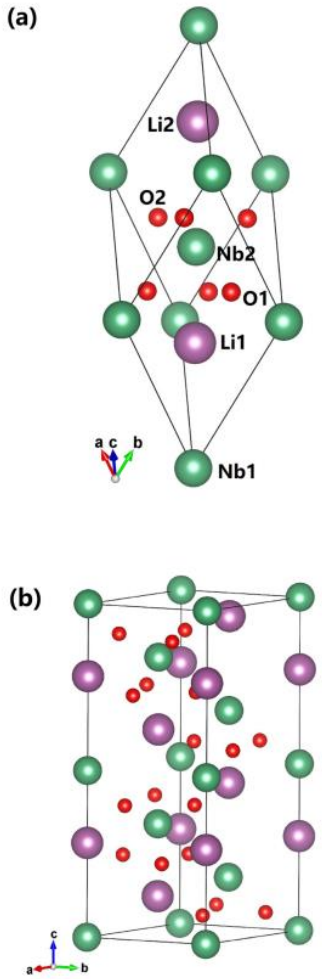

FIG. 2. 1: Crystal structure of $LiNbO_3$: (a) 10-atom rhombohedral unit cell, (b) 30-atom hexagonal unit cell. Li, Nb, and O atoms are shown in purple, green, and red spheres, respectively.

The $LiNbO_3$ crystal can be described either using a 10-atoms rhombohedral unit cell with lattice constant a_R and angle γ between two trigonal lattice vectors [Fig.2.1(a)], or using a 30-atoms hexagonal unit cell with in-plane lattice constant a_H and out-of-plane lattice constant c [Fig.2.1(b)]. The relationship between the lattice parameters of these two cells is: $a_R = \frac{1}{3}\sqrt{3a_H^2 + c^2}$ and $\sin\frac{\gamma}{2} = \frac{3/2}{\sqrt{3+c^2/a_H^2}}$. For the FE phase of bulk $LiNbO_3$ under SCBC, our structural optimization yields a_R = 5.444 Å and γ = 55.813°, which are close to experimental results a_R = 5.494 Å and γ = 55.867° [39]. The electric polarization in FE $LiNbO_3$ is calculated to be 0.768

C/m^2, agreeing with the experimental value of 0.71 C/m^2 [40]. The depth of the FE double potential wells is determined to be −258 meV, close to the value of −259 meV in another study [41].

To examine the hyperferroelectric properties, we also need to consider the PE phase since HyFE occurs often near the PE phase. For PE $LiNbO_3$ with centrosymmetry, atoms are located at Li ($\frac{1}{4}$, $\frac{1}{4}$, $\frac{1}{4}$), Nb (0, 0, 0), and O ($u, \frac{1}{2}-u, \frac{3}{4}$) in the coordinate frame of the rhombohedral lattice vectors. We optimize both the cell parameters and internal parameter u while constraining the R$\bar{3}$c symmetry, and we obtain a_R = 5.394 Å, γ = 56.7°, and u = 0.1275. Converting our theoretical results from the rhombohedral cell to the hexagonal cell, we find a_H = 5.1228 Å, c = 13.5326 Å, and an O-atom position (0.0441, $\frac{1}{3}, \frac{1}{12}$) . These values agree well with a_H = 5.1378 Å, c = 13.4987 Å, and the O atom position (0.0490, $\frac{1}{3}, \frac{1}{12}$) in Ref. [42], and with a_H = 5.1250 Å, c = 13.5480 Å, and the O atom position (0.0420, $\frac{1}{3}, \frac{1}{12}$) in Ref. [43]. In PE $LiNbO_3$, our calculated Z^*_{33} effective charges are 1.11, 9.03, and -3.36, respectively, for Li, Nb, and O atoms, which are close to the values of 1.11, 9.17, and -3.43 in another calculation [43]. All results show that our calculations are rather reliable.

III. Results and discussions

A. LO phonon in $LiNbO_3$

Since HyFE is closely connected with LO phonon, we begin by presenting the LO phonon in PE *$LiNbO_3$*. Table.2.1 lists the calculated phonon frequencies for several zone-center modes of key importance in PE $LiNbO_3$, obtained from the linear response calculations. Note that we report in

Table.2.1 the phonon frequencies, calculated both with and without the nonanalytical C^{na} contribution in the dynamic matrix.

TABLE. 2. 1: The zone-center phonon modes of key relevance (2nd column), frequency ω (3rd column), and mode-specific effective charge $\tilde{Z}_3^{n\vec{q}}$ (4th column) in centrosymmetric $LiNbO_3$. Results calculated without (and with) non-analytic C^{na} contribution in dynamic matrix are given in the upper (and lower) part of the Table. The nonsoft $A_{2u}(TO_2)$ mode is also listed since it participates in forming the $A_{2u}(LO_1)$ mode.

C^{na} or not	Modes	ω (cm^{-1})	$\tilde{Z}_3^{n\vec{q}}$
without C^{na}	$A_{2u}(TO_1)$	$202i$	6.65
	A_{2g}	$113i$	0.00
	$A_{2u}(TO_2)$	95	−4.21
with C^{na}	A_{2g}	$120i$	0.00
	$A_{2u}(LO_1)$	$96i$	0.39

Table.2.1 I reveals that (i) when C^{na} is not included (i.e., under SCBC), there are two soft modes, one is the $A_{2u}(TO_1)$ mode at frequency $\omega = 202i$ cm^{-1} and the other is the nonpolar A_{2g} mode at $\omega = 113i$ cm^{-1} (see the upper part of Table.2.1) [44]; (ii) When C^{na} is included (i.e., when macroscopic electric field is nonzero), the A_{2g} mode remains to be soft, and its frequency barely changes from $113i$ cm^{-1} to $120i$ cm^{-1} (see the lower part of Table.2.1). This is not surprising since the A_{2g} mode is nonpolar and thus does not interact strongly with the macroscopic electric field. (iii) Interestingly, besides nonpolar A_{2g}, another *polar* mode remains soft after C^{na} is included, that is, the longitudinal-optic $A_{2u}(LO_1)$ mode. Furthermore, the frequency of $A_{2u}(LO_1)$ is rather strongly imaginary at $\omega = 96i$ cm^{-1}, suggesting that this mode is to cause a significant structure instability under OCBC.

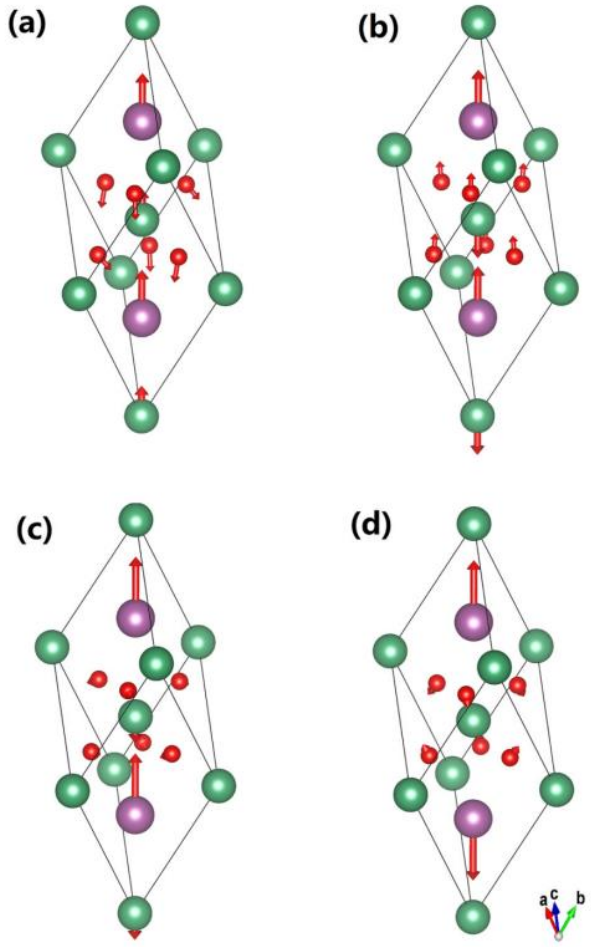

FIG. 2. 2: Phonon eigenvectors for the following modes: (a) $A_{2u}(TO_1)$, (b) $A_{2u}(TO_2)$, (c) $A_{2u}(LO_1)$, (d) non-polar A_{2g}. Li, Nb, and O atoms are shown in purple, green, and red spheres as in Fig.2.1(a), respectively.

To provide microscopic insight into the structure instability, we show in Fig.2.2 the phonon eigenvectors of those modes in Table.2.1. For $A_{2u}(TO_1)$ in Fig.2.2(a), we see that positively charged Li and Nb ions move along the same direction, and negatively-charged O ions move in an opposite direction along the polar axis, showing that $A_{2u}(TO_1)$ is a polar mode. For $A_{2u}(TO_2)$, which is not soft, Fig.2.2(b) tells that, while Nb and O atoms move along opposite directions, Li and O atoms nevertheless move along the same direction. The soft LO phonon of $A_{2u}(LO_1)$ in Fig.2.2(c) is more intriguing—this mode consists predominantly of the displacements of Li atoms,

with small but not negligible contributions from Nb and O atoms. The A_{2g} mode in Fig.2.2(d) reveals that two Li atoms move along opposite directions with the same magnitude (which maintains the centrosymmetry), and therefore this mode is indeed nonpolar.

Since soft LO phonon plays a pivotal role in developing HyFE, we go one step further and attempt to find out where $A_{2u}(LO_1)$ originates from, by performing the following mode analysis [29]. Let us use the ket vector $|\omega_i\rangle$ to denote the phonon eigenvectors obtained from the dynamic matrix without the nonanalytic C^{na} contribution, and use $|\omega'_i\rangle$ to denote the eigenvectors obtained from the dynamic matrix with the C^{na} contribution. We recognize that the eigenvectors $|\omega_i\rangle$ at the $\vec{q}$ = 0 zone center form a complete basis set for this phonon wave vector. We can thus use $|\omega_i\rangle$ as bases and expand $|\omega'_i\rangle$ according to $|\omega'_i\rangle = \sum_i t_{ij}|\omega'_i\rangle$, where coefficients $t_{ij} = \langle\omega_i|\omega'_j\rangle$ should tell us quantitatively which modes participate in forming a given $|\omega'_i\rangle$ mode. We find that $|A_{2u}(LO_1)\rangle = \sqrt{0.39}|A_{2u}(LO_1)\rangle + \sqrt{0.61}|A_{2u}(TO_2)\rangle$. It reveals two important outcomes: (i) $A_{2u}(LO_1)$ and $A_{2u}(TO_1)$ do not have the same eigenvectors, and instead $A_{2u}(TO_1)$ contributes only 39% in the process of forming $A_{2u}(LO_1)$. This is in marked difference with semiconductor ZnO where LO and TO modes have nearly identical eigenvectors although their frequencies differ [32]. (ii) $A_{2u}(LO_1)$ mainly comes from the nonsoft $A_{2u}(TO_2)$, which suggests a critical knowledge that nonsoft phonon may play an important role in forming HyFE.

B. Can soft $A_{2u}(LO_1)$ yield HyFE?

After finding that $A_{2u}(LO_1)$ is soft, it then becomes interesting to investigate (i) how strong a (HyFE) spontaneous polarization may be induced by this longitudinal mode, and (ii) how deep the HyFE potential well will be under OCBC. These questions are nontrivial particularly when system is under OCBC, and the answers are previously unknown. For this purpose, we calculate the

electric free energies along the configuration path as parameterized in Eq.(3) by using the vibration eigendisplacement $|\vec{u}_i\rangle$ of $A_{2u}(LO_1)$.

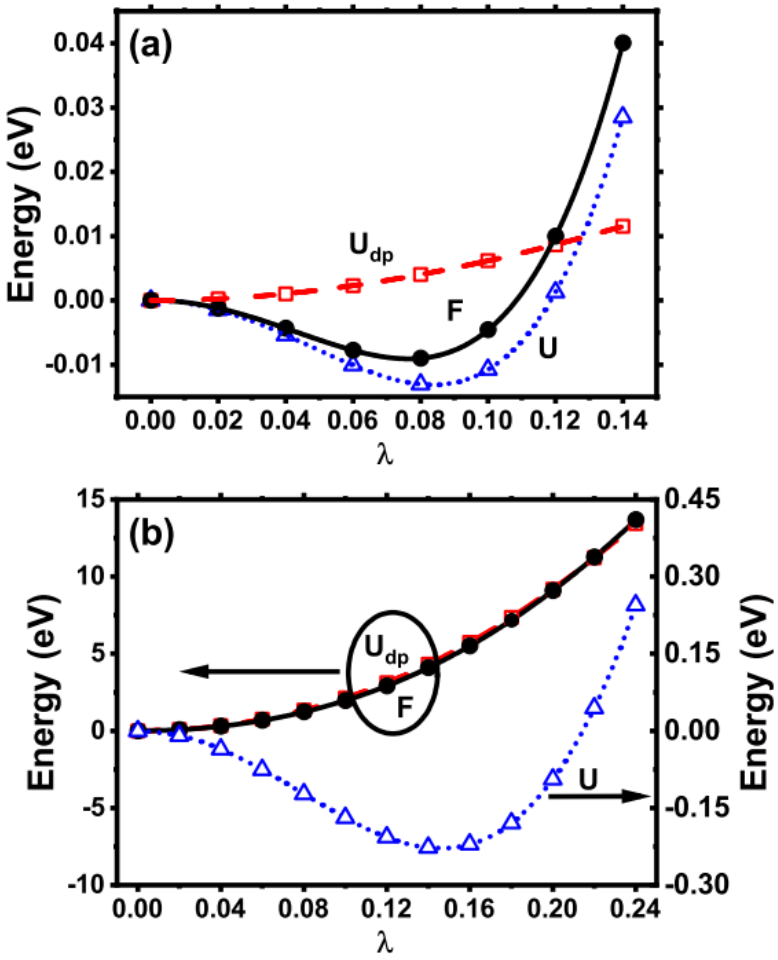

FIG. 2. 3. Electric free energy $F(\lambda)$ (solid dots), internal energy $U(\lambda)$ (empty triangles), and depolarization energy $U_{dp}(\lambda)$ (empty squares) in $LiNbO_3$ under OCBC as a function of λ, for the following phonon modes: (a) soft longitudinal $A_{2u}(LO_1)$ mode, and (b) soft transverse $A_{2u}(TO_1)$ mode. In (b), $F(\lambda)$ and $U_{dp}(\lambda)$ are plotted using the left vertical axis, while $U(\lambda)$ is plotted using the right vertical axis so that the depth of the potential well of $U(\lambda)$ can be clearly displayed. $\lambda = 0$ corresponds to the PE phase. $F(\lambda)$ exhibits a minimum at $\lambda = 0.0765$ for $A_{2u}(LO_1)$ mode in (a). $U(\lambda)$ exhibits a minimum at $\lambda = 0.1460$ for $A_{2u}(TO_1)$ mode in (b).

The calculated free energy $F(\lambda)$, along with the internal energy $U(\lambda)$, is shown in Fig.2.3(a) for $LiNbO_3$ under OCBC. Fig.2.3(a) reveals that, as λ deviates from the PE phase of λ=0, free energy $F(\lambda)$ starts to decrease, showing that, under OCBC, the PE phase is unstable against the phonon

displacement of the $A_{2u}(LO_1)$ mode. In other words, we find that the soft $A_{2u}(LO_1)$ mode can induce, under OCBC, hyperferroelectricity at nonzero λ. Furthermore, our calculations in Fig.2.3(a) predict that $F(\lambda)$ reaches its minimum at λ=0.0765. We denote the structure phase with a nonzero polarization at λ=0.0765 as the LO-induced HyFE phase.

We further calculate the polarization of the LO-induced HyFE phase using the modern theory of polarization, and find that the polarization is P_{LO}=0.023 C/m^2. This polarization is not small and is comparable in magnitude to the value of 0.02 C/m^2 previously found in the ABC-type hyperferroelectric materials LiBeSb and LiZnAs [1]. Furthermore, Fig.2.3(a) shows that the free-energy depth of the HyFE potential well is ΔF=-9 meV, which is close to the internal-energy depth (-9.57 meV) of the double potential well in prototypical ferroelectric $BaTiO_3$ under SCBC [45]. This is rather remarkable and implies that the Curie temperature of HyFE in $LiNbO_3$ under OCBC could be as high as that of bulk $BaTiO_3$ (120˚C).

Having seen that $A_{2u}(LO_1)$ is able to induce a HyFE phase, readers may wonder whether $A_{2u}(TO_1)$, the TO mode, can produce a nonzero polarization under OCBC. Here we go one step further and determine the free energy $F(\lambda)$ under OCBC and the internal energy $U(\lambda)$ for this TO mode using the $A_{2u}(TO_1)$ eigendisplacement. The results are shown in Fig.2.3(b).

Let us first focus on the internal energy $U(\lambda)$ in Fig.2.3(b). Note in Eq.(4) that, when macroscopic electric field E vanishes (i.e., when system is under SCBC), the internal energy $U(\lambda)$ is the free energy, namely $U(\lambda)$ yields the energetics and structural instability under SCBC. Fig.2.3(b) reveals that (i) as λ deviates from λ=0, $U(\lambda)$ drastically decreases and exhibits a minimum at λ=0.1460. We name the atomic configuration corresponding to this λ value as the TO-induced phase (under SCBC). (ii) The potential well of $U(\lambda)$ for this TO-induced phase is very deep and is -227 meV [see the triangle symbols and the right vertical axis in Fig.2.3(b)]. (iii) We

further find that the $A_{2u}(TO_1)$ mode is the mode responsible for the FE phase in bulk $LiNbO_3$ under SCBC (not OCBC). As a matter of fact, we compute the polarization for the TO-induced phase, and find that the polarization is 0.756 C/m^2, which is very close to the calculated polarization value of 0.768 C/m^2 in bulk $LiNbO_3$ under SCBC. Furthermore, we examine the atomic off-center displacement Δr_z along the polar *z*-direction in the TO-induced phase with respect to the centrosymmetric configuration, by fixing one Nb atom at the origin as the reference. Δr_z is defined as $\Delta r_z(i) = r_z(i) - r_z^c(i)$, where $r_z(i)$ and $r_z^c(i)$ are the *z*-position of atom i in the non-centrosymmetric and centrosymmetric phases, respectively. Δr_z is shown in Fig.2.4, and we find that the Δr_z values for the TO-induced phase (yellow bars in Fig.2.4) and for the bulk FE phase (shaded bars in Fig.2.4) are very close to each other for all atoms, confirming that the $A_{2u}(TO_1)$ mode is indeed responsible for the ferroelectricity in bulk $LiNbO_3$ under SCBC.

Interestingly, Fig.2.3(b) also reveals that, although $U(\lambda)$ produces a deep internal-energy potential well, the free energy $F(\lambda)$ nevertheless does not exhibit a minimum at nonzero λ under OCBC. Instead, as λ deviates from λ=0 in Fig.2.3(b), $F(\lambda)$ monotonously increases. Therefore, under OCBC, $A_{2u}(TO_1)$ produces only a stable PE phase at λ=0. This demonstrates that the $A_{2u}(TO_1)$ mode cannot generate HyFE under OCBC.

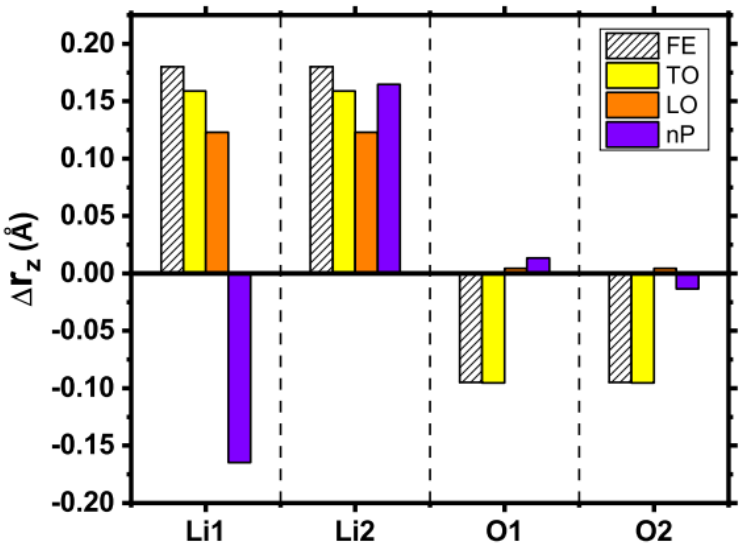

FIG. 2. 4: Atomic off-center displacement Δr_z with respect to the centrosymmetric PE phase, for the following configurations in $LiNbO_3$: the bulk FE phase under SCBC (shaded), the TO-induced phase under SCBC (yellow), the LO-induced phase under OCBC (orange), and the nonpolar nP phase under OCBC (violet). In all cases, one Nb atom is placed at the origin as the reference. Li1 and O1 are located at the bottom of the cell, while Li2 and O2 are located at the top of the cell [see Fig.2.1(a)].

C. Origin of LO-induced HyFE in $LiNbO_3$

The finding that the $A_{2u}(LO_1)$ mode is able to generate a free-energy minimum at nonzero λ (and thus produce HyFE) under OCBC, despite the fact that the internal-energy well of this soft LO mode is very shallow, is intriguing. We now attempt to provide the physical origin which aims at understanding why the HyFE free-energy minimum exists.

Figures 3.5(a)-3.5(d) shows the computed internal energy U, electric polarization P, high-frequency dielectric constant $\varepsilon_\infty = 1 + \chi_\infty$, and the depolarization energy U_{dp} for the $A_{2u}(LO_1)$ mode. In order to obtain insightful knowledge, we also plot in Fig.2.5 each quantity obtained for $A_{2u}(TO_1)$ (the TO mode) on the same figure so that a direct comparison can be made. Fig.2.5(a) reveals that the well depth of the internal energy for $A_{2u}(TO_1)$, -227 meV, is indeed much deeper than the value of -13 meV for $A_{2u}(LO_1)$; the latter is barely noticeable in the inset of Fig.2.5(a).

Interestingly, Fig.2.5(b) reveals that the electric polarizations for the configurations along the $A_{2u}(LO_1)$ path and along the $A_{2u}(TO_1)$ path exhibit drastic differences. Along the $A_{2u}(TO_1)$ path, polarization rises rapidly from P=0 at λ=0 to P=0.730 C/m^2 at λ=0.14 (which is near the internal-energy minimum of this TO mode). However, along the $A_{2u}(LO_1)$ path, polarization increases very slowly from P=0 at λ=0 to merely P=0.025 C/m^2 at λ=0.08 (which is near the internal-energy minimum of this LO mode). Quantitatively, the slope $\frac{dP}{d\lambda}$=0.31 C/m^2 along the LO path is more than *one order of magnitude smaller* than the slope $\frac{dP}{d\lambda}$=5.21 C/m^2 along the TO path, which is phenomenal.

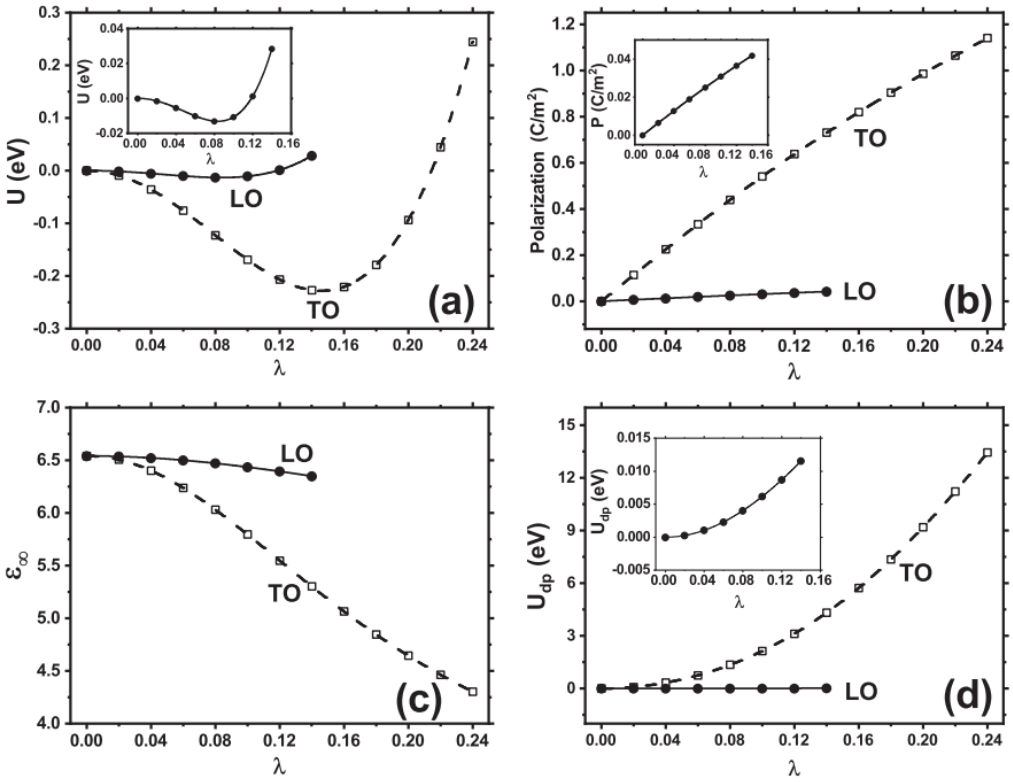

FIG. 2. 5: Variations of the following quantities as a function of λ, for the $A_{2u}(LO_1)$ mode (solid circles and labelled as LO) and for the $A_{2u}(TO_1)$ mode (open squares and labelled as TO): (a) internal energy $U(\lambda)$, (b) polarization $P(\lambda)$, (c) high-frequency dielectric constant $\varepsilon_\infty = 1 + \chi_\infty$, and (d) the depolarization energy U_{dp}. The insets in (a)-(d) are the blowup of the $A_{2u}(LO_1)$ curve on small scale.

We find that the key mechanism---by which $A_{2u}(LO_1)$ is able to generate a free-energy minimum at nonzero λ (and thus HyFE)---originates from the small depolarization energy U_{dp}, as depicted in Fig.2.5(d). From the inset of Fig.2.5(d), we see that, at λ=0.08 which is near the internal-energy minimum along the $A_{2u}(LO_1)$ path, the depolarization energy U_{dp} is only 4 meV, which is remarkably small. Since U is -13 meV at λ=0.08, the free energy $F=U+U_{dp}$ is still *negative* at this nonzero λ as shown in Fig.2.3(a), allowing the existence of structure instability (and thus HyFE) for $A_{2u}(LO_1)$ under OCBC. In contrast, along the $A_{2u}(TO_1)$ path, at λ=0.14 near the internal-energy minimum of this path, the depolarization energy in Fig.2.5(d) is 4.32 eV, far exceeding the internal-energy gain of -0.227 eV. As a consequence, the free energy in Fig.2.3(b) is positive when λ deviates from 0, and no structural instability occurs under OCBC along the $A_{2u}(TO_1)$ path.

It is not surprising that the depolarization energy U_{dp} is small along the $A_{2u}(LO_1)$ path, since U_{dp} is proportional to P^2 and inversely proportional to $\varepsilon_\infty = 1 + \chi_\infty$ according to Eq.(7). Our finding that the polarization increases slowly along the $A_{2u}(LO_1)$ path [Fig.2.5(b)] naturally leads to a small depolarization energy. The relatively larger ε_∞ dielectric constant along the $A_{2u}(LO_1)$ path [Fig.2.5(c)], as compared to that along the $A_{2u}(TO_1)$ path, further contributes to the small depolarization energy of $A_{2u}(LO_1)$.

D. Possible key quantity in the search for new HyFE

Another interesting and technologically-important question centers on whether there is any key physical quantity which may help in the searching or designing of new hyperferroelectric solids. We find that such a quantity indeed exists, and it is the mode-specific effective charge (MEC), $\tilde{Z}_\alpha^{n\vec{q}}$, of a given phonon (not the effective charges of ions). Consider a phonon mode $n\vec{q}$ with normalized eigendisplacement $u_{i\beta}^{n\vec{q}}$, the mode-specific effective charge $\tilde{Z}_\alpha^{n\vec{q}}$ of this phonon is defined as

$$\tilde{Z}_{\alpha}^{n\vec{q}} = \sum_{i\beta} Z_{i,\alpha\beta}^{*} \, u_{i\beta}^{n\vec{q}}, \tag{8}$$

where $Z_{i,\alpha\beta}^{*}$ is the dynamic Born effective charge of atom *i*, *n* the phonon-branch index, $\vec{q}$ the phonon wave vector, and α and β the indices of Cartesian directions. Note that (i) $\tilde{Z}_{\alpha}^{n\vec{q}}$ is a vector (not a tensor); (ii) $\tilde{Z}_{\alpha}^{n\vec{q}}$ depends critically on phonon displacement $u_{i\beta}^{n\vec{q}}$. Using the definition in Eq.(8), the change in polarization for the atomic configuration constructed along the vibration direction of the $n\vec{q}$ phonon will be $\Delta P_{\alpha} = \frac{1}{\Omega}\tilde{Z}_{\alpha}^{n\vec{q}} a_0 \Delta\lambda$, where a_0 is the lattice constant. Note that ΔP_{α} is directly proportional to the mode-specific effective charge $\tilde{Z}_{\alpha}^{n\vec{q}}$, not the Born effective charges Z^{*} of ions per se.

We compute the MEC along the polarization direction, namely $\tilde{Z}_3$, for the $A_{2u}(TO_1)$ and $A_{2u}(LO_1)$ modes, and the results are given in the fourth column of Table.2.1. The $\tilde{Z}_3$ value of $A_{2u}(TO_1)$ is found to be 6.65, which is large and leads to the rapid increase of polarization in Fig.2.5(b) for this TO mode as λ increases. Interestingly, and in sharp contrast, the $\tilde{Z}_3$ value of $A_{2u}(LO_1)$ is only 0.39, which is outstandingly small. This tiny MEC is critical in terms of giving rise to the very slow increase in the polarization when λ increases, as shown in Fig.2.5(b) for the LO mode. Therefore, we find that MEC is likely a possible key quantity that is responsible for the small polarization, small depolarization energy U_{dp}, and the existence of HyFE. Meanwhile, we would also like to point out that, although our study of $LiNbO_3$ suggests that small mode-specific effective charge is vitally important for the existence of HyFE, it nevertheless requires more studies on other hyperferroelectric solids to find out whether the conclusion can be generalized to other materials.

We recognize that $\tilde{Z}_3$=0.39 of $A_{2u}(LO_1)$ is even smaller than Z_{33}^{*}=1.11 of Li atom. This is rather interesting and meanwhile puzzling since (i) if $A_{2u}(LO_1)$ involves only Li atoms alone, its $\tilde{Z}_3$ value

will be 1.11, which is still considerably larger than 0.39; (ii) Z_{33}^{*}=9.03 of Nb atoms and Z_{33}^{*}=-3.36 of O atoms are (much) larger in magnitude than that of Li. The origin of the exceptionally small $\tilde{Z}_3$ of $A_{2u}(LO_1)$ can be intuitively understood by examining the phonon eigenvector of this mode in Fig.2.2(c). Fig.2.2(c) shows that, although $A_{2u}(LO_1)$ consists of a large amplitude from Li atoms, the contribution from Nb atoms cannot be neglected, however. Furthermore, note that Nb atoms vibrate along the *opposite* direction as Li atoms, and since Z_{33}^{*} of Nb is very large, a small vibration amplitude of Nb atoms will cancel, to a large extent, the contribution from Li atoms in Eq.(8), which leads to a small $\tilde{Z}_3$ for $A_{2u}(LO_1)$.

E. Existence of tri-stable states

The existence of soft LO mode has been previously used as a key benchmark for determining whether or not a solid is HyFE [1-3, 14]. Is this benchmark always valid? Is it possible that the ground state may turn out to be non-HyFE even if a soft LO mode exists under OCBC? Since this is a subject of critical importance, we address it here.

As we report in the lower part of Table.2.1, besides the soft $A_{2u}(LO_1)$ mode, there exists another soft A_{2g} mode when C^{na} is included (i.e., under OCBC). Fig.2.2(d) shows that, in A_{2g} mode, two Li atoms exhibit opposite displacements along the polar axis with respect to the central Nb atom; therefore, the mode is non-polar. Also note that under OCBC, the frequency of the A_{2g} mode, $120i$ cm^{-1}, is more unstable than the soft $A_{2u}(LO_1)$ mode. It will be inappropriate to ignore the soft non-polar A_{2g} mode and conclude $LiNbO_3$ is a bistable HyFE. One key question is to determine how the soft A_{2g} mode may affect HyFE in $LiNbO_3$ under OCBC.

We calculate the electric free energies for the configurations generated according to the phonon eigen-displacement of the A_{2g} mode, and the result is shown in Fig.2.6(a). Since the A_{2g} mode is non-polar, the depolarization energy U_{dp} is zero and the internal energy is the only contribution to

the free energy under OCBC. Fig.2.6(a) reveals that, when the free energy is at its minimum, the optimal λ value is 0.11. We name the configuration at this optimal λ as the non-polar "nP" phase, and denote the configuration as $\{\mathbf{r}_i^{\mathrm{nP}}\}$. Fig.2.6(a) also tells us that the free-energy well depth of the nP phase is -30.2 meV, which is about 3 times deeper than the counterpart of the $A_{2u}(LO_1)$-induced LO phase [see Fig.2.3(a)]. Therefore, our calculations reveal that the ground state of $LiNbO_3$ under OCBC is non-polar, which is energetically more stable than the hyperferroelectric LO phase under OCBC. Importantly, the result also demonstrates that the existence of soft LO mode does not guarantee the occurrence of HyFE. One must be cautious when using the existence of soft LO mode as the hallmark criterion to determine whether a solid is HyFE.

It is interesting to point out that $LiNbO_3$ behaves rather differently from the hexagonal ABC-type semiconductor FEs such as LiBeSb and LiZnAs. Unlike the ABC-type semiconductor FEs in which only one soft LO phonon exists in the long-wavelength limit under OCBC [1], $LiNbO_3$ under OCBC exhibits a soft, non-polar A_{2g} mode in addition to a soft LO mode. Previous study focused only on the soft LO mode in $LiNbO_3$ and did not consider the non-polar A_{2g} mode, which inappropriately concluded that $LiNbO_3$ is HyFE [3].

After having established that the ground state of $LiNbO_3$ under OCBC is non-polar, we further discover another intriguing possibility, that is, $LiNbO_3$ under OCBC exhibits unusual tri-stable states. To show this, we consider the configurations along the path connecting the nP phase and the LO phase, namely we examine the intermediate configurations according to $\mathbf{r}_i(\alpha) = \mathbf{r}_i^{\mathrm{nP}} + \alpha(\mathbf{r}_i^{\mathrm{LO}} - \mathbf{r}_i^{\mathrm{nP}})$, where $\mathbf{r}_i^{\mathrm{nP}}$ and $\mathbf{r}_i^{\mathrm{LO}}$ are respectively the atomic positions of the nP and LO phases. Obviously, α=0 and α=1 correspond to the nP phase and LO phase, respectively. The calculated free energy is plotted in Fig.2.6(b) as a function of parameter α. We set the local maximum of the free energy between the nP and LO phases as the zero energy in Fig.2.6(b).

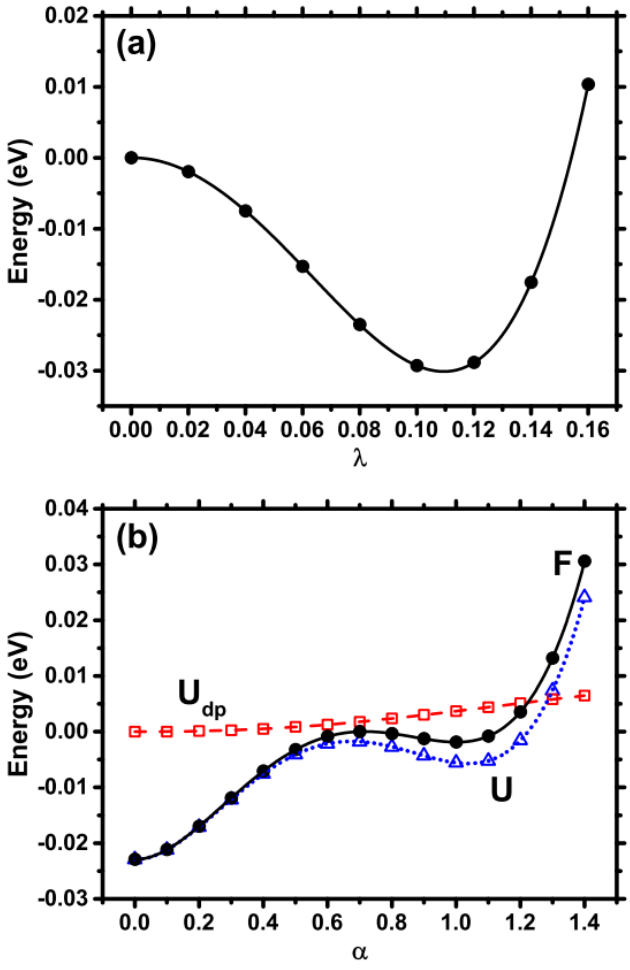

FIG. 2. 6: Electric free energy F of $LiNbO_3$ under OCBC for (a) the configurations generated according to the eigen-displacement of the soft A_{2g} mode, and (b) the configurations along the transition path from the non-polar nP phase to the LO phase, where the internal energy U and the depolarization energy U_{dp} are also shown. In (a), internal energy is the only contribution to the free energy, and the depth of the potential well is -30.2 meV. In (b), free energy F exhibits three local minima located at α=0 and α=±1.

Interestingly, Fig.2.6(b) reveals that, in addition to the global minimum at α=0, there is one local free-energy minimum located at α=1 (also at α=-1 due to symmetry), which is the hyperferroelectric LO phase with polarization P=0.023 C/m^2. We also find that, with respect to the local maximum at α=0.7, the well depth of the free energy for the LO and nP phases are -1.9 meV and -23 meV, respectively. Therefore, we find that $LiNbO_3$ under OCBC possesses interesting tri-stable states (i.e., three local minima at α=0 and α=±1).

The finding—that $LiNbO_3$ transforms from polarization bi-stable states to tri-stable states when the boundary condition changes from SCBC to OCBC—is interesting in the following sense: (i) unlike bistable states where the centrosymmetric state is unstable and cannot be accessed below the Curie temperature, the centrosymmetric nP phase in $LiNbO_3$ under OCBC is stable and can be accessed in experiments. (ii) As an unusual feature of the tri-stable states, the hysteresis loop in $LiNbO_3$ under OCBC will be different from the normal hysteresis of bi-stable states, by exhibiting the existence of a threshold electric field which is required to move the system out of the stable centrosymmetric nP phase. This may also reduce the dielectric loss during the hysteresis [46]. (iii) The existence of tri-stable states can be technologically very useful by utilizing HyFE to design new FE applications such as ternary memory devices and on/off switching devices.

IV. Conclusions

We have employed a combination of linear-response perturbation theory, the modern theory of polarization, and electric free energy to investigate the hyperferroelectric properties of technologically important $LiNbO_3$ solid under OCBC. Our specific findings are summarized in the following.

(i) The longitudinal $A_{2u}(LO_1)$ mode is soft with an imaginary frequency of $96i$ cm^{-1} in centrosymmetric $LiNbO_3$ under OCBC. Although the well depth of the *internal* energy is shallow and merely -13 meV for the $A_{2u}(LO_1)$ mode, we find that this LO mode can nevertheless induce a free-energy minimum at non-zero polarization P=0.023 C/m^2 (thus HyFE) under OCBC. The (HyFE) free-energy well depth is determined to be -9 meV, which is comparable to the well depth of bulk $BaTiO_3$ under SCBC.

In contrast, the transverse $A_{2u}(TO_1)$ mode, despite that it generates a very deep internal-energy well depth of -227 meV, is found incapable of inducing HyFE under OCBC.

(ii) The origin why soft $A_{2u}(LO_1)$ is able to generate a non-zero polarization under OCBC is revealed, and is found to result from the extraordinarily small depolarization energy which is only +4 meV. Combined with the (albeit small) internal-energy well depth of -13 meV, the electric free energy still exhibits a minimum at non-zero polarization and thus HyFE under OCBC. $A_{2u}(TO_2)$

(iii) We further reveal that the soft $A_{2u}(LO_1)$ mode is formed by the coupling between the soft $A_{2u}(TO_1)$ mode and *non-soft* $A_{2u}(TO_2)$ mode, and a large majority contribution of 61% comes from the non-soft $A_{2u}(TO_2)$. Our study thus shows new knowledge that non-soft mode may play a pivotal role in developing HyFE.

(iv) We find a critical physical quantity that is important in the searching and designing of new HyFE materials, and the quantity is the mode-specific effective charge $\tilde{Z}_{\alpha}^{n\vec{q}}$ defined in Eq.(8). We further determine that $\tilde{Z}_{3}^{n\vec{q}}$ is very small and merely 0.39 for $A_{2u}(LO_1)$ in $LiNbO_3$, which is 1700% smaller than $\tilde{Z}_{3}^{n\vec{q}}$=6.65 for $A_{2u}(TO_1)$. In fact, $\tilde{Z}_{\alpha}^{n\vec{q}}$ can in principle approach zero for LO modes. A tiny $\tilde{Z}_{\alpha}^{n\vec{q}}$ gives rise to a very small depolarization energy U_{dp} and thus HyFE under OCBC.

(v) Despite that $A_{2u}(LO_1)$ can induce HyFE, we discover that the ground state of $LiNbO_3$ under OCBC is nevertheless not HyFE. The reason that the ground state of $LiNbO_3$ is not HyFE is caused by the fact that, in addition to soft $A_{2u}(LO_1)$, there exists another soft non-polar A_{2g} mode in $LiNbO_3$ under OCBC, which dominates the structure distortion and produces a non-polar ground state. Our calculations thus reveal that the existence of a soft LO mode does not guarantee that the solid will be HyFE. One need be cautious in using this criterion to determine HyFE.

(vi) We further reveal an intriguing possibility that $LiNbO_3$ is tri-stable under OCBC. More specifically, we find that, along the configuration path transitioning from the ground-state non-polar nP phase to the polar LO phase, $LiNbO_3$ under OCBC possesses three stable polarization states, which are located at P=±0.023 and 0 C/m^2. The free-energy potential wells for the nP and

LO phases are calculated to be -23 meV and -1.9 meV, respectively. The finding of tri-stable states in $LiNbO_3$ under OCBC may open new phenomena and new possibilities of technological applications. We hope the rich and interesting results in this study will stimulate more theoretical and experimental interest on hyperferroelectricity.

V. Acknowledgments

Computations were performed on the computing facilities provided by the Arkansas High-Performance Computing Center, supported by National Science Foundation.

References

[1] K. F. Garrity, K. M. Rabe, and D. Vanderbilt, Phys. Rev. Lett. **112**, 127601 (2014).

[2] H. Fu, J. Appl. Phys. **116**, 164104 (2014).

[3] P. Li, X. Ren, G.-C. Guo, and L. He, Sci. Rep. **6**, 34085 (2016).

[4] C. J. Fennie and K. M. Rabe, Phys. Rev. B **72**, 100103(R) (2005).

[5] E. Bousquet, M. Dawber, N. Stucki, C. Lichtensteiger, P. Hermet, S. Gariglio, J.-M. Triscone, and P. Ghosez, Nature (London) **452**, 732 (2008).

[6] N. A. Benedek and C. J. Fennie, Phys. Rev. Lett. **106**, 107204 (2011).

[7] M. Dawber, K. M. Rabe, and J. F. Scott, Rev. Mod. Phys. **77**, 1083 (2005).

[8] J. Junquera and P. Ghosez, Nature (London) **422**, 506 (2003).

[9] N. A. Benedek and M. Stengel, Physics **7**, 32 (2014).

[10] S. Liu and R. E. Cohen, Phys. Rev. Lett. **119**, 207601 (2017).

[11] M. E. Lines and A. M. Glass, Principles and Applications of Ferroelectrics and Related Materials (Clarendon Press, Oxford, 1977).

[12] J. F. Scott and C. A. Paz de Araujo, Science **246**, 1400 (1989).

[13] J. F. Scott, Ferroelectric Memories (Springer, Berlin, 2000).

[14] M. Khedidji, D. Amoroso, and H. Djani, Phys. Rev. B **103**, 014116 (2021).

[15] H. J. Zhao, A. Filippetti, C. Escorihuela-Sayalero, P. Delugas, E. Canadell, L. Bellaiche, V. Fiorentini, and J. Iniguez, Phys. Rev. B **97**, 054107 (2018).

[16] R. S. Weis and T. K. Gaylord, Appl. Phys. A **37**, 191 (1985).

[17] M. R. Chowdhury, G. E. Peckham, and D. H. Saunderson, J. Phys. C: Solid State Phys. **11**, 1671 (1978).

[18] W. G. Schmidt, M. Albrecht, S. Wippermann, S. Blankenburg, E. Rauls, F. Fuchs, C. Rodl, J. Furthmuller, and A. Hermann, Phys. Rev. B **77**, 035106 (2008).

[19] S. Sanna, S. Neufeld, M. Rusing, G. Berth, A. Zrenner, and W. G. Schmidt, Phys. Rev. B **91**, 224302 (2015).

[20] S. Margueron, A. Bartasyte, A. M. Glazer, E. Simon, J. Hlinka, I. Gregora, and J. Gleize, J. Appl. Phys. **111**, 104105 (2012).

[21] M. Friedrich, A. Schindlmayr, W. G. Schmidt, and S. Sanna, Phys. Status Solidi B **253**, 683 (2016).

[22] S. Sanna, G. Berth, W. Hahn, A. Widhalm, A. Zrenner, and W. G. Schmidt, Ferroelectrics **419**, 1 (2011).

[23] S. Baroni, S. Gironcoli, A. D. Corso, and P. Giannozzi, Rev. Mod. Phys. **73**, 515 (2001).

[24] S. Baroni, P. Giannozzi, and A. Testa, Phys. Rev. Lett. **58**, 1861 (1987).

[25] X. Gonze, Phys. Rev. A **52**, 1096 (1995).

[26] X. Gonze and C. Lee, Phys. Rev. B **55**, 10355 (1997).

[27] D. M. Eagles, J. Phys. Chem. Solids **25**, 1243 (1964).

[28] W. Zhong, R. D. King-Smith, and D. Vanderbilt, Phys. Rev. Lett. **72**, 3618 (1994).

[29] A. Raeliarijaona, and H. Fu, Phys. Rev. B **92**, 094303 (2015).

[30] R. D. King-Smith and D. Vanderbilt, Phys. Rev. B **47**, 1651 (1993).

[31] R. Resta, Rev. Mod. Phys. **66**, 899 (1994).

[32] R. Adhikari and H. Fu, Phys. Rev. B **99**, 104101 (2019).

[33] M. Born and K. Huang, *Dynamical Theory of Crystal Lattices* (Clarendon Press, Oxford, 1988).

[34] Y. Yao and H. Fu, Phys. Rev. B **79**, 014103 (2009).

[35] M. Stengel, N. A. Spaldin, and D. Vanderbilt, Nat. Phys. **5**, 304 (2009).

[36] P. Giannozzi, S. Baroni, N. Bonini, M. Calandra, R. Car, C. Cavazzoni, D. Ceresoli, G. L. Chiarotti, M. Cococcioni, I. Dabo *et al.* J. Phys.: Condens. Matter **21**, 395502 (2009).

[37] See, https://www.quantum-espresso.org.

[38] N. Troullier and J. L. Martins, Phys. Rev. B **43**, 1993 (1991).

[39] S. C. Abrahams, J. M. Reddy, and J. L. Bernstein, J. Chem. Phys. Solids **27**, 997 (1966).

[40] S. H. Wemple, M. DiDomenico Jr., and I. Camlibel, Appl. Phys. Lett. **12**, 209 (1968).

[41] M. Ye and D. Vanderbilt, Phys. Rev. B **93**, 134303 (2016).

[42] A. V. Postnikov, V. Caciuc, and G. Borstel, J. Phys. Chem. Solids **61**, 295 (2000).

[43] M. Veithen and P. Ghosez, Phys. Rev. B. **65**, 214302 (2002).

[44] Our calculated frequency 202*i* cm^{-1} for $A_{2u}(TO_1)$ agrees well with 201*i* cm^{-1} in Ref. [43] and with 183*i* cm^{-1} in Ref. [18].

[45] H. Fu and R. E. Cohen, Nature (London) **403**, 281 (2000).

[46] A. D. L. Chandani, T. Hagiwara, and Y. Suzuki, Jpn. J. Appl. Phys. **27**, L729 (1988).

Chapter 3: Giant hyperferroelectricity in LiZnSb and its origin

I. Introduction

Hyperferroelectricity (HyFE) is an interesting phenomenon of both fundamental and technological importance [1-3]. Differing from improper ferroelectrics (with the dominating structural instability occurring at the zone boundary) [4-7], materials with HyFE are a class of proper ferroelectrics (FE) in which ferroelectric instability originates from the soft phonons at the zone center. When proper FEs are under an open-circuit boundary condition (OCBC), the strong depolarization field tends to suppress ferroelectricity [8, 9]. Intriguingly, HyFEs are able to maintain polar instability even under OCBC (despite the existence of depolarization field), which explains why HyFEs are fundamentally interesting [10].

Technologically, HyFEs can be potentially very useful in device miniaturization; for instance, the persisting polarization in HyFE thin films allows the FE memories to be smaller, which increases the storage density [11, 12]. HyFEs may also possess unusual properties such as polarization tri-stability [13] and negative longitudinal piezoelectric coefficients [14]. Furthermore, HyFEs can be utilized (in heterostructures) to tune the properties of other functional materials such as topological insulators or superconductors.

HyFE has been reported to exist in hexagonal ABC-type semiconducting FEs such as LiBeSb [1], and in $LiBO_3$ compounds (where B can be V, Nb, Ta, and Os) [3]. Furthermore, HyFE was also shown to be metastable in $LiNbO_3$ under OCBC [13].

Despite the profound importance of HyFE, many fundamental challenges nevertheless remain in the field of HyFE. More specifically, (i) the spontaneous polarization under OCBC, found so far in many HyFEs, turns out to be tiny and not practically useful. For example, the HyFE polarization in LiBeSb is merely 0.02 C/m^2 under OCBC, which is more than twenty times smaller

than the value of 0.59 C/m^2 of the same solid under a short-circuit boundary condition (SCBC) [1]. Similarly, in $LiNbO_3$ under OCBC, the HyFE polarization was reported to be 0.023 C/m^2, which is drastically reduced from the polarization of 0.768 C/m^2 in $LiNbO_3$ under SCBC [13]. The tiny HyFE polarization under OCBC poses an outstanding obstacle to the technological use of hyperferroelectricity. It is thus fundamentally important to search for HyFE materials of large polarization under OCBC. (ii) The well depth of hyperferroelectricity is detrimentally small, and consequently, the HyFE phase is stable only at very low temperatures. For instance, the free-energy well depth of the HyFE phase in $LiNbO_3$ under OCBC is only -1.9 meV, which is two orders of magnitude smaller than the FE well depth of -227 meV under SCBC [13]. Thermal fluctuation can thus easily eliminate the hyperferroelectricity in $LiNbO_3$. Therefore, seeking the hyperferroelectricity that is stable under room temperature is of critical significance. (iii) HyFE defies the conventional wisdom, by possessing ferroelectricity despite the strong depolarization field. It is thus profoundly important to identify the origin on why HyFE exists—and even better, to discover the mechanism that can lead to strong HyFE with large polarization.

In this project, we investigate the hyperferroelectricity in LiZnSb using first-principles density functional theory. LiZnSb has been experimentally synthesized [15], and exhibits interesting properties such as superior thermoelectric conductivity[16]. We determine the HyFE polarization and well depth using a rigorous approach based on the electric free energy under OCBC [17]. When a solid possesses hyperferroelectricity, the electric free energy under OCBC should, by definition, exhibit a minimum at a structure configuration of nonzero polarization.

We find that (i) a giant HyFE polarization exists in LiZnSb under -2% compressive inplane strain, and the magnitude of polarization is 0.282 C/m^2 under an open-circuit boundary condition, which is rather remarkable since this magnitude of polarization under OCBC is comparable to the

polarization of 0.21 C/m^2 in prototypical ferroelectric $BaTiO_3$ under a short-circuit boundary condition [18]. (ii) The hyperferroelectricity in LiZnSb is discovered to be unusually stable, with a well depth of the electric free-energy being -332 meV. It indicates that the HyFE phase in LiZnSb is stable even under room temperature. (iii) The physical origin responsible for the giant hyperferroelectricity is shown to stem from two facts: the mode effective charge of the soft longitudinal-optic (LO) phonon is large in LiZnSb, and LiZnSb is close to be metallic with a large high-frequency dielectric constant. This finding also provides a useful guideline in order to search for new HyFE materials. (iv) Moreover, we reveal that hyperferroelectricity under OCBC responds to the inplane strain in an interestingly different manner than ferroelectricity under SCBC.

II. Theoretical methods

We employ the density functional theory (DFT) within the local density approximation (LDA) [19] to calculate the total (internal) energy, atomic force, cell stress, and the optimal structure, as implemented in Quantum Espresso [20, 21]. Norm-conserving pseudopotentials of the Troullier-Martins type is generated to replace the effects of core electrons [22, 23]. Spin-orbit coupling is included in the calculations. The cutoff energy for plane-wave expansion of the single-pproject wavefunctions is 120 Ry, which is tested to be sufficient. $6 \times 6 \times 4$ Monkhorst-Pack k-mesh is used. A combination of three different methods are used to investigate the HyFE properties in LiZnSb. These methods are described as follows.

(i) The linear-response density functional perturbation theory (DFPT) [24-27] is used to study the lattice vibration and phonon modes. Phonon frequencies and eigenvectors are calculated by solving the secular equation $det\left|\frac{1}{\sqrt{M_i M_j}} C_{i\alpha,j\beta}(\vec{q}) - \omega^2(\vec{q})\right| = 0$, where $C(\vec{q})$ is the force-constant matrix, ω is eigen-frequency, i and j are atomic indices, and α and β are the indices of Cartesian directions [28]. $C(\vec{q}) = C^a + C^{na}$ includes both the analytic part C^a and non-analytic part C^{na} [26].

The analytic part applies when there is no macroscopic electric field (i.e., when the system is under SCBC); C^{a} can be directly calculated using DFPT [25, 26]. The non-analytic part comes from the interaction between lattice vibration and the macroscopic electric field, e.g., when the system is under OCBC. C^{na} is computed [26] as $C^{na}_{i\alpha,j\beta}(\vec{q}) = \frac{4\pi}{\Omega} e^2 \frac{(\vec{q}\cdot Z_i)_\alpha (\vec{q}\cdot Z_j)_\beta}{\vec{q}\cdot\Sigma_\infty\vec{q}}$, where Z_i is the Born effective-charge tensor of atom i, and Σ_∞ is the high-frequency dielectric tensor due to the electronic response.

Since HyFE is related to soft modes and structural instability under OCBC [1-3], we begin with the paraelectric (PE) phase of LiZnSb, and optimize the atomic positions and cell structure while constraining it to be centro-symmetric. We then compute the zone-center phonon modes. The existence of a soft longitudinal-optic (LO) phonon in the PE phase indicates that the system is unstable under OCBC [1, 2]. Nevertheless, the existence of soft LO phonon does not guarantee that the system is HyFE [13].

(ii) The electric free-energy approach [17] is used to determine whether (or not) HyFE exists in a solid. Once a zone-center soft LO phonon is determined, we then vary the atomic configuration using the vibration eigen-displacement $|\vec{u}_i\rangle$ of this soft LO phonon, according to $\mathbf{r}_i(\lambda) = \mathbf{r}_i^{c} + \lambda c\vec{u}_i$, where $\{\mathbf{r}_i^{c}\}$ is the configuration of the PE phase, λ is the control parameter, and c is the lattice constant along the polarization direction.

The electric free-energy of a polar solid under a finite electric field E is defined [29] as $F(\lambda) = U(\lambda) - \Omega(\lambda)\left[P(\lambda)\cdot E + \frac{1}{2}\epsilon_0\chi_\infty(\lambda)E^2\right]$, which U is the internal energy, Ω the unit-cell volume, P the electric polarization, and $\chi_\infty = \Sigma_\infty^{33} - 1$ is the component of high-frequency dielectric permittivity. Here, both P and E are along the polar direction, and therefore the vector notation is dropped. Using the free energy, one obtains the total polarization under a finite electric field as

$P_{tot} = -\frac{1}{\Omega}\frac{\partial F}{\partial E} = P(\lambda) + \epsilon_0\chi_\infty(\lambda)E$. In this equation, the electronic contribution to the total polarization is included in the second term via high-frequency dielectric permittivity χ_∞. The ionic contribution is included in the first term (which is the Berry-phase polarization for *new* atomic positions after ions move). Therefore, the dielectric permittivity from ions is included in the free energy via polarization *P* and need not be accounted again. Using the vanishing electric displacement *D*=0 under OCBC, the electric free energy along the LO configuration path can be analytically determined as [17],

$$F(\lambda) = U(\lambda) - \Omega(\lambda)\frac{1+\frac{1}{2}\chi_\infty(\lambda)}{\epsilon_0[1+\chi_\infty(\lambda)]^2}P^2(\lambda), \quad (1)$$

The second term in Eq.(1) is the energy cost due to the existence of depolarization field, and will be denoted as the depolarization energy $U_{dp}(\lambda)$. By definition, a solid will be HyFE if the electric free-energy $F(\lambda)$ has a minimum at nonzero λ (i.e., at a configuration with nonzero polarization).

(iii) The electric polarization *P* in Eq.(1) is computed using the modern theory of polarization via the geometric Berry-phase approach [30, 31]. Microscopic understanding of electric polarization can be further obtained using the theory of polarization structure [32].

III. Results and discussions

A. Structural and electronic properties of LiZnSb

The centro-symmetric PE phase of LiZnSb has $P6_3/mmc$ symmetry, and its unit cell is shown in Fig.3.1(a), where Zn and Sb atoms are located on the same plane, and Li atoms occupy the intercalated positions. Polar LiZnSb (i.e., the FE phase) exhibits a LiGaGe structure with $P6_3mc$ group symmetry, where Zn and Sb atoms occupy the sites of the wurtzite sublattices. The unit cell of the FE phase of LiZnSb is shown in Fig.3.1(b). The atomic positions and spontaneous

polarization in FE LiZnSb were reported previously [33, 34], but hyperferroelectric properties were not investigated in these studies.

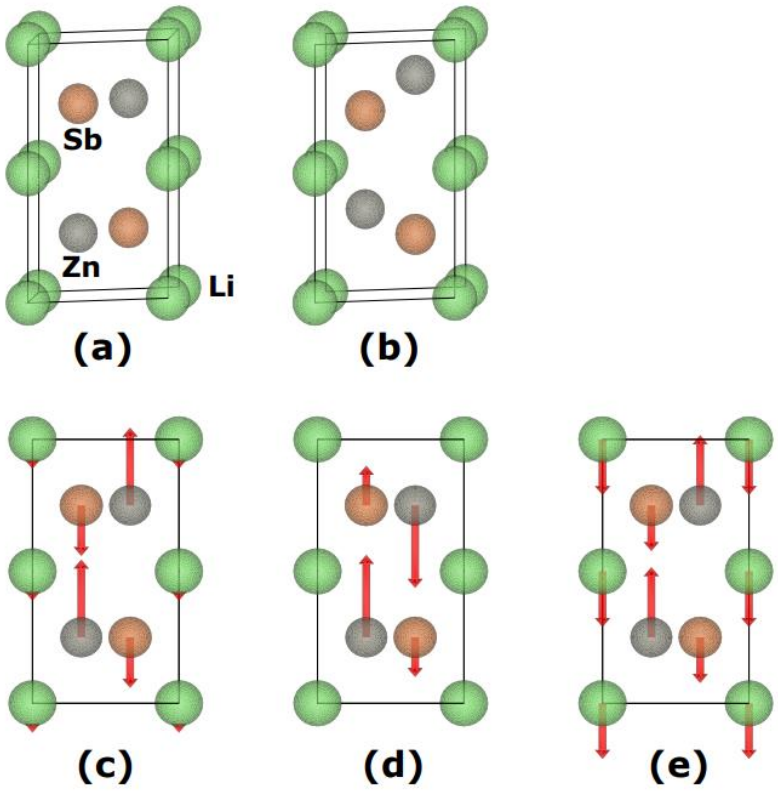

FIG. 3. 1: (a) A three-dimensional (3D) view of the unit cell of LiZnSb in the centrosymmetric PE phase; (b) A 3D view of the unit cell of LiZnSb in the FE phase. (c)-(e) The side views of the phonon eigenvectors of the following modes in PE LiZnSb under a −2% inplane strain: (c) soft transverse-optic $A_{2u}(TO_1)$ mode; (d) non-polar B_{1g} mode; (e) soft longitudinal-optic $A_{2u}(LO_1)$ mode. Atomic vibration amplitude and direction are shown in arrows. Li, Zn, and Sb atoms are shown respectively in green, gray, and golden colors.

The lattice constants obtained in our calculations are a=4.392 Å and c=7.490 Å for the PE phase of LiZnSb, where atoms are located at Li (0, 0, 0), Zn (2/3, 1/3, 1/4), and Sb (1/3, 2/3, 1/4). For the FE phase of LiZnSb, our calculated lattice constants are a=4.355 Å and c=7.073 Å, which agree well with the values a=4.376 Å and c=7.081 Å in Ref.[33], as well as with the results a=4.341 Å and c=6.962 Å in Ref.[34]. Atomic positions of FE LiZnSb are determined to be Li (0, 0, 0), Zn (2/3, 1/3, 0.342), and Sb (1/3, 2/3, 0.224) in our calculations, which are in good agreement with

other studies (see Table.3.1 for comparison). Furthermore, our calculated electric polarization for FE LiZnSb under SCBC is 0.544 C/m^2, and our calculated depth of the FE double well is -0.776 eV. These values are consistent with the electric polarization of 0.56 C/m^2 and FE well depth of -0.8 eV in another study [33]. All these results show that our calculations are rather reliable.

TABLE. 3. 1: The lattice constants and atomic positions in the FE phase of LiZnSb. Atomic positions are given in the framework of lattice vectors, where one Li atom is placed at the origin. The second column is our results, and the third column is the results obtained in other studies.

Quantity	Our work	Others
a (Å)	4.355	4.376[a], 4.341[b]
c (Å)	7.073	7.081[a], 6.962[b]
Zn	(2/3, 1/3, 0.342)	(2/3, 1/3, 0.331)[a], (2/3, 1/3, 0.335)[b]
Sb	(1/3, 2/3, 0.224)	(1/3, 2/3, 0.212)[a], (1/3, 2/3, 0.217)[b]

[a] [33], [b] [34]

Since hyperferroelectricity often occurs near the PE phase [1] and requires the knowledge of structural instability of soft LO phonon in the PE phase [13], we thus examine the PE LiZnSb in greater details. The calculated band structure of PE LiZnSb is shown in Fig.3.2(a). Interestingly we find that LiZnSb in the PE phase is metallic (or semimetal). Specifically, Fig.3.2(a) reveals that, near the zone-center Γ point, the top valence band and the bottom conduction band cross the Fermi energy [see the enlarged band structure in the bottom-right of Fig.3.2(a)], showing that the system is indeed metallic.

Strictly speaking, the metallic nature of PE LiZnSb does not allow us to investigate polarization and hyperferroelectricity, since the modern theory of polarization via the Berry's-phase approach requires that the system must remain to be insulating when it adiabatically moves along the path

between the PE phase and the FE phase [30, 31], in order for the electric polarization to be meaningfully defined. In metallic systems, the electric polarization, Born effective charges, and the LO/TO splitting are thus ill-defined [35, 36], which prevents the investigation of the LO phonon and hyperferroelectricity under OCBC.

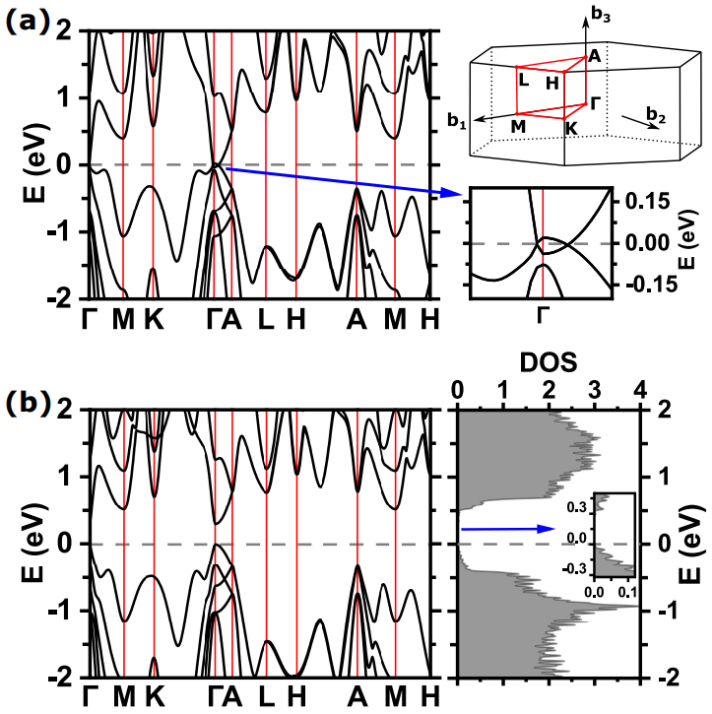

FIG. 3. 2: Band structures of centrosymmetric (PE) LiZnSb under the following inplane strains: (a) under zero inplane strain, and (b) under a compressive −2% inplane strain. In (a), the band structure of unstrained LiZnSb is shown in the left; the enlarged band structure close to the Fermi level near Γ point is given in the bottom of the right. The Brillouin zone and high-symmetry points are given in the top of the right. In (b), the band structure of LiZnSb under a −2% inplane strain is shown in the left; the density of states (DOS) is given in the right (with the DOS near the band gap being enlarged in the inset).

To drive the system out of the metallic state, we decide to apply the biaxial compressive inplane strain to LiZnSb. The band structure of PE LiZnSb under a -2% inplane strain is given in the left of Fig.3.2(b), showing that a direct band gap notably opens at Γ point. To further confirm that the system is insulating, we compute the density of states (DOS) across the full Brillouin zone (instead of the high-symmetry $\vec{k}$ paths as chosen in the band structure), and the obtained DOS is depicted

in the right of Fig.3.2(b). Our calculated DOS reveals that there is a sizable band gap of ~0.3 eV between the fully occupied valence states and the unoccupied conduction states, demonstrating that LiZnSb under a -2% inplane strain is indeed an insulator. Moreover, we also examine other magnitudes of compressive inplane strains, ranging from -1% to -6%. We find (see the Appendix for details) that the LiZnSb solids under the considered range of compressive strains are all insulators, with the band gap varying from 0.10 eV to 0.45 eV, which thus allows us to investigate the HyFE properties. In the following, we will largely focus on LiZnSb under the -2% inplane strain, unless specified otherwise.

B. Giant hyperferroelectricity in LiZnSb

Existence of soft LO phonon was previously demonstrated to be an important and necessary (although not sufficient) condition for the emergence of HyFE [13]. We thus first perform linear-response calculations and determine the soft modes in PE LiZnSb under a -2% inplane strain. When LiZnSb is under SCBC (i.e., there is no macroscopic electric field and the non-analytic C^{na} contribution to the force-constant matrix is not included), we find two soft modes in PE LiZnSb: one is the polar $A_{2u}TO_1$ mode at frequency $\omega = 107i$ cm^{-1}, and the other is the non-polar B_{1g} mode at frequency $\omega = 67.8i$ cm^{-1}. The phonon eigenvectors of these two modes are given in Fig.3.1(c) and Fig.3.1(d), respectively. We see that (i) for the $A_{2u}TO_1$ mode in Fig.3.1(c), Zn atoms move upward while Sb atoms move downward, and both types of atoms have large vibration amplitudes; this mode is thus polar. Meanwhile, the Li vibration contribution is rather small. (ii) For the B_{1g} mode in Fig.3.1(d), the displacements of two Zn atoms in the unit cell are opposite, so are the displacements of two Sb atoms. B_{1g} is thus non-polar with no contribution from Li atoms.

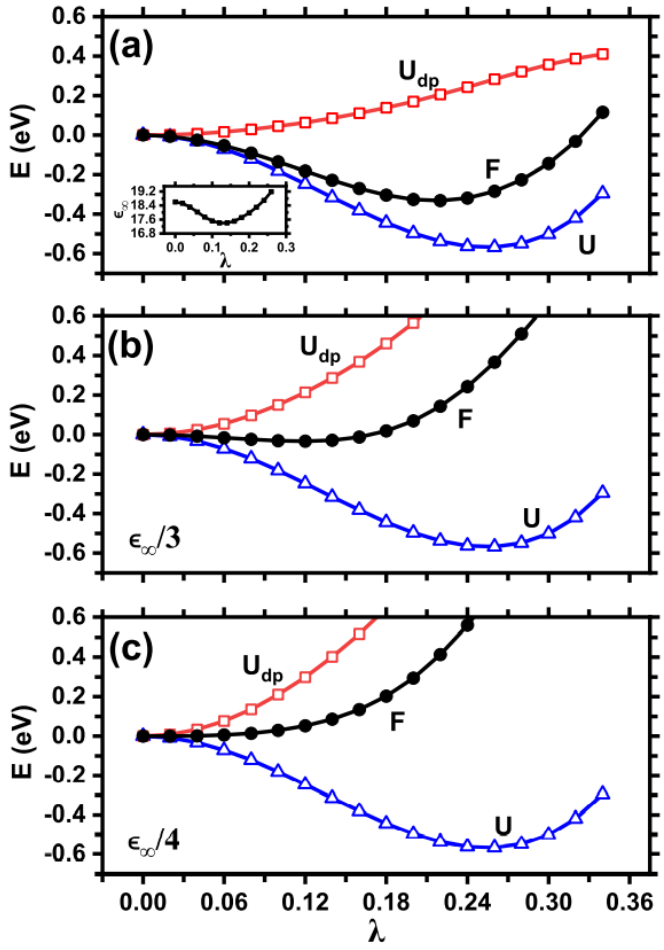

FIG. 3. 3: (a) Electric free-energy $F(\lambda)$ (solid dots), internal energy $U(\lambda)$ (empty triangles), and depolarization energy $U_{dp}(\lambda)$ (empty squares) in −2% strained LiZnSb under OCBC as a function of λ. The calculated high-frequency dielectric constant $\epsilon_\infty(\lambda)$ is shown in the inset. (b) The same as (a), except that ϵ_∞ is artificially reduced to 1/3 of its original value. (c) The same as (a), except that ϵ_∞ is reduced to 1/4 of its original value.

When LiZnSb is under OCBC (i.e., when non-analytic C^{na} contribution is included), we find that the polar LO mode, $A_{2u}LO_1$, remains soft with imaginary frequency ω = 90.6i cm^{-1}, which indicates a structural instability under OCBC and a (possible) existence of HyFE. The phonon eigenvector of $A_{2u}LO_1$ is shown in Fig.3.1(e). Interestingly, compared to the transverse $A_{2u}TO_1$ mode in Fig.3.1(c), the longitudinal $A_{2u}LO_1$ mode in Fig.3.1(e) exhibits a (drastically) enhanced displacement from Li atoms, while the Zn and Sb displacements remain large. Therefore, Li atoms play an important role in forming the soft LO mode. Our calculations also show that, under OCBC,

the frequency of the non-polar B_{1g} mode remains almost unchanged at $\omega = 68.2i$ cm^{-1}, which is not surprising since this mode is non-polar and does not interact with the macroscopic electric field.

After finding that $A_{2u}LO_1$ is soft in LiZnSb under a -2% inplane strain, we compute the electric free energy F for the configuration path along the eigendisplacement direction of this soft mode. If F exhibits a minimum at a configuration of nonzero polarization, then by definition the system is HyFE. The calculated free-energy $F(\lambda)$ of LiZnSb under OCBC is depicted in Fig.3.3(a), where the internal energy $U(\lambda)$ and the depolarization energy $U_{dp}(\lambda)$ are also plotted for comparison. Fig.3.3(a) shows that, as λ deviates from zero, the free energy F starts to decrease, reaches a minimum at $\lambda=\pm0.22$, and then increases [see the curve of solid dots in Fig.3.3(a)]. Our results in Fig.3.3(a) hence reveal that LiZnSb at the PE configuration (i.e., $\lambda=0$) possesses a higher energy and is unstable under OCBC, and instead, LiZnSb prefers to be HyFE at nonzero λ. We thus find that LiZnSb is HyFE. We denote the configuration of LiZnSb at optimal $\lambda=\pm0.22$ as the LO-induced HyFE phase.

Importantly, Fig.3.3(a) further reveals that the free-energy well depth is ΔF_{HyFE}=-332 meV, which is remarkably large. In fact, this HyFE well depth in LiZnSb is more than *one hundred times* deeper than the HyFE well depth of -1.9 meV reported in $LiNbO_3$ [13]. Furthermore, it is also worth pointing out that the *hyperferroelectric* well depth of LiZnSb under an *open-circuit* boundary condition is comparable to the ferroelectric well depth (about -200 meV) of bulk $PbTiO_3$ under a *short-circuit* boundary condition [37]. This tells us that (i) the hyperferroelectricity in LiZnSb is indeed very stable, and (ii) Since the ferroelectric Curie temperature of bulk $PbTiO_3$ is 493 ˚C, LiZnSb is thus likely to be hyperferroelectric at room temperature, which is appealing because it does not require cooling.

We find that the large depth of the HyFE free-energy well in LiZnSb is caused by the combination of a *deep* well of the internal energy U and a *small* depolarization energy U_{dp}. As shown in Fig.3.3(a), at optimal λ=0.22, U is -0.537 eV, and meanwhile, U_{dp} is small and merely 0.205 eV, which gives rise to a strongly negative value of -0.332 eV in free energy F. Furthermore, we also calculate the electric free-energy along the configuration path of the non-polar B_{1g} mode, and find that the lowest free energy is ΔF=-150 meV, which is significantly higher than ΔF_{HyFE}=-332 meV of the LO-induced HyFE phase. This confirms that the ground state of LiZnSb is indeed HyFE under OCBC.

We also calculate the electric polarization of the HyFE phase under OCBC, using the modern theory of polarization via the geometrical Berry-phase approach [30, 31]. At optimal λ=0.22, the magnitude of the HyFE polarization under OCBC is found to be P_{HyFE}=0.282 C/m^2, which is gigantic. Note that this HyFE polarization is about 10 times larger than the P_{HyFE} value of ~0.023 C/m^2 reported in LiBeSe [1] as well as in $LiNbO_3$ [13]. As a matter of fact, the HyFE polarization in LiZnSb under *open-circuit* boundary condition is remarkably comparable to the polarization of 0.21 C/m^2 in bulk ferroelectric $BaTiO_3$ under *short-circuit* boundary condition [18], despite that there is a strong depolarization field in LiZnSb. This large HyFE polarization is very attractive since it shall open many possibilities for hyperferroelectric applications; for instance, the HyFE polarization can be utilized to control the transport properties of semiconductors, superconductors, and/or topological insulators by forming interfaces or heterostructures.

C. Origin of the large and stable HyFE in LiZnSb

With the discovery of a giant polarization under OCBC and attractively stable hyperferroelectricity in LiZnSb, we now attempt to provide the physical origin of these interesting phenomena. We find that the strong hyperferroelectricity in LiZnSb can be attributed to two key

quantities: (i) a large mode effective charge (MEC) of soft LO phonon, and (ii) a large high-frequency dielectric constant ϵ_∞ (i.e., from the electronic contribution). Here, the Σ_∞^{33} component of the high-frequency dielectric tensor is abbreviated as ϵ_∞.

We first find that a large mode effective charge is important in order to generate a large HyFE polarization. For an arbitrary phonon mode with normalized eigendisplacement $u_{i\beta}^{n\vec{q}}$, the mode-specific effective charge $\tilde{Z}_\alpha^{n\vec{q}}$ is defined as [13]

$$\tilde{Z}_\alpha^{n\vec{q}} = \sum_{i\beta} Z_{i,\alpha\beta}^* \, u_{i\beta}^{n\vec{q}}, \tag{2}$$

where *n* is the index of phonon branch, $\vec{q}$ the phonon wave vector, *i* the atom index, Z_i^* the dynamic Born effective-charge tensor of atom *i*, and α and β are the indices of Cartesian directions. Note that, after the summation over β in Eq.(2), $\tilde{Z}_\alpha^{n\vec{q}}$ is a vector (not a tensor). Using the definition of MEC, it is straightforward to show that the HyFE polarization is directly proportional to MEC as $\Delta P_\alpha = \frac{1}{\Omega}\tilde{Z}_\alpha^{n\vec{q}} c\Delta\lambda$, where *c* is the *c*-axis lattice constant. A large MEC will thus generate a large HyFE polarization. The most important component of MEC is the $\tilde{Z}_3$ component along the polarization direction. We quantitatively calculate the $\tilde{Z}_3$ value for the soft longitudinal-optic $A_{2u}LO_1$ mode in LiZnSb under -2% strain, and the obtained $\tilde{Z}_3$ value is 2.59. To illustrate whether this value is large or small, we compare it to the $\tilde{Z}_3$ value (merely 0.39) of soft LO mode in $LiNbO_3$ [13]. We see that the $\tilde{Z}_3$ value in LiZnSb is more than 600% larger than the value in $LiNbO_3$, which is one key reason why the HyFE polarization in LiZnSb is large [38].

To demonstrate the importance of the high-frequency dielectric constant ϵ_∞, we artificially reduce the ϵ_∞ value by a factor of 1/3 (as well as by a factor of 1/4), and then recalculate the electric free energy *F* along the $A_{2u}LO_1$ configuration path. The calculated free energies are given in Fig.3.3(b) and Fig.3.3(c). Fig.3.3(b) shows that, when the dielectric constant is changed to 1/3

of the original value, the free-energy well depth sharply decreases to ΔF=-33.4 meV, which is much smaller than the original value ΔF=-332 meV in Fig.3.3(a). And furthermore, the optimal λ of the free energy in Fig.3.3(b) is also significantly reduced to λ=0.12, as compared to λ=0.22 in Fig.3.3(a). Since the HyFE polarization is directly proportional to the optimal λ, we thus see from Fig.3.3(b) that, when ϵ_∞ is reduced, both the HyFE instability and the HyFE polarization are drastically weakened. When the dielectric constant ϵ_∞ is further reduced to 1/4 of the original value in Fig.3.3(c), we notice that the minimum of the electric free energy is no longer located at a nonzero λ. Instead, it is located at λ=0, and the PE phase becomes most stable under OCBC. Therefore the system is not HyFE. The calculation results in Fig.3.3(b) and Fig.3.3(c) thus demonstrate that the large dielectric constant ϵ_∞ in LiZnSb is indeed important.

It is rather intuitive to understand why both MEC and ϵ_∞ are important in order to produce strong HyFE. First, to generate large P_{HyFE} polarization, a large $\tilde{Z}_3$ of soft LO phonon is needed since P_{HyFE} is proportional to $\tilde{Z}_3$. Meanwhile, a large P_{HyFE} tends to (detrimentally) give rise to a large depolarization energy U_{dp}, which reduces the well depth ΔF of the HyFE free energy and weakens the HyFE instability. To reduce U_{dp} while maintaining a large P_{HyFE}, large ϵ_∞ is thus needed since U_{dp} is inversely proportional to ϵ_∞ according to Eq.(1) [39].

Our finding that large high-frequency dielectric constant ϵ_∞ is beneficial to generate strong HyFE also provides useful guide for searching new HyFE materials. Since large ϵ_∞ is often associated with small electronic band gap [40], new HyFE materials with strong HyFE should thus have a small band gap and a large mode effective charge of soft LO phonon.

We recognize that materials of small band gap tend to have a low dielectric breakdown electric field. It is thus helpful to estimate the hyperferroelectricity-switching electric field E_s and the dielectric breakdown electric field E_b in LiZnSb. Considering the facts that (i) the free-energy

barrier (~0.3 eV) of LiZnSb under OCBC is comparable to the internal-energy barrier (~0.2 eV) of $PbTiO_3$ under SCBC, and (ii) the (intrinsic) switching electric field in $PbTiO_3$ thin film is on the order of 10^7 V/m in experiment [41], it is thus reasonable that the intrinsic switching electric field E_s of the hyperferroelectricity in LiZnSb under OCBC will be also on the order of 10^7 V/m. Note that the extrinsic switching field will be one or two orders of magnitude smaller than the intrinsic switching field, since the nucleation of opposite domain is easier due to the existence of defect or domain wall. Real E_s may thus be considerably lower than the value estimated above. Meanwhile, the breakdown electric field E_b of LiZnSb can be estimated using $\frac{1}{\epsilon_r} E_b d = E_g$, where ϵ_r=30 is the relative zero-frequency dielectric constant, E_g≈0.3 eV is the band gap, and d is the film thickness. For d=20 nm LiZnSb film under OCBC, the breakdown field E_b is estimated to be 4.5×10^8 V/m, which is significantly higher than the switching field E_s. Therefore, it is possible that the hypeferroelectricity in LiZnSb can be switched.

There is subtle and important difference between hyperferroelectrics and polar metals, although the band gap of LiZnSb is small. Hyperferroelectrics require the existence of soft LO modes (and this soft LO mode often needs to have a large mode effective charge). In contrast, polar metals may not possess soft LO modes and are thus not hyperferroelectric, even if strain opens the band gap. For instance, doping a small amount of free carriers into $PbTiO_3$ may make it to become polar metal. But $PbTiO_3$ does not possess a soft LO mode, and is thus not hyperferroelectric.

One intriguing question centers on the role of Li atoms in hyperferroelectricity. To determine the role of Li atoms, we consider LiZnSb under a -2% strain at the optimal configuration of λ=0.22, and we constrain the displacement of Li atoms in the soft $A_{2u}LO_1$ mode to be zero (namely the Li atoms are fixed in positions). We then calculate the internal energy U, polarization P under OCBC,

depolarization energy U_{dp}, and free energy F. By comparing the values of these quantities with their counterparts (which are obtained when Li atoms are not constrained), we can quantitatively determine how Li atoms affect hyperferroelectricity. We obtain U=-0.577 eV, P=0.416 C/m^2, U_{dp}=0.426 eV, and F=-0.151 eV for the Li-constrained system, as compared to U=-0.537 eV, P=0.259 C/m^2, U_{dp}=0.205 eV, and F=-0.332 eV for Li-unconstrained system. We thus see that, by allowing Li atoms to move, the depolarization energy U_{dp} decreases drastically by more than 50% from 0.426 eV in the Li-constrained system to merely 0.205 eV in the Li-unconstrained system, due to the fact that polarization P is significantly smaller in the latter. As a consequence, the free energy F is lowered considerably in the Li-unconstrained system, which stabilizes the hyperferroelectricity. Therefore, the Li atoms play an important role to stabilize hyperferroelectricity in LiZnSb by decreasing the polarization (and thus the depolarization energy) under OCBC. This is indeed consistent with the soft $A_{2u}LO_1$ mode in Fig.3.1(e), where the Li atoms move opposite to the Zn atoms (thus opposite to the direction of polarization).

D. Strain effects on HyFE

After revealing the origin of strong HyFE in LiZnSb, we now go one step further and investigate how the HyFE polarization—and the free-energy well depth—can be tuned by inplane strain. It is previously demonstrated that inplane strain alters *ferroelectricity* under SCBC [42-46]. However, the knowledge cannot be naively applied to *hyperferroelectricity* under OCBC, since the (strong) depolarization field plays a critical role on HyFE under OCBC (but not on FE under SCBC). Therefore, it remains intriguing to investigate how the HyFE properties under OCBC depend on the inplane strain. Furthermore, it is also interesting to examine how the response of HyFE under OCBC to the inplane strain may differ from (or resemble) that of FE under SCBC.

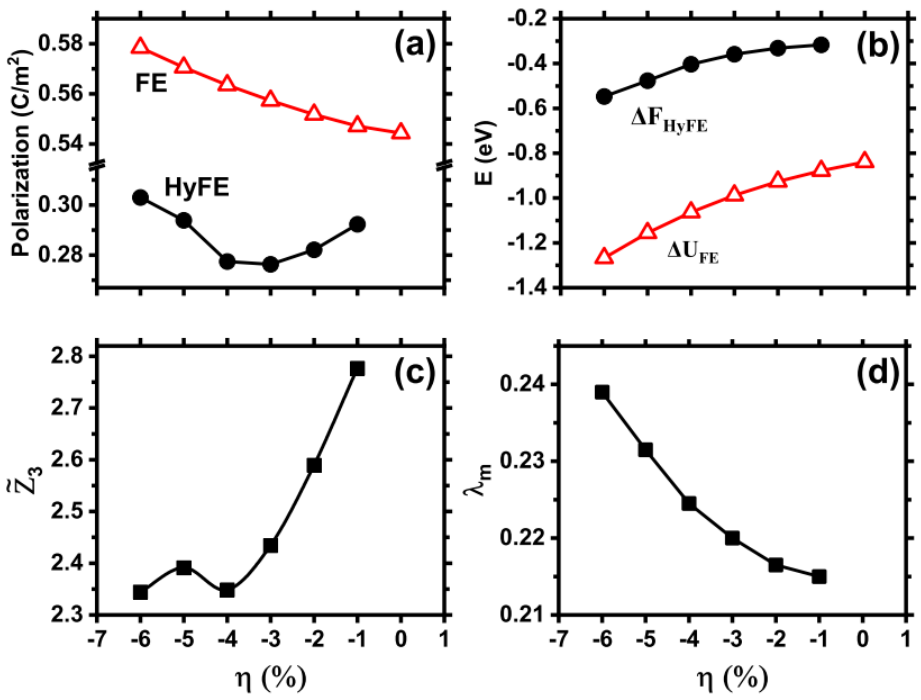

FIG. 3. 4: The dependences of the following quantities in LiZnSb as a functions of the compressive inplane strain η: (a) The HyFE polarization under OCBC (solid dots) and the FE polarization under SCBC (empty triangles); (b) The free-energy well depth ΔF_{HyFE} of hyperferroelectricity under OCBC (solid dots), and the internal-energy well depth ΔU_{FE} of ferroelectricity under SCBC (empty triangles); (c) The mode-specific effective charge $\tilde{Z}_3$ of $A_{2u}(LO_1)$ phonon; (d) The optimal λ_m.

The calculated HyFE polarizations in LiZnSb under OCBC are given in Fig.3.4(a) for different inplane strains. For comparison, we also show in Fig.3.4(a) our calculated results on the FE polarization under SCBC. Fig.3.4(a) tells us that the FE polarization under SCBC increases monotonously as strain η varies from 0% to -6% [see the empty triangles in Fig.3.4(a)], which is not surprising [42-45]. However, and interestingly, for the HyFE polarization (P_{HyFE}) under OCBC, the behavior drastically differs: P_{HyFE} first *decreases* from 0.292 C/m^2 to 0.276 C/m^2 when strain changes from -1% to -3% (thus yielding a negative piezoelectric coefficient [46]), and then increases from 0.277 C/m^2 to 0.303 C/m^2 when strain varies from -4% to -6% [see the solid dots in Fig.3.4(a)]. P_{HyFE} thus depends on the inplane strain in a non-monotonous manner. Therefore,

Fig.3.4(a) reveals one important outcome, that is, the hyperferroelectric polarization responds to the inplane strain very differently from the ferroelectric polarization. Also notably, for every inplane strain within the considered strain range in Fig.3.4(a), the HyFE polarization is found to be large and around 0.28 C/m^2, which is useful for technological applications.

We like to point out that, for unstrained LiZnSb, although the PE phase is metallic, it may still be possible to determine the hyperferroelectric P_{HyFE} polarization as follows. We start with the PE LiZnSb and move atoms along the nonpolar B_{1g} mode to a configuration where LiZnSb becomes insulating and meanwhile possesses an unstable LO mode. This insulating atomic configuration is still nonpolar and is used as a zero reference to calculate polarization. We then move atoms along the unstable LO mode and find the most stable hyperferroelectric phase. Using this approach we obtain the P_{HyFE} polarization in unstrained LiZnSb to be 0.292 C/m^2 under OCBC.

Furthermore, we also examine how another important HyFE quantity, namely the well depth (ΔF_{HyFE}) of the HyFE free energy under OCBC, depends on the inplane strain. The calculated ΔF_{HyFE} is shown in Fig.3.4(b), in comparison with the well depth ΔU_{FE} of ferroelectricity under SCBC. Fig.3.4(b) tells us that the absolute value of the HyFE free-energy well depth ΔF_{HyFE} increases with the compressive strain, varying from 0.32 eV at η=-1% to 0.55 eV at η=-6% [see the solid dots in Fig.3.4(b)]. This reveals that the HyFE instability can be effectively tuned by the inplane strain.

The discovery of a non-monotonous dependence of the HyFE polarization with the inplane strain in Fig.3.4(a) is interesting, and meanwhile, puzzling. We next provide a possible physical mechanism which leads to this unusual behavior. First we find that the decrease of P_{HyFE} from η=-1% to η=-3% is caused by the decrease in the mode effective charge $\tilde{Z}_3$. $\tilde{Z}_3$ of soft A_{2u} (LO_1) phonon is given in Fig.3.4(c), showing that $\tilde{Z}_3$ decreases significantly from η=-1% to η=-3%. Since

the HyFE polarization is directly proportional to $\tilde{Z}_3$, the decrease of $\tilde{Z}_3$ thus leads to the decline of the HyFE polarization in the considered strain range. Considering that the Born effective charges are often valid only within the linear regime [47], we need be slightly cautious. To confirm our explanation, we compute the polarization P_{BEC} using the mode effective charge as $P_{BEC} = \frac{1}{\Omega}\tilde{Z}_3 c\lambda_m$. We find that P_{BEC} indeed follows a similar non-monotonous behavior as the Berry-phase polarization P_{HyFE} in Fig.3.4(a), showing that our explanation is reasonable.

On the other hand, the increase of P_{HyFE} from η=-4% to η=-6% in Fig.3.4(a) can be attributed to the strain-induced increase of optimal λ_m (Note that λ_m is defined as the λ value where the electric free energy is at minimum). Fig.3.4(d) shows the optimal λ_m value as a function of inplane strain. From -1% to -3% strains, λ_m is similar and increases only slightly. However, when strain is varied from -4% to -6%, λ_m increases more drastically, which gives rise to the enlarged HyFE polarization since P_{HyFE} is proportional to λ_m. This is indeed consistent with Fig.3.4(a) when strain varies from -4% to -6%.

Our finding on the strain dependence of hyperferroelectricity in LiZnSb could be technologically useful for the following reasons: (i) It reveals that the HyFE polarization can be effectively tuned by strains, despite the existence of strong depolarization field under OCBC. (ii) It also tells that the well depth of the HyFE free energy and HyFE instability can be considerably adjusted by inplane strain. This can be used to modify the Curie temperature for hyperferroelectricity. Furthermore, it may also be utilized to decrease the HyFE well depth, making the HyFE polarization easier to switch.

IV. Conclusions

A combination of three different methods—including the linear-response density-functional perturbation theory, the electric free-energy, and the modern theory of polarization—are used to

investigate the hyperferroelectricity in LiZnSb. Furthermore, the strain dependence of the hyperferroelectric properties is also studied. Our main findings are summarized in the following.

(i) A giant hyperferroelectricity is discovered in LiZnSb. More specifically, in LiZnSb under -2% strain, the HyFE polarization under an open-circuit boundary condition is found to be 0.282 C/m^2, despite the existence of depolarization field. This magnitude of polarization under OCBC is ten times larger than most of the HyFE polarizations reported so far in other materials [1, 13], and is in fact comparable to the ferroelectric polarization of prototypical bulk $BaTiO_3$ under SCBC (i.e., without the depolarization field). This giant HyFE polarization should open many technological applications of hyperferroelectricity.

(ii) The hyperferroelectricity in LiZnSb under OCBC is shown to be robust and remarkably stable. The well depth of free energy in LiZnSb under -2% strain is determined to be -332 meV. Note that this well depth is under OCBC, and its value is comparable to the FE well depth (-200 meV) of bulk $PbTiO_3$ under SCBC. Considering that the Curie temperature of bulk $PbTiO_3$ is T_C=493 ˚C, our result indicates that LiZnSb under OCBC is hyperferroelectric at room temperature.

(iii) The origin of the strong hyperferroelectricity in LiZnSb is found to come from two factors, both being important. One is the large mode effective charge of the soft $A_{2u}LO_1$ phonon, and the other is a large high-frequency dielectric constant ϵ_∞.

A large MEC of the soft $A_{2u}LO_1$ phonon is critical since it can produce a large HyFE polarization. In LiZnSb under -2% strain, $\tilde{Z}_3$ of soft $A_{2u}LO_1$ phonon is calculated to be 2.59, which is more than 600% times larger than the value of 0.39 in another hyperferroelectric $LiNbO_3$. Since the HyFE polarization is directly proportional to $\tilde{Z}_3$ of the soft LO phonon, a large MEC will thus lead to a large HyFE polarization.

Meanwhile, a large HyFE polarization often detrimentally gives rise to a strong depolarization field which tends to eliminate hyperferroelectricity. To maintain HyFE, large dielectric ϵ_∞ constant becomes necessary and important, since it reduces the depolarization energy [see Eq.(1)], and allows the well depth of electric free energy to be deep, thus stabilizing HyFE. Our calculations reveal that, when ϵ_∞ is reduced to 1/3 of its original value in LiZnSb, the free-energy well depth is drastically reduced by a factor of ten from ΔF=-332 meV to ΔF=-33.4 meV, showing that the HyFE instability is strongly suppressed. When ϵ_∞ is further reduced to 1/4 of its original value, HyFE completely disappears.

(iv) We further find that both the HyFE polarization and the HyFE free-energy well depth can be effectively tuned by inplane strain (Fig.3.4). This tunability allows us to adjust the HyFE well depth and polarization, depending on what is needed in practical applications. Moreover, we also reveal that the HyFE polarization responds to the inplane strain in a (considerably) different manner than the FE polarization. While the FE polarization in LiZnSb under SCBC shows a continuous increase with the increasing compressive strain, the HyFE polarization under OCBC nevertheless exhibits an interesting and non-monotonous strain dependence. Considering that hyperferroelectricity is an intriguing new phenomenon, we hope that the rich and interesting results obtained in this study will stimulate more theoretical and experimental interest in the field.

V. Acknowledgments

This work was partially supported by the Office of Naval Research. Computations were performed on the computing facilities provided by the Arkansas High-Performance Computing Center, supported by NSF.

VI. Appendix

A. Electronic band structures and electric free energies of LiZnSb under different compressive inplane strains

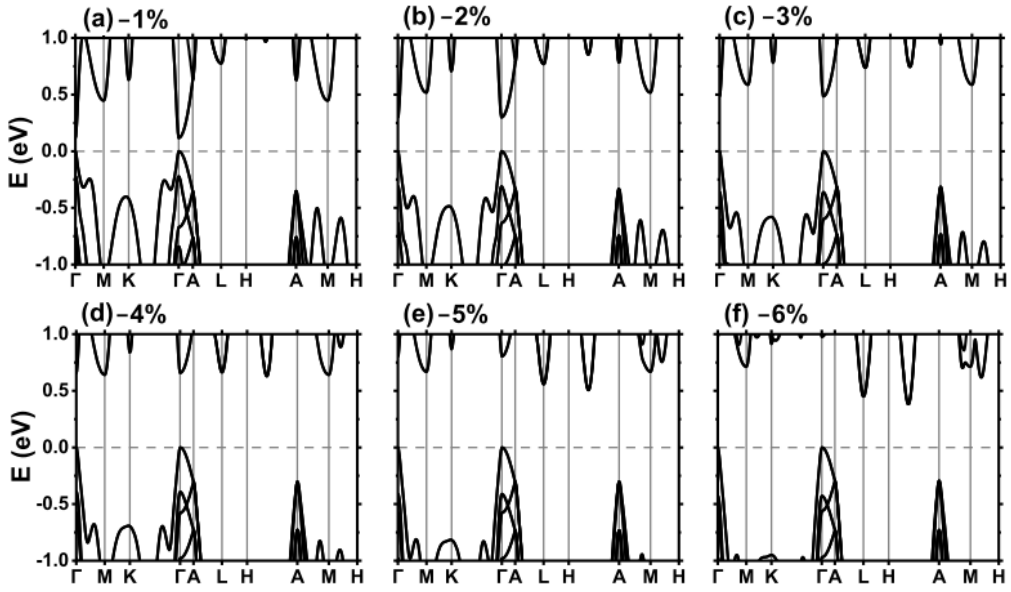

FIG. 3. 5: Electronic band structure of centro-symmetric LiZnSb under the following compressive inplane strains: *(*a) -1%, *(*b) -2%, *(*c) -3%, *(*d) -4%, *(*e) -5%, and *(*f) -6%. The band gap is direct in *(*a)-*(*c), and becomes indirect in *(*d)-*(*f).

In this Appendix, we describe in detail the calculated electronic band structures of centrosymmetric LiZnSb under different inplane strains, which are reported in Fig.3.5. Fig.3.5(a) reveals that, at -1% strain, a band gap clearly opens at Γ, showing that the system is an insulator, and therefore, both the Born effective charges and the electric polarization are well defined. When strain increases from -1% to -3%, Fig.3.5(b) and Fig.3.5(c) tell us that the band gap increases, and the gap is direct at the zone-center Γ point. As strain is further increased to -4%, the *local* conduction band minima (CBM) have similar energies at several $\vec{k}$ points, while the valence band maximum (VBM) remains at Γ [see Fig.3.5(d)]. When the strain continues to increase from -4% to -6%, Fig.3.5(e) and Fig.3.5(f) reveal that (i) the fundamental band gap in this strain range is no

longer direct. More specifically, the CBM state changes from Γ to a $\vec{k}$ point between H and A, while the VBM state is still located at Γ. (ii) The fundamental band gap starts to decrease. Nevertheless, the system remains to have a finite band gap in the whole considered strain range (i.e., from -1% to -6%).

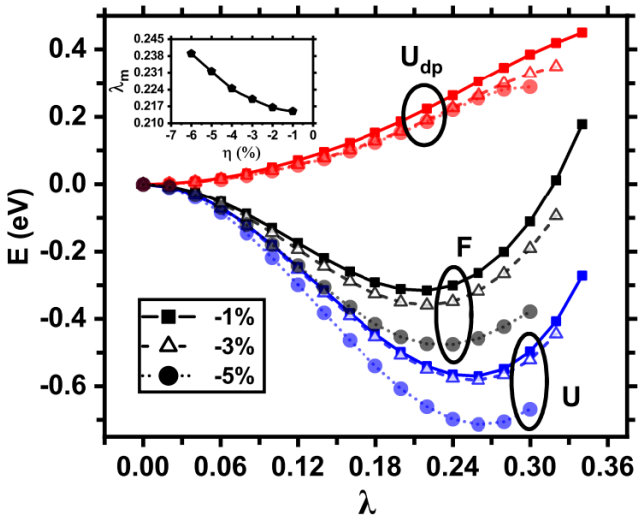

FIG. 3. 6: shows the electric free energy in LiZnSb under -1%, -3% and -5% strains, where the internal energy U and depolarization energy U_{dp} are also plotted. Fig.3.6 reveals that (i) the well depth of free energy becomes deeper as strain increases, and (ii) the depolarization energies of different inplane strains remain small and interestingly similar, since the high-frequency dielectric ϵ_∞ constant is high for all considered strains.

References

[1] K. F. Garrity, K. M. Rabe, and D. Vanderbilt, Phys. Rev. Lett. **112**, 127601 (2014).

[2] H. Fu, J. Appl. Phys. **116**, 164104 (2014).

[3] P. Li, X. Ren, G.-C. Guo, and L. He, Sci. Rep. **6**, 34085 (2016).

[4] C. J. Fennie and K. M. Rabe, Phys. Rev. B **72**, 100103(R) (2005).

[5] E. Bousquet, M. Dawber, N. Stucki, C. Lichtensteiger, P. Hermet, S. Gariglio, J.-M. Triscone, and P. Ghosez, Nature (London) **452**, 732 (2008).

[6] N. A. Benedek and C. J. Fennie, Phys. Rev. Lett. **106**, 107204 (2011).

[7] P. Chen, M.N. Grisolia, H.J. Zhao, O.E. Gonzalez-Vazquez, L. Bellaiche, M. Bibes, B.-G. Liu, and J. Iniguez, Phys. Rev. B **97**, 024113 (2018).

[8] M. Dawber, K.M. Rabe, and J.F. Scott, Rev. Mod. Phys. **77**, 1083 (2005).

[9] J. Junquera and P. Ghosez, Nature (London) **422**, 506 (2003).

[10] N.A. Benedek and M. Stengel, Polarization that Holds Steady, Physics **7**, 32 (2014).

[11] J.F. Scott and C.A. Paz de Araujo, Ferroelectric Memories, Science **246**, 1400 (1989).

[12] J.F. Scott, *Ferroelectric Memories* (Springer, Berlin, 2000).

[13] S. Qiu, L. Ma, S. Liu, and H. Fu, Phys. Rev. B. **104**, 064112 (2021).

[14] S. Liu and R.E. Cohen, Phys. Rev. Lett. **119**, 207601 (2017).

[15] D. Du, P. J. Strohbeen, H. Paik, C. Zhang, K. T. Genser, K. M. Rabe, P. M. Voyles, D. G. Schlom, and J. K. Kawasaki, Journal of Vacuum Science and Technology B **38**, 022208 (2020).

[16] M. A. White, G. J. Miller, and J. Vela, J. Am. Chem. Soc. **138**, 14574 (2016).

[17] R. Adhikari and H. Fu, Phys. Rev. B **99**, 104101 (2019).

[18] H. Fu and R.E. Cohen, Nature (London) **403**, 281 (2000).

[19] P. Hohenberg and W. Kohn, Phys. Rev. **136**, B864 (1964); W. Kohn and L.J. Sham, Phys. Rev. **140**, A1133 (1965).

[20] P. Giannozzi, S. Baroni, N. Bonini, M. Calandra, R. Car, C. Cavazzoni, D. Ceresoli, G.L. Chiarotti, M. Cococcioni, I. Dabo, A. Dal Corso, S. Fabris, G. Fratesi, S. de Gironcoli, R. Gebauer, U. Gerstmann, C. Gougoussis, A. Kokalj, M. Lazzeri, L. Martin-Samos, N. Marzari, F. Mauri, R. Mazzarello, S. Paolini, A. Pasquarello, L. Paulatto, C. Sbraccia, S. Scandolo, G. Sclauzero, A.P. Seitsonen, A. Smogunov, P. Umari, R.M. Wentzcovitch, J. Phys. Condens. Matter **21**, 395502 (2009).

[21] https://www.quantum-espresso.org.

[22] N. Troullier and J. L. Martins, Phys. Rev. B **43**, 1993 (1991).

[23] The configurations for generating pseudopotentials are $1s^2 2p^{0.05}$ for Li, $3d^{10} 4s^1 4p^{0.1}$ for Zn, and $5s^2 5p^{2.5} 5d^{0.1}$ for Sb. The matching radii of pseudo-wavefunction and all-electron wavefunction are $r_{cut}^{s,p}$=1.5, 3.0 Bohr for Li, $r_{cut}^{s,p,d}$=2.0, 2.0, 2.5 Bohr for Zn, and $r_{cut}^{s,p,d}$ =1.8, 1.8, 2.5 Bohr for Sb. The local channel of pseudopotential is chosen to be the screened Coulomb potential with r_c=1.30 Bohr for Li, the 4*s* pseudopotential for Zn, and the 5*s* pseudopotential for Sb.

[24] S. Baroni, S. Gironcoli, A. D. Corso, and P. Giannozzi, Rev. Mod. Phys. **73**, 515-562 (2001).

[25] S. Baroni, P. Giannozzi, and T. Testa, Phys. Rev. Lett. **58**, 1861 (1987).

[26] X. Gonze, Adiabatic density-functional perturbation theory, Phys. Rev. A **52**, 1096 (1995).

[27] X. Gonze and C. Lee, Phys. Rev. B **55**, 10355 (1997).

[28] M. Born and K. Huang, *Dynamical theory of crystal lattices* (Clarendon press, Oxford, 1988).

[29] M. Stengel, N. A. Spaldin, and D. Vanderbilt, Nat. Phys. **5**, 304-308 (2009).

[30] R. D. King-Smith and D. Vanderbilt, Phys. Rev. B **47**, 1651-1654 (1993).

[31] R. Resta, Rev. Mod. Phys. **66**, 889-915 (1994).

[32] Y. Yao and H. Fu, Phys. Rev. B **79**, 014103 (2009).

[33] J. W. Bennett, K. F. Garrity, K. M. Rabe, and D. Vanderbilt, Phys. Rev. Lett. **109**, 167602 (2012).

[34] Dj. Guendouz, Z. Charifi, H. Baaziz, F. Soyalp, G. Ugur, and S. Ugur, Physica B **519**, 39-52 (2017).

[35] A. Raeliarijaona and H. Fu, Phys. Rev. B **92**, 094303 (2015).

[36] H. Fu, Phys. Rev. B **102**, 134118 (2020).

[37] R. E. Cohen, Origin of ferroelectricity in perovskite oxides, Nature (London) **358**, 136 (1992).

[38] We also compute the Z_{e3} value for the soft transverse-optic $A_{2u}(TO_1)$ mode in LiZnSb (note that it is the soft TO mode), and the value is 3.98. The Z_{e3} value of the soft LO mode is thus comparable to that of the soft TO mode.

[39] There are two mechanisms to generate hyperferroelectricity. The mechanisms for strong HyFE in LiZnSb and for weak HyFE in $LiNbO_3$ are rather different. In $LiNbO_3$ of weak HyFE, MEC is small, which leads to a small HyFE polarization and a small depolarization energy. In LiZnSb of strong HyFE, MEC is large, and ϵ_∞ need be large too.

[40] P. Yu and M. Cardona, *Fundamentals of Semiconductors* (Springer, Berlin, 1996).

[41] R. Xu, R. Gao, S. E. Reyes-Lillo, S. Saremi, Y. Dong, H. Lu, Z. Chen, X. Lu, Y. Qi, S.-L. Hsu, A. R. Damodaran, H. Zhou, J. B. Neaton, and L. W. Martin, ACS Nano. **12**, 4736 (2018). 037601 (2019).

[42] J. H. Haeni, P. Irvin, W. Chang, R. Uecker, P. Reiche, Y. L. Li, S. Choudhury, W. Tian, M. E. Hawley, B. Craigo, A. K. Tagantsev, X. Q. Pan, S. K. Streiffer, L. Q. Chen, S. W. Kirchoefer, J. Levy, and D. G. Schlom, Nature **430**, 758 (2004).

[43] C. Ederer and N.A. Spaldin, Phys. Rev. Lett. **95**, 257601 (2005).

[44] H. N. Lee, S. M. Nakhmanson, M. F. Chisholm, H. M. Christen, K. M. Rabe, and D. Vanderbilt, Phys. Rev. Lett. **98**, 217602 (2007).

[45] Y. Yao and H. Fu, Phys. Rev. B **80**, 035126 (2009).

[46] S. Dutta, P. Buragohain, S. Glinsek, C. Richter, H. Aramberri, H. Lu, U. Schroeder, E. Defay, A. Gruverman, and J. Iniguez, Nat. Commun. **12**, 7301 (2021).

[47] A. Chanana and U. V. Waghmare, Phys. Rev. Lett. **123**,

Conclusion

This dissertation contains three projects that present a comprehensive study of the extended oxygen vacancies in $BaTiO_3$ and hyperferroelectric properties in $LiNbO_3$, and LiZnSb. By utilizing density functional theory, linear-response perturbation theory, the modern theory of polarization, and electric free energy, we have uncovered critical insights into the underlying mechanisms that govern planar oxygen vacancies in $BaTiO_3$ and hyperferroelectricity in $LiNbO_3$ and LiZnSb. Our studies have led to significant findings, including the formation and the effects of planar oxygen vacancies V_O^q in $BaTiO_3$, the possible polarization tri-stability and tunability in $LiNbO_3$ under OCBC, and the discovery of a giant hyperferroelectricity in LiZnSb. These findings provide profound contributions to the fundamental understanding of ferroelectric materials under different conditions and their potential applications in various technological fields. We summarize our findings in the following.

Planar oxygen vacancies in $BaTiO_3$. An extensive investigation of planar oxygen vacancies with charge states 0, 1+ and 2+ in ferroelectric $BaTiO_3$ have been conducted. We examinate the properties include the energetics of vacancy formation, conditions to control the formation of planar V_O^q vacancies, insulating or conducting nature of different vacancy-charge states, the magnitude of electric polarization when planar vacancies are presented, and the microscopic structure insight.

More specifically, we find that (i) under the oxygen-poor condition, planar V_O^q vacancies can spontaneously form in $BaTiO_3$. We also find that, even under the oxygen-rich condition, the formation energy of planar V_O^{2+} vacancies is only 0.54 eV when chemical potential of electron reservoir μ_e is near VBM, which is small and indicates that planar V_O^{2+} vacancies are easy to form. Moreover, it is possible to make each of the charge states of oxygen vacancies most stable by

adjusting the chemical potential μ_e. We quantitatively determined that the most stable regions for the three charge states of oxygen vacancies are as follows: V_O^{2+} is most stable for μ_e values below 1.22 eV, V_O^{1+} is most stable for μ_e values between 1.22 and 2.22 eV, and V_O^{2+} is most stable for μ_e values greater than 2.22 eV.

(ii) We have identified the optimal conditions for growing or eliminating planar oxygen vacancies of all three charge states in $BaTiO_3$. If planar oxygen vacancies are desirable and need to be intentionally generated, the corresponding optimal condition, Condition G, is to choose μ_O around -3.0 eV and adjust μ_e to be within the range of 1.6 to 2.4 eV. This is because the formation energies of all three charge states are small, ~0.6 eV. Additionally, this knowledge provides the advantage of being able to change the most stable charge state of planar V_O^q vacancies by altering μ_e, which allows the tuning of transport properties. Conversely, if planar oxygen vacancies are harmful and need to be eliminated, $BaTiO_3$ should be grown under the oxygen-rich condition ($\mu_O = 0$ eV) and adjust μ_e to be near CBM, namely Condition E.

(iii) $BaTiO_3$ that contains planar V_O^{2+} vacancies is an insulator, which means that no mobile charges are present to screen the polarization when ferroelectricity sustains. The band gap of $BaTiO_3$ with V_O^{2+} vacancies is decreased compared to perfect $BaTiO_3$. Furthermore, $BaTiO_3$ with planar oxygen vacancies of two other charge states, namely V_O^{1+} or V_O^0, are found to be metallic. In the metallic cases, the presence of mobile charges should screen the ferroelectricity, or at least partially screen it.

(iv) We calculate the electric polarization in defected $BaTiO_3$ with planar V_O^{2+} vacancies, and our findings shows that these vacancies almost completely eliminate polarization when the spacing S between adjacent V_O^{2+} planes is 24Å. Our calculations also provide compelling evidence that polarization fatigue is likely caused by extended defects rather than isolated ones.

(v) Through the examination of the relative displacement ΔZ of Ti and O atoms, we have discovered that for planar V_O^q vacancies of all three charge states, ΔZ in cell 1 (the bulk cell closest to the vacancy) is significantly enhanced by approximately 300% compared to perfect $BaTiO_3$. This ΔZ enhancement in cell 1 results from the broken Ti-O bond that is created by the vacancies. Additionally, ΔZ in cell 1 decreases as the charge state q changes from +2 to 0, which can be attributed to the decreasing Coulomb interaction. We have also observed that when the spacing *S* is 24Å, ΔZ exhibits mirror symmetry for all three charge states, meaning that ΔZs in cells ±1 are equal and have opposite signs. This symmetry leads to the significant reduction of polarization.

(vi) By increasing the spacing S between adjacent V_O^{2+} planes to 96Å, we found that ferroelectricity is restored, as evidenced by local Ti-O displacements in the region distant from the vacancy plane, as shown in Fig.1.6(b). Additionally, we determined that the total length of the polarization dead layer resulting from planar V_O^{2+} vacancies is approximately 72Å.

Possible existence of tri-stable polarization states in LiNbO3 under OCBC. We investigate the hyperferroelectric properties in $LiNbO_3$ solid under OCBC. We observed that a soft LO mode in $LiNbO_3$ can give rise to a nonzero polarization under OCBC due to the significantly small depolarization energy. However, we found that the ground state of $LiNbO_3$ under OCBC is nonpolar, not hyperferroelectric, despite the presence of the soft LO mode. This suggests that the presence of a soft LO mode is not a guarantee of hyperferroelectricity. Furthermore, our investigation revealed an intriguing phenomenon in $LiNbO_3$ under OCBC: it may possess an unusual, triple potential well. This means that $LiNbO_3$ under OCBC exhibits three stable and/or metastable states with different polarizations.

More specifically, we find that (i) under OCBC, the LO mode $A_{2u}(LO_1)$ is soft with an imaginary frequency of $96i$ cm^{-1} in centrosymmetric $LiNbO_3$. This LO mode can induce

hyperferroelectricity of a free-energy minimum of -9 meV and a polarization P=0.023 C/m^2 under OCBC.

(ii) We identify the origin of this HyFE induced by the soft $A_{2u}(LO_1)$ mode. This phenomenon arises from an exceptionally small depolarization energy of only +4 meV, which, when combined with the internal-energy difference of -13 meV, results in an electric free energy minimum at a non-zero polarization, indicating the presence of hyperferroelectricity. Furthermore, our investigation revealed that the soft $A_{2u}(LO_1)$ mode is a result of the coupling between the soft $A_{2u}(TO_1)$ mode and non-soft $A_{2u}(TO_2)$ mode, with a significant contribution of 61% attributed to the non-soft $A_{2u}(TO_2)$ mode. These findings suggest that non-soft modes may play an important role in the development of hyperferroelectricity.

(iv) We propose that the mode-specific effective charge, $\tilde{Z}_3^{n\vec{q}}$, is a critical physical quantity in the search for and design of new hyperferroelectric materials. We determine that $\tilde{Z}_3^{n\vec{q}}$ is only 0.39 for $A_{2u}(LO_1)$ in $LiNbO_3$, which is 17 times smaller than $\tilde{Z}_3^{n\vec{q}}$=6.65 for $A_{2u}(TO_1)$, which gives rise to a very small depolarization energy U_{dp} and HyFE under OCBC.

(v) We discover that the ground state of $LiNbO_3$ under OCBC is surprisingly not HyFE. In addition to soft $A_{2u}(LO_1)$, there is another soft non-polar A_{2g} mode which dominates the structure distortion and produces a non-polar ground state. Therefore, the existence of a soft LO mode does not guarantee hyperferroelectricity.

(vi) We further propose an interesting possibility that $LiNbO_3$ is polarization tri-stable under OCBC. By following the configuration path varying from the ground-state non-polar nP phase to the polar LO phase, the free-energy potential shows three wells which indicate three stable states. At those states, the polarization values are found to be P=0 and ±0.023 C/m^2 and the free-energy potential wells for the LO and nP phases are calculated to be -1.9 meV and -23 meV, respectively.

Giant hyperferroelectricity in LiZnSb. We investigate the hyperferroelectric properties and its strain dependence in LiZnSb. We find a giant hyperferroelectric polarization, P=0.282 C/m^2, exists in LiZnSb under an in-plane strain of -2%. The hyperferroelectric phase in LiZnSb is discovered to be surprisingly stable, with an electric free-energy well depth of -332 meV. The physical origin responsible for the giant hyperferroelectricity in LiZnSb stems from two facts: the large soft LO mode effective charge and a large high-frequency dielectric constant. Furthermore, we show that the hyperferroelectricity under OCBC in LiZbSb responds differently to in-plane strain compared to its ferroelectricity under SCBC.

More specifically, we find (i) the hyperferroelectricity in LiZnSb is giant under a -2% in-plane strain. The HyFE polarization under OCBC is found to be 0.282 C/m^2, which is ten times larger than most of the HyFE polarizations reported in other materials and is comparable to the ferroelectric polarization of prototypical bulk $BaTiO_3$ under SCBC. The substantial HyFE polarization we observed in this material suggests that it may be suitable for a variety HyFE applications.

(ii) The hyperferroelectricity in LiZnSb under OCBC is remarkably stable. The HyFE electric free-energy well depth in LiZnSb under -2% strain is calculated to be -332 meV, which is deeper than the FE well depth (-200 meV) of $PbTiO_3$ under SCBC, indicating that LiZnSb under OCBC should exhibits hyperferroelectricity at room temperature, given that the Curie temperature of bulk $PbTiO_3$ is T_C=493°C.

(iii) We attribute the strong hyperferroelectricity observed in LiZnSb to the large mode effective charge of the soft LO phonon $A_{2u}LO_1$, as well as the high-frequency dielectric constant ϵ_∞. A large soft phonon MEC is responsible for generating a large HyFE polarization. $\tilde{Z}_3$ of the soft $A_{2u}LO_1$ phonon is calculated to be 2.59 in LiZnSb under a -2% strain, which is more than 6

times larger than $\tilde{Z}_3$=0.39 in hyperferroelectric $LiNbO_3$ found in Chapter 2. Normally, a large HyFE polarization induces a strong depolarization field which counteracts with the hyperferroelectric polarization. For HyFE to persist in LiZnSb, a large dielectric ϵ_∞ constant, which reduces the depolarization energy, is critical for stabilizing the hyperferroelectricity. We demonstrate that, reducing the high-frequency dielectric constant ϵ_∞ in LiZnSb has a significant impact on the hyperferroelectric instability. Specifically, we show that decreasing ϵ_∞ to 1/3 of its original value results in a tenfold reduction in the depth of the free-energy well, from ΔF=-332 meV to ΔF=-33.4 meV, which strongly suppresses the HyFE instability; furthermore, when ϵ_∞ is reduced to 1/4 of its original value, HyFE completely disappears.

(iv) Our further reveal that in-plane strain can be used to tune both the HyFE polarization and the free-energy well depth, enabling us to adjust the HyFE well depth and polarization to suit practical applications. We also discover that the HyFE polarization responds differently to in-plane strain compared to the ferroelectric polarization. While the FE polarization in LiZnSb under SCBC increases continuously with increasing compressive strain, the HyFE polarization under OCBC exhibits a non-monotonic strain dependence that is both interesting and distinct.

Overall, our investigations into the extended planar oxygen vacancies in $BaTiO_3$, and the hyperferroelectric properties of $LiNbO_3$ and LiZnSb have revealed exciting new phenomena and provided important insights into the mechanisms behind ferroelectricity under different conditions. We hope our findings pave the way for the development of novel materials with tailored ferroelectric properties for a wide range of technological applications. We also hope our research inspires further exploration and advances in this exciting field.